

Ludwig-Maximilians-Universität München

Faculty of Physics

Optimization and Design Constraints for Two-Dimensional Hyperuniform Photonic Band Gap Materials in the Search for a Universal Gap Sensitivity

Master's Thesis

Author: Argyrios Gkionis

Supervisors: Dr.-habil. Christoph Räth, Dr. Michael A. Klatt

Date: 20. October 2026



Ludwig-Maximilians-Universität München

Fakultät für Physik

Optimierung und Designeinschränkungen für zweidimensionale hyperuniforme photonische Bandlückenmaterialien auf der Suche nach einer universellen Lückensensitivität

Masterarbeit

Autor: Argyrios Gkionis

Betreuer: Dr.-habil. Christoph Räth, Dr. Michael A. Klatt

Datum: 20. Oktober 2026

Acknowledgements

I would like to express my sincere gratitude to my supervisors, Dr.-habil. Christoph Räth and Dr. Michael A. Klatt, for their support throughout this work. Also, I acknowledge the IT Support Team of the Faculty of Physics at LMU for maintaining and supporting the HPC, storage, and computational infrastructure used in this work.

Special thanks to Michael A. Klatt for his guidance through my thesis. He taught me patience, courage and how to think like a "modern" theoretical physicist, with an absolute balance between mathematics and computation. He "picked me up from the hand" and taught me computational skills, he gave me the opportunity to participate in conferences and workshops, he persuaded me to travel, enjoy and learn physics via extensive conversations with many researchers and people from the DLR institute. Michael, you were always listening to my problems, you gave me hope and I learned a lot for physics and life through your stories and extensive explanations and zoom meetings. A true mentor. A guiding figure. The best teacher I could have, thank you!

I also thank my colleagues: Luca Lotz and Joel Steinegger who despite their full schedule of academia and Phd responsibilities, they were always finding time for fruitful, email and in person, conversations. Moreover, I would like to express my gratitude toward the people who helped me with my first steps in Munich: Cornelius, Kostas, Alekos, Efi, Eirini and my beloved friends from Munich: Panagiotis, Alex, Alice, Anna, Spandan, Mahnoor, Pranav, Art, Eric, Karen, Keno, Nick, Nickos, Paola, Misael, Ragad, John and Angelos. Moreover I would like to thank my friends from Athens, who were listening my nonstop talking physics sessions: Stelios and Chris, and my "Bachelor friends": Chris, Alexis, Dionysis, Nikos, Tasos, Michalis and Nadia.

Last but not least, I would like to thank my family: Mum, Dad, Eleni and my grandma (Alexandra) for their encouragement and financial contribution, during the preparation of this thesis. Without their support I could not fulfill my dreams. As Nikos Kazantzakis, the famous Greek writer, stated: "Our life is just a flash of lightning, yet we still have time". And I will add the following: In this "lightning" which is called life, I prefer to spend my time with my family, my friends and good colleagues. And in this case I have all of them.

Declaration

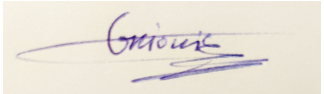
I hereby declare that this thesis is my own work, and that I have not used any sources and aids other than those stated in the thesis. During the preparation of this thesis, ChatGPT (OpenAI) was used as an auxiliary tool for language editing, including the correction of grammar, spelling, and phrasing, as well as for improving the clarity and readability of the text. ChatGPT was also used for technical assistance with computer programming and code development, including debugging and discussing possible implementations.

The scientific content, algorithms, analysis, interpretation of results, and conclusions presented in this thesis are the responsibility of the author. All AI-assisted suggestions were critically reviewed and independently verified by the author.

Declaration on Figures and Illustrations

All figures, plots, and illustrations presented in this thesis have been produced by the author, unless otherwise explicitly stated. Any material reproduced or adapted from books, scientific articles, or other sources is appropriately acknowledged and referenced. Where required, permission for reproduction has been obtained from the respective copyright holders.

München, 20.10.2026



Argyrios Gkionis

Abstract

Photonic crystals (PhCs) are natural or synthetic dielectric structures that exhibit periodic variations of the refractive index on the scale of the wavelength of light. Analogous to the electronic band structure in crystalline solids, photonic crystals can possess "energy" bands. Moreover, they can contain frequency regions where electromagnetic wave propagation is prohibited; these are the photonic band gaps (PBGs). In this manuscript, an introduction to the fundamental concepts of photonic crystals is presented.

Although the initial description is focused on crystals, which emerged from the foundational work of Sajeev John and Eli Yablonovitch, photonic band gaps can also be obtained from disordered dielectric materials. The presence of photonic band gaps for both crystal lattices and disordered structures is here examined. Disordered band gap materials lack long-range order, which might call the appearance of photonic band gaps into question. For this enigmatic connection between crystals, disordered materials and photonic band gaps, hyperuniformity is used as a deus ex machina. More specifically, stealthy hyperuniformity offers a kind of "hidden order" for disordered structures, which appears to be necessary to open a PBG while preserving isotropy. In addition, the appearance of PBGs on both types of structures triggers a scientific remark, around which this thesis is focused: is there a common, universal behavior of the "gap" for crystal and disordered structures?

The missing link is universal gap sensitivity, $S(\alpha)$, which describes the relation between the optimal gap-to-midgap ratio and dielectric contrast. A universality concept has been observed for three-dimensional (3D) systems by examining different kinds of photonic networks, for which the gap sensitivity tends for high dielectric contrast to the same result as for the one-dimensional (1D) quarter-wave stack (QWS). However, the two-dimensional (2D) case remains an open question. The purpose of this manuscript is to examine whether gap sensitivity appears to have the same universal behavior for 2D, optimized systems, specifically accounting for the complexity of transverse electric (TE) and transverse magnetic (TM) polarizations, that favor competing geometric features. We, therefore, study both complete PBGs for lattices composed of 2D networks and for TM band gaps in 2D structures composed of dielectric discs. Specifically, we present the universal behavior of gap sensitivity for TM gaps for disc packings in that we find that the numerical data approaches the universal curve for the QWS, but a small deviation persists up to the largest dielectric contrasts studied. Moreover, for network structures, we identify the challenges and limitations of the optimization procedure for 2D networks and provide a resource-efficient optimization technique, with an outlook to future research with larger computational resources. Moreover, we address the challenge of designing 2D hyperuniform systems by a rigorous theoretical analysis of the "slicing hypothesis", i.e., we raise the question whether hyperuniformity can be inherited by 2D slices from a 3D material. We answer the question in the negative by a "no-go theorem". Together, these results contribute to refining the design principles for next-generation isotropic photonic materials.

Contents

1 Introduction **10**
- 1.1 An overview of PhCs . . . 13
- 1.2 The master equation and the frequency modes . . . 15
  - 1.2.1 Revisiting Maxwells equations . . . 15
  - 1.2.2 Symmetries . . . 17
  - 1.2.3 Computational photonics . . . 20
- 1.3 Complete band gaps and gap sensitivity . . . 22
- 1.4 Our goal . . . 25

2 Photonic band gaps in discs and networks, heatmaps & more **27**
- 2.1 Disc packings . . . 27
  - 2.1.1 Why we do not observe complete PBGs in disc packings? 28
  - 2.1.2 Computing TM gap-to-midgap ratios . . . 28
- 2.2 Photonic networks . . . 33
- 2.3 Computing TE and TM gap-to-midgap ratios . . . 34
- 2.4 Complete PBGs . . . 38
  - 2.4.1 Complete PBGs in networks: methodology . . . 38
  - 2.4.2 Heatmaps for complete PBGs . . . 38

3 Optimization **41**
- 3.1 Optimizing 2D disc packings . . . 41
- 3.2 Optimizing 2D photonic networks . . . 48
- 3.3 Remarks on optimization processes . . . 53

4 No-go theorem for hyperuniform slices **54**
- 4.1 What is a random field? . . . 54
- 4.2 What is hyperuniformity? . . . 57
  - 4.2.1 Hyperuniformity in random fields . . . 57
  - 4.2.2 Hyperuniformity in two phase media . . . 59
- 4.3 Stereology for hyperuniform random fields . . . 62
  - 4.3.1 Stereological expansion to random fields . . . 62

5 Conclusions and outlook **67**

A Appendix: Heatmaps for TE/TM polarization **72**

B Appendix: Heatmaps for complete PBGs **83**

1 Introduction

> "Where there is matter, there is geometry."
>
> Johannes Kepler

A wealth of physical examples, like rugged energy landscapes, percolation, self-assembly structures and systems with quenched disorder, provide a "playground" where statistical physics and geometry are interwoven [1]. Many particles, atoms, hard spheres, veins and dielectric networks interact and self-organize in spatial structures which are characterized by symmetry, topology and connectivity. These three parameters, related to geometry, can determine the physical properties of the materials. A major example is the appearance of **photonic band gaps** (PBGs) of photonic crystals (PhCs). The complex phenomenon of PBGs is determined primarily by the geometry of the dielectric medium, and this dependence is highly non-trivial and non-linear. For instance, by adjusting the thickness of two-dimensional PhC slabs, we affect the electromagnetic (EM) modes that propagate through them, and so we can "control" the gap values [2]. Moreover, PhCs made with defects or constructed by specific compounds can allow more complex behavior; localization phenomena [3], nonlinear effects (Kerr nonlinearity) [4], etc. So, manipulating the geometry of structures can provide rich physics phenomena for PhCs. Modifying microscopic parameters that define crystal lattices can suppress or amplify the opening of PBGs, paving the way for new technological applications (e.g., waveguides, lasers, optical computing).

We can construct PhCs from crystals with ordinary lattice geometry, e.g. with simple cubic, triangular, or hexagonal symmetries. In two dimensions, "simple cubic" refers to the square lattice, and "hexagonal" to the honeycomb structure. These structures can be composed by dielectric discs (embedded in air or vacuum) or by combinations of discs and rods that create complex dielectric networks, which we characterize by their connectivity and symmetry. While crystals provide many PBGs and allow for the study of transversal electric (TE) and transversal magnetic (TM) modes, they lack isotropy, a concept important for the manipulation of light propagation in any possible direction. The key to create materials that block light in the same way in all directions (isotropic PBGs) requires a different kind of order: stealthy hyperuniformity [5, 6, 7]. Systems of particles that interact via isotropic "stealthy" bounded long-ranged pair potentials are remarked to have classical ground states that are hyperuniform and that can be disordered and highly degenerate. Disordered hyperuniform systems are exotic states of matter that behave isotropic like a liquid and homogeneous as a crystal. Their novel physical properties are connected with the appearance of large photonic band gaps [6]. In other words, a disordered structure apparently needs to be stealthy hyperuniform for opening a PBG [7]. "Stealthy" implies that the hyperuniform patterns are transparent, i.e. $S(k) = 0$, for a range of certain wavenumbers $0 < k < K$. In other

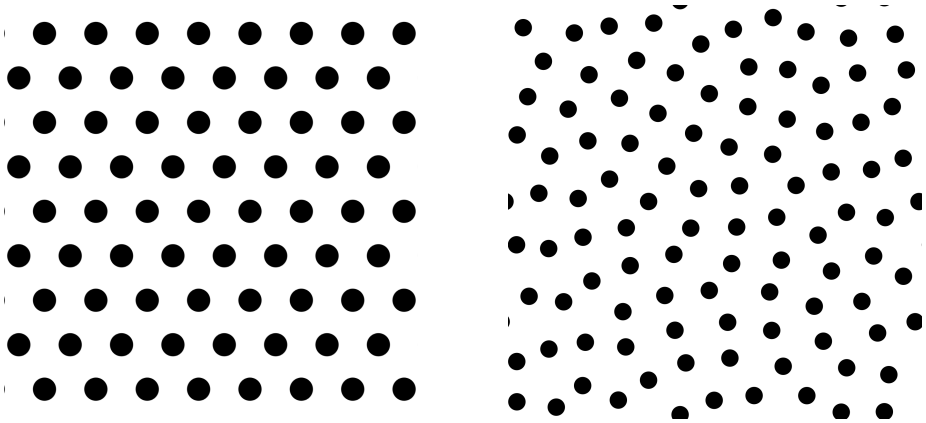


Figure 1: Two stealthy hyperuniform 2D point patterns, a crystal (left) and a disordered sample (right), both are produced by converting an h5 file into a png file. Each file is produced by MPB for disc packings arranged according to the original point pattern.

words, the structure factor of stealthy point patterns is continuous and equal to zero for a finite range of wavenumbers. For sufficiently small values of K, the stealthy patterns can be disordered and isotropic, but (perfect) crystals are also stealthy hyperuniform. Two stealthy point patterns are presented in Figure 1 for a crystal and a disordered sample, respectively.

PBGs can occur in heterostructures composed of two, three, or more materials with different dielectric constants (e.g., Si and air, GaAs, glass rods in air, polymers). In disc structures (dielectric discs embedded in air), only gaps from TM modes are obtained; TE gaps are absent or negligible. Moreover, complete photonic band gaps (CPBGs) that prohibit the propagation of light in all in-plane directions and for both polarizations occur on dielectric network structures, where both TE and TM mode gaps are allowed. Taking into account these structures and the notion of PBGs, we immediately come up with the following questions: can we construct optimal lattices for photonic crystals, where maximum gap values occur? Is there any underlying universal behavior between different heterostructures that will allow to understand deeply the formation of PBGs and provide new tools for designing novel materials? Recent discoveries [8] have noted the existence of a hidden, universal behavior in how the band gap responds to dielectric contrast (the ratio of the dielectric constants between two compounds); this refers to **universal gap sensitivity**. Gap sensitivity is the first derivative of the optimal gap-to-midgap ratio, $S(\alpha)$ and $\Delta(\alpha)$ respectively. Research conducted on 3D lattices states that $S(\alpha)$ appears to take a universal form that is well approximated by the analytical formula of a 1D quarter-wave stack, for large values of dielectric contrast and a variety of heterostructures and crystals. Although research has been conducted for 1D and 3D structures, there is a missing link in our understanding of the universal gap sensitivity concept for 2D materials. This thesis aims to explore this notion in 2D structures and discuss the difficulties in achieving a CPBG in two-dimensions, because

of the competition between TE and TM polarizations, both of which must be suppressed to achieve a complete gap. Because of the high computational cost of determining PBGs, we devise an efficient optimization procedure that balances accuracy and computational resources. We thus find gap sensitivities for the TM PBGs of our disc packings that almost converge to the universal curve found in one and three dimensions. However, we observe a small offset that does not vanish for our largest dielectric contrasts of about 20. Not all systems are available for our analysis of complete PBGs, either because of numerical limitations (like computational cost excluding the disordered networks) or because of the lack of a sizable complete PBG (like in our triangular network). For our two available networks (simple cubic and hexagonal) with complete PBGs, we observe an even stronger difference. For the hexagonal network, the gap sensitivity shows a qualitatively similar behavior, but it the curve is substantially above that for the universal curve of the QWS. The three reliable data points for the simple cubic network lie below that of the QWS; they approach the QWS curve, but there is too few data to decide or reject an agreement for larger dielectric contrasts. Whether this offset is due to numerical limitations or a real physical effect arising from the competing geometries for TE and TM PBGs remains an interesting question for further research.

Moreover, we "dig" deep into the construction principles of 2D hyperuniform systems and with the help of stereology and statistical mechanics, we expand the theoretical framework of the **"slicing hypothesis"**, which discusses the following intuitive idea: If we had a 3D hyperuniform material, can we simply take a 2D slice of it to obtain a 2D hyperuniform material? This manuscript presents the work around this hypothesis by employing knowledge from random fields and stereology. We propose and prove a **"no-go theorem"** which mathematically rules out the "slicing" method of materials, proving that hyperuniformity is not inherited under dimensional reduction for isotropic fields.

The structure of the thesis is as follows: Firstly, we briefly introduce the basic notions of photonic band theory, gap-to-midgap ratio, gap sensitivity, and how to solve Maxwell equations as an eigenvalue problem. Next, we discuss the appearance of PBGs on photonic heterostructures and explain the numerical procedures used (MPB software, data analysis of the eigenfrequencies via Python codes, and the development of optimization algorithms). Special emphasis is placed on photonic band gaps in systems composed of discs and network structures, as well as on the emergence of complete photonic band gaps. In addition, we summarize our numerical results for two-dimensional lattices composed exclusively of dielectric discs, for which we identify a universal gap-sensitivity law across four different lattice geometries. The results exhibit a small deviation from the asymptotic behavior predicted by the theoretical curve for the quarter-wave stack crystal; we discuss possible reasons, both numerical and physical. We then analyze our findings for complete photonic band gaps (CPBGs) in network structures, discussing the challenges in validating the gap sensitivity law due to limited numerical resolution, as well as the influence of TE and TM polarizations on the optimal lattice geometry, in a way that both the numerical and physical explanations for the deviations become more rele-

vant. Furthermore, we introduce the mathematical framework of random fields and hyperuniformity and investigate the slicing hypothesis using stereological assumptions, culminating in the proof of a no-go theorem. Finally, we synthesize our numerical and theoretical findings and discuss their implications for the design of photonic band-gap materials.

1.1 An overview of PhCs

The understanding of electronic properties of materials has led to a breakthrough in our technology. Semiconductors, alloys and many ceramics are crystal structures; periodic arrangement of atoms or molecules.

Electrons in crystals are arranged in **energy bands**. Bands can be separated by energy regions where no wave-like electron orbitals exist. Such prohibited regions are called **band gaps** or **energy gaps**, an outcome from the interaction of electron waves with the ion cores (potentials) of the crystal ([9], Chapter 7: Band Structure). From the above, a new kind of question emerges: can we take advantage of the periodicity of a crystal and create new materials that will manipulate light (electromagnetic waves) instead of electrons?

The answer is yes! The optical analogue of a semiconductor is the photonic crystal (PhC). Unlike lattices of atoms, which can be found in nature in many crystalline compounds, most photonic crystals have to be designed in the lab with a vast constraint: "human imagination". The atoms or molecules are replaced by macroscopic media with differing dielectric constants and periodic dielectric functions earn the place of the periodic potential that is used in crystals. This implies that the nomenclature of solid state physics: Brillouin zone, reciprocal lattice, band gaps, Van Hove singularities, and defects, is inherited by photonic crystals. PhC's are low-loss periodic mediums, designed with high dielectric contrast α, which is associated with a strong contrast of the refractive index n. In particular, we can design PhC's with **photonic band gaps**, frequency regions (spectrum) in which light propagation is prohibited in certain directions. Taking this analysis further, we can construct mirrors, waveguides and materials, which manipulate light not only in the microwave spectrum, but even further; like optical frequencies and infrared.

Figure 2, represents an analogue between an electronic band gap (on the left) and a photonic band gap (on the right). The energy bands (band structure) theory, described first for the movement of electrons in a landscape of ionic potentials, on a crystal, was proved to be applicable also in the case of Photonic crystals [10]. More specifically, in the last case, photons do not interact with each other, in contrast with electrons, making the theory more profound. In addition to the application of band structure theory, the independent discoveries of Sajeev John, for an optical analogue of Anderson localization in carefully constructed, disordered photonic superlattices [3] and Eli Yablonovich, for the inhibition of spontaneous emission of light, in solid state structures [11], have paved the way for the development of the field of photonic crystals and photonic band-gap materials. The above research has shed light first to the three dimensional photonic structures. Later research focused on one- and two-dimensional

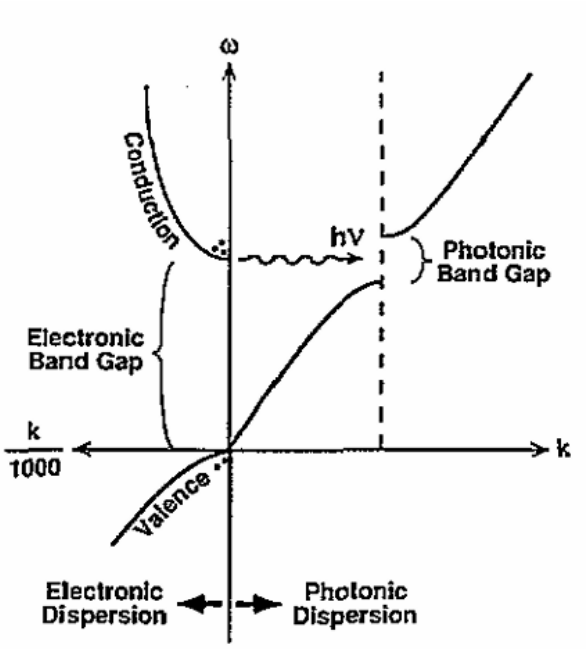


Figure 2: On the left, there is an electron wave dispersion, of a direct gap semiconductor and on the right there is a forbidden gap for photonic crystals, with an electromagnetic wave dispersion relation. The "dots" on the left represent electrons and holes, positioned on the highest band before the gap (valence band) and the lowest band above the gap, called conduction band, respectively. Each band is characterized by a number, n (=1,2,3,...). In photonic crystals, the band above the gap is called **air band** and the band below the gap is called **dielectric band**. Each band is characterized by a dielectric constant, ε. For an air band, $\varepsilon = 1$. The ratio of the dielectric constants of dielectric and air band gives the dielectric contrast, α which we will use later in our study of gap-sensitivity. (Reproduced with permission from Yablonovitch 1993 [10], https://doi.org/10.1088/0953-8984/5/16/004. © IOP Publishing Ltd)

photonic structures, demonstrating that these systems could exhibit complete photonic band gaps for in-plane propagation, leading the way to new technological applications. Lastly, it should be mentioned that, despite the challenges involved in designing photonic heterostructures, nature has already achieved remarkably sophisticated optical architectures through evolutionary processes. Biological systems provide striking examples of naturally occurring photonic structures that manipulate light in ways comparable to engineered photonic crystals.

One notable example is butterfly wings, whose vivid coloration often does not originate from pigments but from periodic micro- and nanostructures acting as natural photonic crystals. These structures selectively reflect specific wavelengths of light through photonic band-gap effects and structural interference, giving rise to their characteristic iridescent colors. Such naturally evolved photonic architectures have become an inspiration for the design of artificial

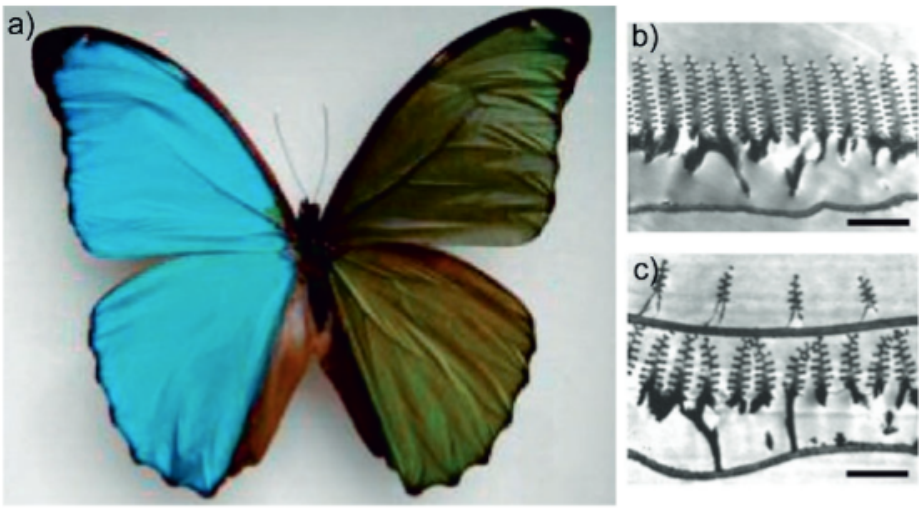


Figure 3: (a) Photograph of wings from the butterfly Morpho rhetenor. In picture (b) we can observe TEM (transmission electron microscopy) images of cross-section of its wing scales. In (c) we have one more TEM image from another butterfly species. The scale bars are $1.8\,\mu m$ and $1.3\,\mu m$, respectively. nature uses photonic crystal structures to a wide extent. The characteristic color of beetles and butterflies, is due to the amorphous structure that their wings are made from, allowing them to use it as a survival and adaptation technique to environments. (Reproduced with permission from Fenzl et al. 2014 [12]. © 2014 Wiley-VCH GmbH.)

photonic materials.

1.2 The master equation and the frequency modes

In this subsection, we use Maxwell equations in dielectric media and the eigenvalue problem approach from mathematical physics, to develop a master equation describing the electromagnetic (EM) waves propagation in Photonic crystals environments. The solution of the eigenvalue problem, provide the eigenvalues (frequencies, ω) and the EM modes for the electric and the magnetic field, E and H respectively.

1.2.1 Revisiting Maxwells equations

The propagation of light in a Photonic crystal is governed by the well known, four, macroscopic Maxwell equations (in a medium), in SI units:

$$\begin{aligned} \nabla \cdot \mathbf{D} &= \rho & \nabla \times \mathbf{H} - \frac{\partial \mathbf{D}}{\partial t} &= \mathbf{J} \\ \nabla \times \mathbf{E} + \frac{\partial \mathbf{B}}{\partial t} &= 0 & \nabla \cdot \mathbf{B} &= 0 \end{aligned} \tag{1}$$

where **E** and **H**, are the Electric and magnetic field respectively (as mentioned above), **D** and **B** are the electric displacement and magnetic induction fields, and ρ and **J** are the free charge and current densities (the vector quantities are written with a bold black color, for distinction from scalar quantities). The propagation of EM waves, for our case, is restricted in a mixed dielectric medium (or multiphase medium), composed from different components each characterized by a specific dielectric constant, $\varepsilon(\mathbf{r})$. The material is composed of homogeneous regions, there are no time variations in the structure, and we assume there are no free charges or density currents ($\rho = 0$ and $\mathbf{J} = 0$). This heterostructure is periodic. In addition, we assume, for our calculations, that the material is macroscopic and isotropic (off-diagonal terms in the dielectric permittivity tensor vanish and diagonal terms are equal), so that the electric field and the displacement, **E** and **D** respectively, can be related by the vacuum permittivity, ε_0, multiplied by a scalar dielectric function $\varepsilon(\mathbf{r}, \omega)$, also known as relative permittivity. Moreover, we ignore any material dispersion of the dielectric constant ($\varepsilon(\mathbf{r})$). Lastly, we take into account only positive and real values of $\varepsilon(\mathbf{r})$ (transparent materials). Taking into account the above approximations, we have $\mathbf{D} = \varepsilon_0 \varepsilon(\mathbf{r})\mathbf{E}(\mathbf{r})$ [13]. For the magnetic induction, we have a similar equation: $\mathbf{B} = \mu_0 \mathbf{H}(\mathbf{r})$, by setting the relative magnetic permeability equal to one (true for most dielectric materials). With $\mu_o = 4\pi \times 10^{-7} Henry/m$, we define the vacuum permeability. With all the assumptions, the Maxwell equations become:

$$\begin{aligned} \nabla \cdot [\varepsilon(\mathbf{r}) E(\mathbf{r}, t)] &= 0 & \nabla \times \mathbf{H} - \varepsilon_0 \varepsilon(\mathbf{r}) \frac{\partial \mathbf{E}(\mathbf{r}, t)}{\partial t} &= 0 \\ \nabla \times \mathbf{E} + \mu_0 \frac{\partial \mathbf{H}(\mathbf{r}, t)}{\partial t} &= 0 & \nabla \cdot \mathbf{H}(\mathbf{r}, t) &= 0. \end{aligned} \tag{2}$$

Our next step is to use the linearity of Maxwells equations, to separate the time from the spatial dependence of both fields, **E** and **H**, by expanding them into a set of **harmonic modes**. By Fourier analysis, we know that we can develop any solution as a linear superposition of the harmonic modes. Fourier and mathematical convenience, allows us to write the modes in the following form:

$$\mathbf{H}(\mathbf{r}, \mathbf{t}) = \mathbf{H}(\mathbf{r}) e^{-i\omega t} \tag{3}$$

$$\mathbf{E}(\mathbf{r}, \mathbf{t}) = \mathbf{E}(\mathbf{r}) e^{-i\omega t}. \tag{4}$$

By applying Eq. (3) and Eq. (4) into Maxwell equations, we derive two curl- and two divergence equations. If we divide the curl-equations by $\varepsilon(\mathbf{r})$ and then apply again the curl ($\nabla\times$), we derive a **master equation**:

$$\nabla \times \left(\frac{1}{\varepsilon(\mathbf{r})} \nabla \times \mathbf{H}(\mathbf{r}) \right) = \left(\frac{\omega}{c} \right)^2 \mathbf{H}(\mathbf{r}), \tag{5}$$

where we have used the vacuum speed of light, $c = 1/\sqrt{\varepsilon_0 \mu_0}$. Moreover, the two divergence equations, tell us that there are no sinks or point sources of magnetic field and displacement in the medium:

$$\nabla \cdot \mathbf{H}(\mathbf{r}) = 0, \ \nabla \cdot [\varepsilon(\mathbf{r})\mathbf{E}(\mathbf{r})] = 0. \tag{6}$$

Equations (5) and (6), provide the information that we need to know about the magnetic field, $\mathbf{H}(\mathbf{r})$. Due to the transversality requirement, we can find a similar equation for the electric field, $\mathbf{E}(\mathbf{r})$. Here for mathematical simplicity we use the magnetic field for our master equation.

In addition, by identifying the left hand side of the master equation as an operator: $\hat{\Theta} := \nabla \times \left(\frac{1}{\varepsilon(\mathbf{r})} \nabla \times \right)$, we can redefine the master equation as an eigenvalue problem, exactly as in quantum mechanics. The operator is applied in the magnetic field, $\mathbf{H}(\mathbf{r})$, and we receive the function itself (eigenfunction) multiplied by a constant (eigenvalue):

$$\hat{\Theta}\mathbf{H}(\mathbf{r}) = \left(\frac{\omega}{c}\right)^2 \mathbf{H}(\mathbf{r}). \tag{7}$$

The eigenfunctions, $\mathbf{H}(\mathbf{r})$, are the spatial patterns of the harmonic modes (fields), and the eigenvalues are $\left(\frac{\omega}{c}\right)^2$, which are proportional to the frequencies of the modes, ω. The operator, described earlier, $\hat{\Theta}$, is Hermitian and positive semi-definite (explaining the non-negativity of the eigenfrequencies, ω^2). Thus ω is real.

1.2.2 Symmetries

We already know from classical and quantum mechanics, that by specifying the symmetries of a system, we can deduce general properties of the system's behavior. Imagine that we need to compute the modes of EM waves in an infinite glass plane. This system exhibits continuous translational symmetry in two dimensions (x, y), and the dielectric constant varies only in the z-direction, $\varepsilon(\mathbf{z})$. We can distinguish the modes by a set of two parameters, $(\mathbf{k}, n)$, where $\mathbf{k}$ represent the values of the wavevector and n is the **band number** (a particular mode's place in line of increasing frequency). As n increases, so does the frequency. The band number can be represented by integers, if the frequency spectrum is discrete, or by a continuous set of numbers. If we plot the wave vector versus the mode frequency, we get the **band structure** (band diagram or dispersion relation). From that a new question is raised: what kind of symmetry describes the photonic crystals?

We know that photonic crystals are periodic structures, and their periodicity can expand in one-, two-, or three-dimensions. So, due to their restrictive geometries, they do not exhibit continuous translational symmetry. Although, they have discrete translational symmetry, not invariant under translations of any distance. Only distances that are multiple of a fixed length (e.g. lattice constant, a_ℓ). For our analysis, we will focus on the mathematical formalism

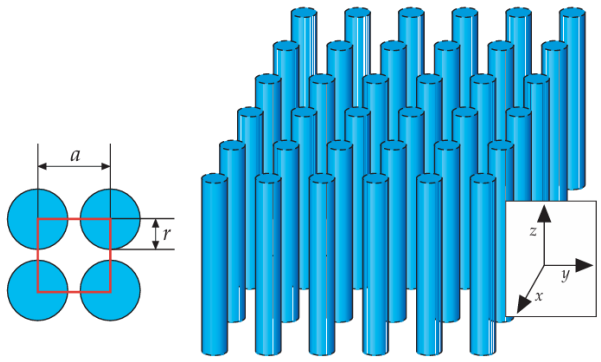


Figure 4: A two dimensional Photonic crystal. Picture is borrowed from the book: Photonic crystals: Molding the flow of light: Joannopoulos et. all [2]. This PhC has a square lattice geometry, this material is homogeneous along the z-direction and we can imagine the cylinders (rods) to be very tall. The periodicity extends to the xy plane and the lattice constant is a_ℓ. The "small" image of the lattice, on the left, indicates the unit cell with a red color, as we can see the photonic crystal from above. (Reproduced with permission from Joannopoulos et al. 2008, *Photonic Crystals: Molding the Flow of Light* [2]. © Princeton University Press.)

in the case of two-dimensional structures. An example of a two-dimensional photonic crystal, with a simple-cubic symmetry is given in Figure 4 .

A two-dimensional photonic crystal is periodic along two of its axes (x, y) and homogeneous along its third axis (z). The system is homogeneous in the z-direction, so the modes should be oscillatory in that direction, with no restrictions on the wave vector, k_z. In addition, the system has discrete translational symmetry in the xy plane, with $\varepsilon(\mathbf{r}) = \varepsilon(\mathbf{r} + \mathbf{R})$, where $\mathbf{R}$ is a linear integer combination of the primitive lattice vectors, $a_\ell \hat{\mathbf{x}}$ and $a_\ell \hat{\mathbf{y}}$ respectively. The discrete periodicity of the crystal, allow us to use the Bloch's theorem for the modes, that their $k_{||}$ values (wave vector values on the xy plane) lie on the Brillouin zone. Specifying the modes of the crystal by $k_{||}$, k_z and n (the band number), we derive the following form for the Bloch states:

$$\mathbf{H}(n, k_z, k_{||})(\mathbf{r}) = e^{ik_{||}\boldsymbol{\rho}} e^{ik_z z} \mathbf{u}(n, k_z, k_{||})(\boldsymbol{\rho}), \tag{8}$$

where $\boldsymbol{\rho}$ is the projection of the coordinate vector, $\mathbf{r}$, in the xy plane and $\mathbf{u}(\boldsymbol{\rho})$ is a periodic function, $\mathbf{u}(\boldsymbol{\rho}) = \mathbf{u}(\boldsymbol{\rho} + \boldsymbol{R})$, for all lattice vectors, $\mathbf{R}$.

If we plug the Bloch state (Eq. (8)) into the eigenvalue problem (Eq. (7)), we derive a new Hermitian operator that depends on the Bloch wave vector, $\mathbf{k}$:

$$\hat{\boldsymbol{\Theta}}_{\mathbf{k}} := (i\mathbf{k} + \nabla) \times \frac{1}{\varepsilon(\mathbf{r})} (i\mathbf{k} + \nabla)\times, \tag{9}$$

and a new eigenvalue problem of the form:

$$\hat{\boldsymbol{\Theta}}_{\mathbf{k}} \mathbf{u}_{\mathbf{k}}(\mathbf{r}) = (\omega(\mathbf{k})/c)^2 \mathbf{u}_{\mathbf{k}}(\mathbf{r}). \tag{10}$$

The modes are subject to transversality and the periodic profile of the function $\mathbf{u}$. Because of the periodic boundary condition we restrict the eigenvalue

problem on a single unit cell of the photonic crystal. This restriction gives a discrete spectrum, as exactly is happening when someone is solving the Schrodinger equation for a particle in a box [14].

Although the spectrum is discrete, Joannopoulos et al. [2], mention that the wave vector, $k_{||}$ which lies inside the Brillouin zone, enters as a continuous parameter in the $\hat{\Theta}$ operator. So every time you change $\mathbf{k}$, you solve a different eigenvalue problem, e.g. for one value $\mathbf{k_1}$ you derive many ω values: $\omega_1, \omega_2, \omega_3, ...$. For a nearby wave vector, $\mathbf{k_2}$, you derive again a set of frequencies: $\omega_1', \omega_2', \omega_3', ...$. So we expect the frequency of each band, for a given number, n, to vary continuously as $\mathbf{k}$ varies. Thus, the frequency modes, of a photonic crystal is a family of continuous functions $\omega_n(\mathbf{k})$, indexed in order of increasing frequency, by the band number, n. A mathematical equivalence is coming from classical mechanics and the frequencies of a guitar. The modes are discrete but if we apply a smooth tension, T, the index n is still discrete but the function, $f_n(T)$, becomes continuous. All the important information contained in this functions, is accumulated in the band structure of the photonic crystal.

Taking into account what has been mentioned above, a new question is raised: for a given photonic crystal, with dielectric constant, $\varepsilon(\mathbf{r})$, how can we calculate these band structure functions, $\omega_n(\mathbf{k})$?

The answer of this task is that we, actually have to apply computational effort in order to solve the standard eigenvalue equation (master equation). A common way is via the iterative minimization technique. More information about the available numerical methods and the computational tools that are used, is given in the following section: Numerics.

In this paragraph, we will emphasize that for the computation of the frequency bands, of a photonic crystal with a simple cubic symmetry (and for any other crystal structure), we choose to work on the **irreducible Brillouin zone**. Because $\omega_n(\mathbf{k})$ inherits the symmetry of the lattice, we do not want to solve the problem in an "extended" region at every $\mathbf{k}$-point. We can derive enough information of the system by solving the eigenvalue problem on the one-eighth of the first Brillouin zone. The reader can grasp an idea of the irreducible Brillouin zone, with Figure 5.

All the formalism of the Bloch states and the ideas developed above, can be expanded for three-dimensional photonic crystals, like the Yablonite, or be reduced in one-dimension, in order to describe the quarter-wave stack, a multilayer film, with each layer having a quarter wavelength width and an optimal volume fraction (for more information, take a look at [2]).

In the last paragraph, we will present another important symmetry, the **mirror symmetry** (reflection symmetry), with respect to the plane of periodicity. It is one of the point symmetries, encountered in the two-dimensional materials, slabs etc. For a reflection about the xy plane we get $(x, y, z) \rightarrow (x, y, -z)$. This transformation is called a mirror reflection.

For the case of photonic crystals, suppose now that you have a dielectric function that satisfies:

$$\varepsilon(x, y, z) = \varepsilon(x, y, -z).$$

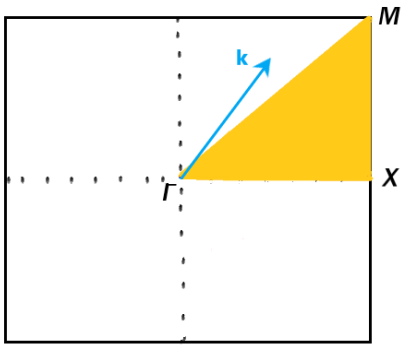


Figure 5: The Brillouin zone, of the squared lattice, centered at the origin (Γ). An arbitrary wave vector $\mathbf{k}$ is indicated in the picture with blue color. The irreducible Brillouin zone, is the yellow triangular wedge. The spatial points at the center, corner and face are known as Γ, M and X respectively. (Adapted from Joannopoulos et al. 2008, *Photonic Crystals: Molding the Flow of Light* [2]. © Princeton University Press.)

This mean that the structure is invariant under the mid-plane. Then the Maxwell operator commutes with the mirror operator, $[\hat{\Theta}, \hat{M}_z] = 0$. Therefore the modes can be chosen to have definite mirror parity: even (symmetric) or odd (antisymmetric). For an ideal photonic crystal with infinite rods and invariant along z, Maxwell equations separate into two independent scalar problems. These modes (with $k_z = 0$) propagate parallel to the xy plane. Then the even and odd symmetry, classify the modes by separating them into two distinct polarizations: the **TE**-polarization, where the magnetic field ($\mathbf{H}$) is normal to the plane and the electric field ($\mathbf{E}$) is confined to the xy plane ($\mathbf{E}(\boldsymbol{\rho}) \cdot \hat{z} = 0$). And the **TM**-polarization, where the electric field is normal to the xy plane and the magnetic field lies on the plane ($\mathbf{H}(\boldsymbol{\rho}) \cdot \hat{z} = 0$).

The band structure of TE and TM modes can be different. This means that we can observe a band gap for a TE mode and not for a TM mode and vice versa. According of course to the symmetry of the system that we have to deal with every time.

1.2.3 Computational photonics

This paragraph, can actually be associated with a very basic question: why we need numerics to solve Maxwell's equations for EM-wave propagation in a specific material?

This is actually one of the central questions behind computational physics. A short answer is that we use numerics, because Maxwell's equations become analytically unsolvable once the dielectric function has a complicated spatial dependence. So, the problem does not lie on the mathematical form of the equations, but on the different type of geometries for the photonic crystals that

we investigate. As we can observe from Eq. (5), the dielectric constant, $\varepsilon(\mathbf{r})$, is inside the differential operator, because it changes from point to point. If we had the privilege to talk about a homogeneous medium, then we could drop out the dielectric constant, and then we would obtain a Helmholtz equation, describing a homogeneous solution, $\nabla^2 u + \lambda u = 0$, where λ are the corresponding eigenvalues.

In this manuscript, the geometries that we will investigate are complex. We have lattices constructed from rods, cylinders or discs, that they are easier to investigate and network structures, that combine the geometric elements mentioned above to create a lattice of a dielectric network. Moreover we have hyperuniform structures and disordered materials, which increase the amount of complexity. Every interface in the photonic crystal, changes the boundary conditions. The field can be bended, reflected or be coupled everywhere. We can not find a magic way to reduce the complexity and solve the problem analytically. So, we need to follow a numerical approach to decrease this eigenvalue problem with infinite degrees of freedom into a finite dimensional one and solve it.

For the computation of the band structures, we will use MPB-software (MIT Photonic Bands, [15]). MPB is a free and open software package, developed for computing band structures, EM-modes and dispersion relations of periodic dielectric structures. It computes definite-frequency eigenstates, or harmonic modes, of Maxwell's equations for periodic dielectric structures of lossless, wavelength-independent, anisotropic ε and μ, for arbitrary wavevectors, using fully-vectorial and three-dimensional methods, making it highly applicable for the case of photonic crystals.

MIT team, has also developed, a time-domain analysis method (MEEP), but it will not be appropriate for our case. Our work is to find the band structures. This means that we have to solve the Maxwell eigenproblem for the frequencies of a periodic system, as given from the master equation (for this periodic dielectric structure, what electromagnetic modes are allowed, and at which frequencies?). MPB directly solves the eigenvalue problem on the finite unit cell of the structure. In addition to the eigenequation, the Bloch-envelope function, $\mathbf{u_k}(\mathbf{r})$, must fulfill the transversality equation: $(i\mathbf{k} + \nabla) \cdot \mathbf{u_k}(\mathbf{r}) = 0$.

For each Bloch wavevector k, MPB expands the electromagnetic fields in a finite plane-wave basis, transforming Maxwell's master equation into a matrix eigenvalue problem. Solving this problem yields the eigenfrequencies $\omega_n(\mathbf{k})$, and the corresponding Bloch modes, from which the photonic band structure is constructed.

More precisely, suppose that we move in path, inside the reduced Brillouin zone, $\Gamma \to X \to M \to \Gamma$, then MPB performs at k_1: computes $\omega_1, \omega_2, ..., \omega_m$. Then at k_2: computes $\omega_1, \omega_2, ..., \omega_m$, etc. Until it reaches the last k-point. Also, it computes the corresponding eigenmodes (the fields distribution).

For these computations, we use Scheme-based scripts developed for the MPB (MIT Photonic Bands) software. Simulations are performed for different geometries, including simple cubic (sc), triangular, and hexagonal lattices, for both photonic crystals consisting of dielectric discs embedded in air and network structures. The simulations provide the eigenfrequencies and electromagnetic

modes, from which Python scripts are used to generate the corresponding band structures and analyze their dependence on the system parameters, such as the cylinder radius and dielectric constant. Finally, the computed modes are used to identify and characterize the occurrence of photonic band gaps for the different geometries.

1.3 Complete band gaps and gap sensitivity

We have already mentioned in paragraph "An overview of photonic crystals" what is a photonic band gap and its importance. A photonic band gap corresponds to a frequency interval in the spectrum, in which electromagnetic waves can not propagate through certain directions in the photonic crystal.

In two-dimensional photonic crystals, that we will focus in this manuscript, band gaps are commonly polarization dependent, with separate gaps arising for transverse electric (TE) and transverse magnetic (TM) modes. Isolated patches of high-dielectric constant regions (high-ε) lead to TM-like polarization gaps (isolated dielectric discs or rods of a specific type of geometry, embedded in air). Whereas, connectivity of high-ε regions (dielectric veins), lead most likely into TE-polarization gaps. A two-dimensional (or a three-dimensional) crystal has different periodicity in different directions. The gaps in each direction tend not to overlap unless they are large enough, which requires a minimum dielectric contrast value ($\alpha = \frac{\varepsilon_{high}}{\varepsilon_{low}}$, where the numerator corresponds to a medium with a high dielectric constant, and the denominator, to a lower one. In our case, $\varepsilon_{low} = 1$). The more equal we can make the periodicity in each of the different directions, the more "circular" the Brillouin zone becomes, facilitating the overlap of gaps for different directions, so we tend to a complete band gap [9, 2]. This means that the more isotropic is a Brillouin zone, for a crystal, in the reciprocal space, the more probable is to have a complete band gap (suppression of light propagation in every direction).

A complete photonic band gap (CPBG) is obtained when the forbidden frequency interval overlaps for both polarizations, preventing electromagnetic propagation regardless of polarization or propagation direction in the plane.

Complete photonic band gaps, are essential because they enable full electromagnetic confinement and are important for applications such as waveguides, optical cavities, low-loss photonic integrated circuits, nanoscopic lasers and more [16].

Next we will analyze how do we measure a band gap. The size of a band gap (it's extension) can be characterized by its frequency width, $\Delta\omega$. However, Maxwell equations are scale-free. So we can find a more appropriate measure, which is independent of the scale, to describe the gap. This measure is called **gap-to-midgap ratio** and is defined as the ratio of the frequency width over the frequency at the middle of the gap. The mathematical form is given below and is expressed as a percentage (e.g. 20 percent gap refers to a gap-to-midgap ratio of 0.2): gap-to-midgap ratio $:= \Delta\omega/\omega_m$.

Thus, when we mention the size of the gap, we refer to the gap-to-midgap ratio, which does not variate even if the scale of the system changes. Moreover,

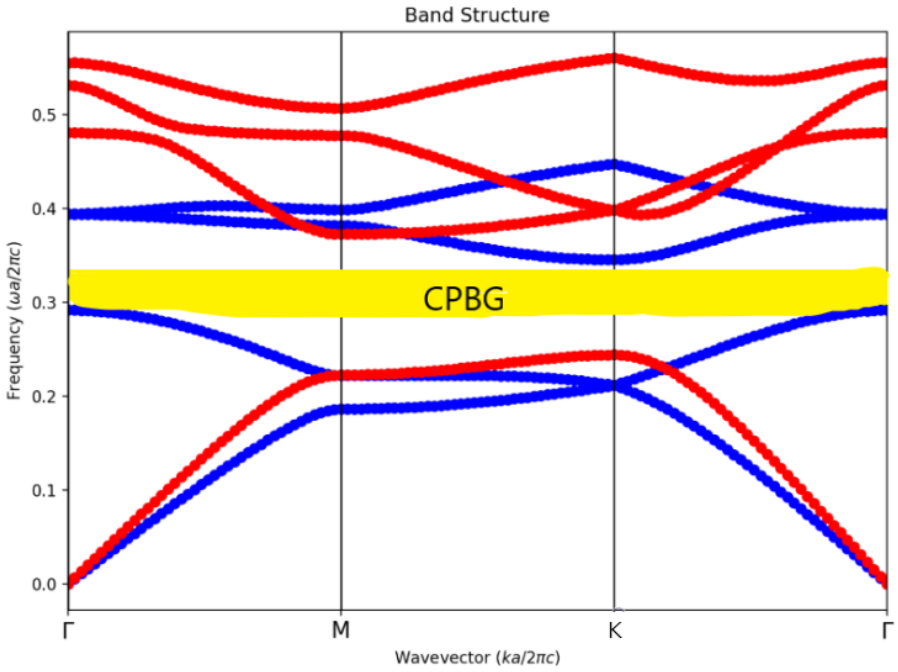


Figure 6: A band structure of a photonic crystal with a hexagonal lattice geometry. The microscopic parameters that describe this network structure (which will be analyzed in section 2), are given by: $r_{disc} = 0.2$, $r_{rod} = 0.05$ and dielectric contrast, $\alpha = 13.0$. The red color represents TE-polarization bands, whereas the blue color bands represent the TM-polarization solutions. For the observation of complete band gaps, we have constructed a python script that compares the TE and TM values and finds frequency regions that overlap for both polarizations. In the figure we represent with yellow color the region where a possible complete band gap may occur. An observation of the band structure can tell that in this region there are k-values for which the gaps of TE- and TM-polarization overlap.

all the graphs and band structures, that involve the frequency and the wavevector, will be written as dimensionless parameters ($\omega a_\ell/2\pi c$ and $ka_\ell/2\pi$, where a_ℓ is the lattice constant).

In this work, TE and TM bands are computed independently via the use of MPB-software. So, we identify a complete band gap if we compare the frequency intervals of both polarizations and determine whether a common forbidden interval exists.

At this moment, we will introduce the second concept of this paragraph; gap sensitivity. While maximizing the photonic band gap is an important objective in the design of photonic crystals, the maximum value alone does not provide a complete description of the system. In practical applications, material properties and geometrical parameters are often subject to fabrication tolerances, making it important to assess how the band gap changes under variations of these parameters. Moreover, there are materials characterized by a disorder network structure, which typically consists many localized defects, causing the

break up of large PBG into smaller ones [3]. This motivates the introduction of the **gap sensitivity**, which quantifies the dependence of the band-gap width on a selected design parameter (e.g. r_{rod}, r_{disc}, etc.); for more details, see [8].

Michael A. Klatt, Paul Steinhardt and Salvatore Torquato [8] have examined via numerical computations, different candidate classes of networks and heterostructures that could probably pursue a complete photonic band gap. For each candidate class, they optimized the microscopic properties of the selected networks, that are composed by spheres and circular rods with radius R each and with dielectric constant ε_2 embedded in a bulk with smaller dielectric constant ε_1. Then, for a fixed dielectric contrast, α (the ratio, $\varepsilon_2/\varepsilon_1$), they varied the values of the radius R (for spheres and rods), so they can compute the maximal value of the photonic band gap-to-midgap ratio $\Delta(\alpha)$, via an optimization algorithm. The optimal gap-to-midgap ratio has the form:

$$\Delta(\alpha) := \max_{R \geq 0} \left\{ \frac{\Delta\omega}{\omega_m}(R, \alpha) \right\} \tag{11}$$

By plotting the maximal gap-to-midgap ratio $\Delta(\alpha)$, versus the different dielectric contrast values α, for each candidate three-dimensional (3D) network, in the same plot, Klatt et al., found out that there is a hidden universal behavior unraveling between the different network classes (disordered and classical ones, e.g. the diamond lattice). The comparison between the different networks was made with the plot that corresponds to the quarter-wave stack coating, mentioned earlier (a structure composed from parallel alternating planes/layers with dielectric constants ε_1 and ε_2, each with a thickness equivalent to a quarter of a wavelength, $\lambda/4$. This structure is characterized by an optimal volume fraction, ϕ). The key for revealing these universal behaviors is the gap sensitivity, denoted with $S(\alpha)$ and defined as:

$$S(\alpha) := \frac{d\Delta(\alpha)}{d\alpha} \tag{12}$$

Moreover the equation describing the gap-sensitivity for a one-dimensional quarter-wave stack is denoted by S_{QWS} and is given by:

$$S_{QWS} := \frac{2}{\pi} \frac{1}{\alpha^{3/4}(1 + \sqrt{\alpha})}, \tag{13}$$

the propagation of EM waves in the quarter-wave stack is perpendicular to the alternating dielectric layers.

The gap sensitivity plot ($S(\alpha)$ versus α, as can be observed in Figure 7) imposes that for sufficiently large values of dielectric contrast, α, for all the optimized crystals and heterostructures, the gap sensitivity converges to the quarter-wave stack value, $S(\alpha) \approx S_{QWS}(\alpha)$. This convergence exists, despite the topological differences, the absence or presence of long-range order and the symmetry of the different crystals and networks analyzed. Implementing a universal behavior across different structures, which could allow us, to reduce the complexity and construct materials with large photonic band gaps, in the foreseeable future.

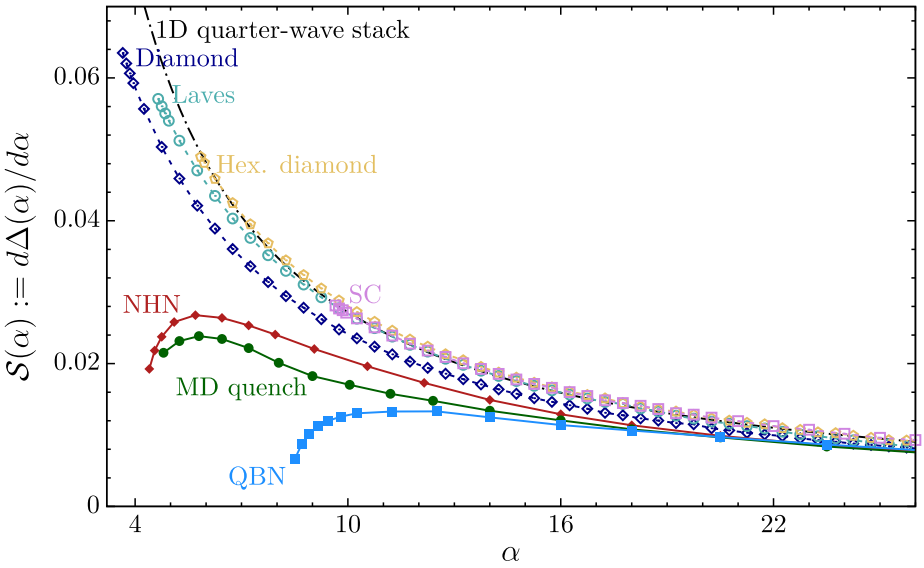


Figure 7: The gap-sensitivity plot shows the slope of $S(\alpha)$ (the derivative of the gap-midgap ratio) for each of the curves that correspond to the different lattice structures (e.g. **crystals**: diamond, Laves, hexagonal and **disorder networks**: NHN, QBNs (quantizer-based networks) MD quench (made with the use of molecular dynamics) etc.). All of the networks are 3D and the gap-sensitivity for the crystal-ones is well approximated by the equation describing the quarter-wave stack structure at every value of α. Whereas, for the disordered networks, $S(\alpha)$ has a maximum at low α values and converges to the quarter-wave stack law, only for larger α values. (Reproduced from Klatt et al. 2021 [8] with permission from the American Physical Society. © American Physical Society.)

1.4 Our goal

The goal of this thesis is to investigate two-dimensional (2D) photonic heterostructures made from disc-packing geometries characterized by simple cubic, triangular and hexagonal lattice symmetries. We present their band structures and we observe substantial photonic band gaps only for TM polarization. In addition to these periodic lattices, we investigate a disc-based structure generated from a stealthy hyperuniform point pattern, extending our analysis beyond periodic geometries to disordered systems. For these structures, we plot the gap-sensitivity curves alongside the analytical quarter-wave stack curve to assess whether the predicted universal behavior holds across different dielectric contrast values.

Then, we extend our research to 2D network structures, composed by discs and rods, which are described by microscopic parameters such as the disc- and rod-radii, r_{disc} and r_{rod} respectively. Subsequently, we look for the existence of a complete band gap and we try to validate the universality of gap-sensitivity in two-dimensions for a hexagonal and sc lattice structure. This case is not so straightforward as in three dimensions, due to the existence of TE- and TM-polarization modes. Each mode has its own band structure and we have to

check for an overlap in between these values. Moreover, each of these modes is favored by a specific geometry as we described in the previous paragraphs, and these geometrical features are competing for TE and TM PBGs. As a consequence, the topology of the dielectric network and the packing fraction may deform the heterostructure and destroy the allowance of a complete PBG. We need to come up with a better optimization algorithm, since the number of parameters that we need to optimize now is increased to two: r_{disc} and r_{rod}. Even more importantly, small changes in the radius r_{rod} of the slender rods may have strong effects on the complete PBG at high-dielectric contrasts. Therefore, we aim to provide and improve a resource-efficient optimization procedure and investigate whether the universal gap sensitivity also holds in two dimensions.

Furthermore, we like to combine our numerical results with analytical work to strengthen the theoretical basis for the design principles of 2D photonic materials. However, rigorous results for PBGs are beyond the scope of a master thesis. Therefore, we here focus on hyperuniformity of 2D materials and pose the question whether we can obtain them from a slice of a 3D material.

2 Photonic band gaps in discs and networks, heatmaps & more

On this section, we will describe photonic crystals made from dielectric discs or networks that obey a variety of symmetries. In our case, we will employ three types of symmetries characterizing the crystals: **simple cubic (sc)**, **triangular** and **hexagonal** lattice symmetries. For each case (discs and networks) we will explore when a band gap occurs and why we do not have a complete band gap for the dielectric disc structures. Moreover, we will explore the connection between the microscopic parameters (radius and dielectric contrast) and we will present when a complete band gap occurs in the network structures with the assistance of heatmap plots.

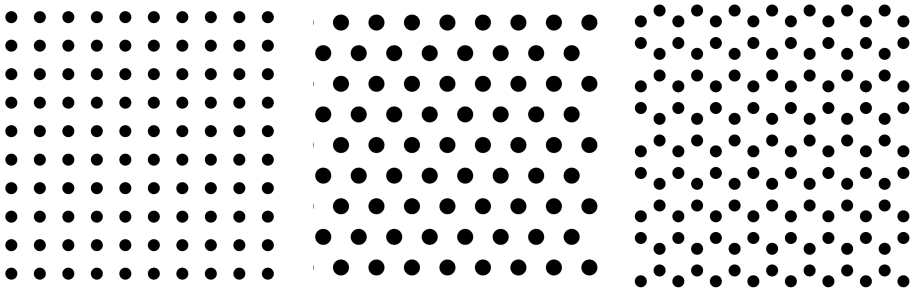
2.1 Disc packings

In this paragraph, we will use the MPB-software to solve the Maxwell equations, for disc-like photonic structures, for the characteristic geometries mentioned in Figure 8. Although it is possible to construct photonic materials with non-crystallographic symmetries, like photonic quasicrystals [17], for this work we will focus only on basic crystallographic structures with hexagonal, triangular and simple cubic lattice symmetries.

Let us now analyze our methodology: how we extract data (only TM-polarization modes and frequencies are important for the discs), from MPB-software and we use them to create band structures and gap-to-midgap ratio as a function of r_{disc}, plots.

We use the Scheme language environment of the MPB-software in order to solve the Maxwell equations. So, we employ already written scheme-codes that define the mesh size, and specifies that master equation can be broken down into two type of solutions, TM and TE polarization (or run-TM and run-TE in the MPB language). Then we construct a bash-file (a code that works under bash command language), that is basically the "core file" which produces the modes (expected solutions), for each specified geometry.

The bash-file contains the most important information that defines the solutions we will receive: the dielectric contrast values, the geometry, the symmetry and the number of bands (which specifies how many eigenmodes/frequencies you need to compute at each k-point, so in a band structure plot, the n=1 band is the $\omega_{1,k}$ function, computed for example at 100 k-points. If you "connect" the dots corresponded to each k-value, you derive one band). Moreover in the bash-file we define the mpb-tolerance, the resolution, the lattice constant ($a_\ell = 1.41421356237$ for the hexagonal lattice and $a_\ell = 1.0$ for the triangular and simple cubic lattices) and the number of k-values that we need to interpolate for our solution. Everything is saved in output files of two forms: ".out", which contain more information of how equations are solved for specified parameters and ".dat" files that correspond to the mode values for each k-point. Because we need to make use of the bash-file each time for a different geometry, we em-



(a) Simple-cubic lattice (b) Triangular lattice (c) Hexagonal lattice

Figure 8: MPB representations of the packing geometries used for two-dimensional photonic crystals composed of **dielectric discs** (black). The geometries were extracted from the HDF5 files generated by MPB.

ploy the use of configuration files (and specifically JSON-files), which include all the values and specified geometries for the parameters that we have mentioned above (three configuration files, each for one of the Figure 8 geometries and only for TM-polarization).

2.1.1 Why we do not observe complete PBGs in disc packings?

As we have discussed above, disc-packing geometries favor the creation of TM-polarization band-gaps only. So we cannot observe a complete band gap, since TE-polarization band gaps are practically absent. In a 2D crystal, "TM" and "TE" modes behave in the structure differently. In the TM-polarization, the electric field has the form $(0, 0, E_z)$, so it moves across the dielectric rods, or in our case, it is concentrated along the dielectric discs. Therefore we experience a strong modulations of the dielectric constant around the discs and therefore strong Bragg scattering and a large band gap. Whereas, in the TE-polarization case, the electric field is confined in the plane, so while it propagates it has to satisfy continuity conditions on the boundaries of the discs, making it in that way much harder for the field to concentrate inside the dielectric discs. The TE-field is concentrated around the discs and so we have less confinement and weaker interactions with the dielectric part of the structure. So, in the band zone, where a band gap occurs for TM-polarization, there is propagation of light for the TE-polarization modes. Thus, we cannot observe a CPBG [2].

2.1.2 Computing TM gap-to-midgap ratios

Let us now unveil the methodology of how we computed the gap-midgap ratio values for different microscopic parameters (α and r_{disc}). First we used the data (".dat" files) where we have collected the modes (solutions of the Maxwell equations for the different k-values). These data are imported into a python script which contains a function that collects the frequencies from the ".dat" files and computes the gap-to-midgap ratio for a dual set of parameters (α, r_{disc}).

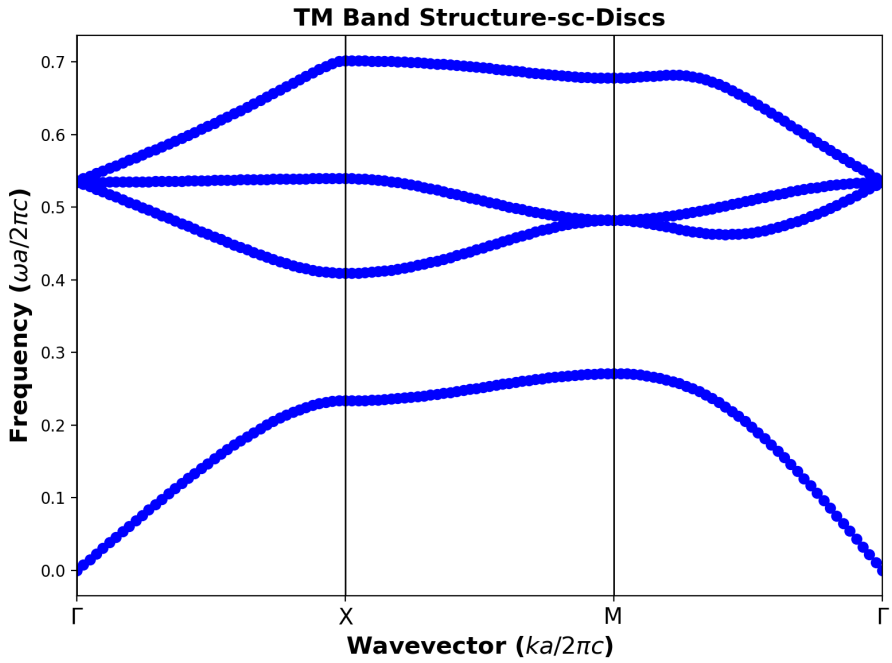


Figure 9: A band structure for TM-polarization for the simple cubic lattice symmetry. The calculation has been done for $r_{disc} = 0.2$ and $\alpha = 13.0$. We can clearly notice the band gap between bands 1-2, in this specific plot.

The function reads the (k, ω_n) and computes the difference $(\Delta\omega)$ by finding the maximum value of the band below the gap and the minimum value of the band above the gap and subtracting them. Then it computes the ω_m and it repeats the process for all the data. If the number of bands is four ($num_bands = 4$) then we derive three gap-midgap ratios and the code peaks up the highest one: it finds the maximum gap-to-midgap ratio for each set of values and assigns it to a new Python matrix. All of the data are saved in csv-files (printed in a table form), with a name corresponded to the geometry used for the chosen lattice. One example of these tables and the gap-to-midgap ratio values computed for both TE- and TM-polarization, for a triangular lattice made of dielectric discs, can be seen on Table 1. The negative values, are due to the way the Python code is made. We could have substituted them with zero for convenience. Although it is clear that a negative value for a gap-to-midgap ratio (or a band gap) means that no band gap exists and the bands overlap, since $\Delta\omega < 0$.

Moreover, Table 1 imposes absent or very small values of TE band-gap in the dielectric disc structures. Especially in high dielectric contrast values ($\alpha = 13.0$) we can observe the high difference between the gap-to-midgap ratio value that corresponds to TM-polarization modes (around 40% gap) in comparison to the TE-polarization modes (mostly around 1% and only 9.6% gap for $r_{disc} = 0.25$).

α	r_{disc}	$\Delta\omega/\omega_m$ (TE)	$\Delta\omega/\omega_m$ (TM)
4.0	0.10	-9.03 %	3.05 %
4.0	0.25	-7.8 %	21.5 %
7.0	0.10	-8.8 %	17.8 %
7.0	0.25	-4.0 %	32.0 %
10.0	0.10	-10.02 %	29.3 %
10.0	0.25	0.9 %	36.5 %
13.0	0.10	-10.3 %	38.4 %
13.0	0.20	0.83 %	46.9 %
13.0	0.25	9.6 %	38.9 %

Table 1: Gap-to-midgap ratio $\Delta\omega/\omega_m$ for selected values of the dielectric contrast α and disc radius r_{disc}, for TE and TM polarizations in a triangular lattice of dielectric discs.

Next we will employ the data of the csv-files, and use them to construct plots of the gap-to-midgap ratio values versus the disc radius parameter. Figures 10–12 show the dependence of the gap-to-midgap ratio on the disc radius for the three considered lattice geometries. From these plots we can extract information about the dependence of the size of the gap with the microscopic parameters that constitute the dielectric lattice (r_{disc} and α). What we can actually observe is that the highest gaps occur in the case of the triangular lattice. Moreover, we realize that as we increase the dielectric contrast, we derive higher values for the gap-to-midgap ratio. So, as the dielectric contrast increases, the gap increases, or as the dielectric contrast decreases, the gap closes.

Another important information is that, in all the graphs, we can observe that the maximum value for the disc-radius, depends on the dielectric contrast. For higher dielectric contrast the maximum r_{disc} occurs around 0.2 in comparison with lower α values, in which we observe the maximum around 0.25.

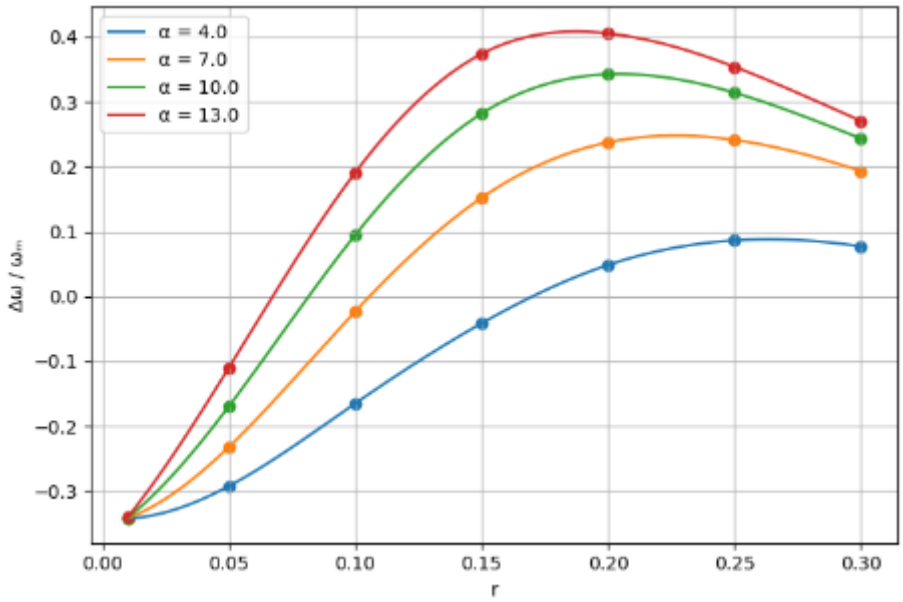


Figure 10: Gap-to-midgap ratio versus disc radius r for the simple-cubic lattice. The different curves correspond to the considered values of the dielectric contrast α.

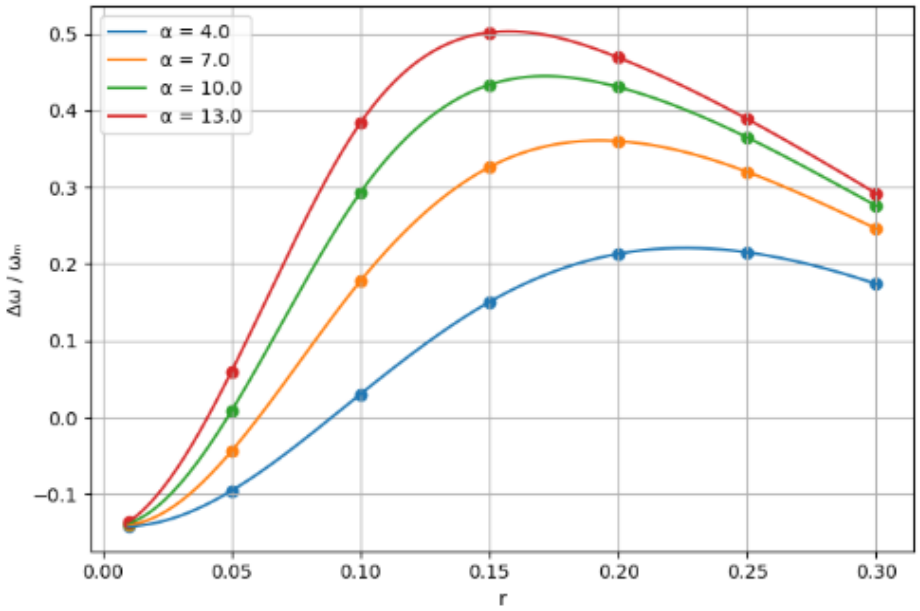


Figure 11: Gap-to-midgap ratio versus disc radius r for the triangular lattice. The different curves correspond to the considered values of the dielectric contrast α.

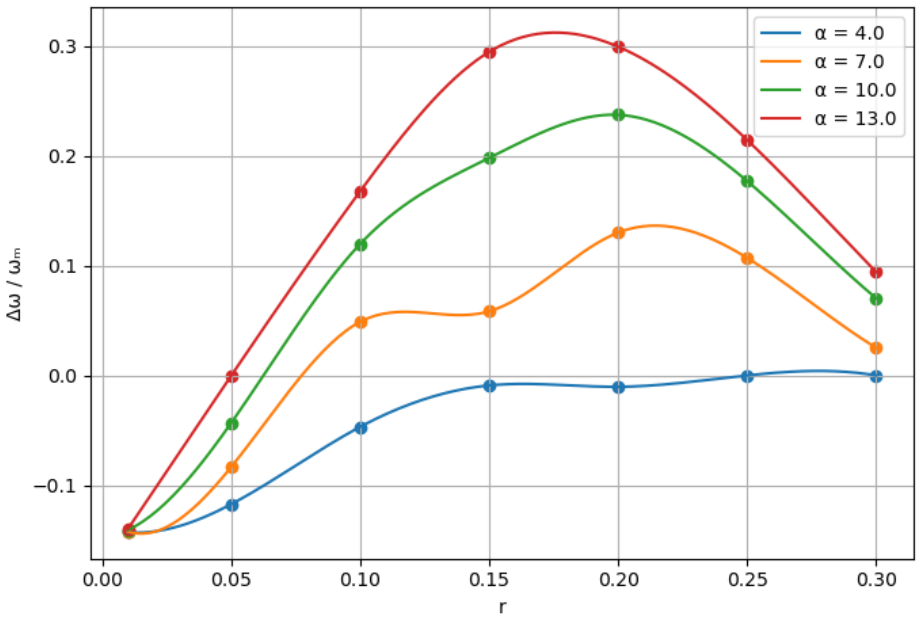
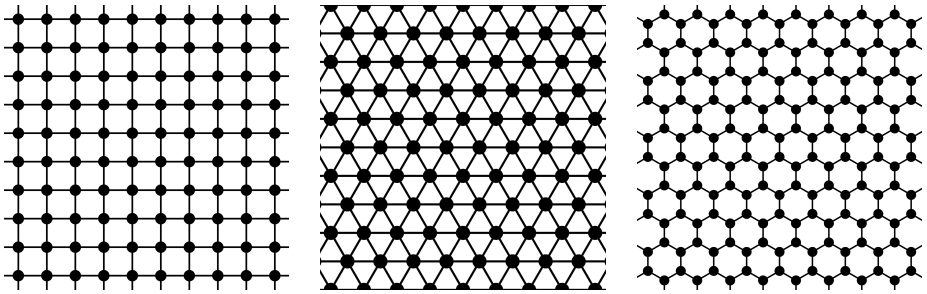


Figure 12: Gap-to-midgap ratio versus disc radius r for the hexagonal lattice. The different curves correspond to the considered values of the dielectric contrast α.



(a) Simple-cubic lattice (b) Triangular lattice (c) Hexagonal lattice

Figure 13: MPB-representation of the packing geometries that we use for two-dimensional photonic crystals made from **dielectric networks** (black color). The white color phase represents **air** with dielectric contrast, $\varepsilon = 1$. The EM-field can propagate through the dielectric channels (black color phase). The pictures were produced by creating, via specific commands, h5-files of MPB to png-files (images). Together with the modes and frequencies (solutions of Maxwell equation saved at .out and .dat files), we also receive an h5-file which encapsulates the geometry of the structure in which we solved the Maxwell equations.

2.2 Photonic networks

As we have discussed analytically in the previous paragraphs, in 2D systems, the structures favorable of TE-mode PBG and those for TM-mode PBG formation are different. This difference lies on the nature of the electric field (E) in both cases. In the TM-mode we have to deal with a scalar electric field $(0, 0, E_z)$, whereas in the TE-mode we have a vector field $(E_x, E_y, 0)$. So, in order to receive a complete photonic band gap, we need to create lattices that combine characteristics of both structures (TM-modes and TE-modes) [18].

Vein-dielectric structures (made from dielectric rods), are ideal for the creation of a TE-mode gap. In this case the continuous field lines of the transverse electric field, can extend to neighboring lattice cites without leaving the high-ε region of the lattice. For example, in the $n = 1$ band, the field could be localized in the high-ε and in the $n = 2$ band, the field "jumps outside", so energy is concentrated on a low-ε region. This "jump" in the frequency creates a band gap.

The difference with the isolated dielectric disc structures, is **connectivity**. The question remains, what are these network structures and why do we call them like that?

The combination of continuously connected dielectric rods with dielectric discs, create an interconnected structure characterized by bonds and connectivity as exactly it is happening with a mathematical graph. Although, here we do not have abstract nodes and edges, but dielectric rods and discs that constitute our **dielectric network**. Network structures, allow the construction of photonic crystals with enriched physical properties like light localization in a specific line, complex band structures and the most important: complete photonic band gaps (CPBGs). Moreover in order to observe light localization phenomena, we can construct 2D disordered network lattices. Extensive research in this subject

has been conducted by Florescu et al. [6], who has designed, with numerical computations, disordered lattices with large band gap values, by employing the notion of stealthy hyperuniformity and noting that the latter together with short range geometric order and local topology can form band gaps without the appearance of long-range order in the system.

In this paragraph, we will focus on the same geometric packing structures that we discussed for the discs and we will present our methodology for the computation of the gap-to-midgap ratios and the complete band gaps (see Figure 13).

2.3 Computing TE and TM gap-to-midgap ratios

The approach that we had to follow for the computation of the gap-to-midgap ratio for photonic network structures, is actually based on the same methodology used for disc-structures.

We save (from MPB-software calculations the corresponding bash-file that we have created for network-lattice geometries) and extract data (eigenfrequencies) computed for three types of dielectric networks (as we can observe in Figure 13). The bash-script is similar to the one used in the discs-case and extracts parameters such as the number of bands, the dielectric contrast and the radii from configuration files made for each lattice. We use the same algorithmic "core" for the python code that we have used for discs. However, we implement a new parameter, r_{rod}, which defines the radius of the rods that represent the connectivity of the network. A distinction between the polarization of the modes is defined through an if-else command. The output (data for the frequencies) is saved in ".out" and ".dat" files. The ".out" files contain all the information during the mpb-running procedure for specific values of the parameters (radii, dielectric contrast), e.g. solving for bands 2 to 4, and in $(cylinder, center) = (.., ..)$ with te/tm frequencies = (...), for k-points. Moreover, they contain the gap values (in %) computed between different bands (e.g. *Gap from band 2 to band 3*). However, we are not going to use these values for our analysis and we will compute the gap-midgap ratio via a python code, as we have exactly obtained in the disc-structure crystals. Our next step is to load the ".dat" files in the python code (compute-gap-table-networks.py), which computes the gap-midgap ratios for each dielectric contrast and for specific radii (r_{disc} and r_{rod}) defined in the configuration file (JSON-file) which is about to be used. The output is saved on "csv-files", each associated with a name that corresponds to the existing lattice structure and polarization ("gap-results-networks-hex-te/tm.csv"). Selected values of the gap-midgap ratio are presented in the following tables, for a hexagonal, simple cubic and triangular lattice respectively.

The values presented on the tables are taken from tables with 197 gap-to-midgap ratio values for each lattice. For the first two dielectric contrasts ($\alpha = 4.0,\ 7.0$), we picked up the highest gaps that occur for TE-polarization and for the equivalent radii, we check the value for TM-polarization. Whereas, for dielectric contrasts, $\alpha = 10$ and $\alpha = 13$ we picked up the highest gap values for both polarizations and we compared them (this is why we chose to have 2

α	r_{rod}	r_{disc}	$\Delta\omega/\omega_m$ (TE)	$\Delta\omega/\omega_m$ (TM)
4.0	0.15	0.25	20.05%	0.019%
7.0	0.15	0.15	37.17%	0.059%
10.0	0.15	0.15	47.26%	0.063 %
	0.01	0.20	1.46%	22.35%
13.0	0.10	0.15	55.25%	2.40%
	0.01	0.20	28.24%	7.98%

Table 2: Gap-to-midgap ratio for selected values of the dielectric contrast α and the radii r_{rod} and r_{disc} in a network structure with hexagonal packing geometry. The gap-to-midgap ratios are given for both TE and TM polarizations.

α	r_{rod}	r_{disc}	$\Delta\omega/\omega_m$ (TE)	$\Delta\omega/\omega_m$ (TM)
4.0	0.01	0.30	0.0%	6.6%
7.0	0.10	0.15	12.2%	3.1%
10.0	0.10	0.15	23.6%	2.95%
	0.01	0.20	0.0%	30.24%
13.0	0.15	0.10	21.92%	0.02%
	0.01	0.20	0.15%	35.96%

Table 3: Gap-to-midgap ratio for selected values of the dielectric contrast α and the radii r_{rod} and r_{disc} in a network structure with simple-cubic packing geometry. The values corresponding to $\alpha = 4.0$ are originally negative; since a negative gap has no physical meaning, these values are reported as zero.

α	r_{rod}	r_{disc}	$\Delta\omega/\omega_m$ (TE)	$\Delta\omega/\omega_m$ (TM)
4.0	0.10	0.30	4.68%	0.98%
7.0	0.10	0.30	12.53%	3.62%
10.0	0.05	0.20	19.19%	16.42%
	0.01	0.20	0.0%	36.13%
13.0	0.05	0.20	24.27%	17.88%
	0.01	0.20	0.0%	39.53%

Table 4: Gap-to-midgap ratio for selected values of the dielectric contrast α and the radii r_{rod} and r_{disc} in a network structure with triangular lattice geometry. The gap-to-midgap ratios are given for both TE and TM polarizations.

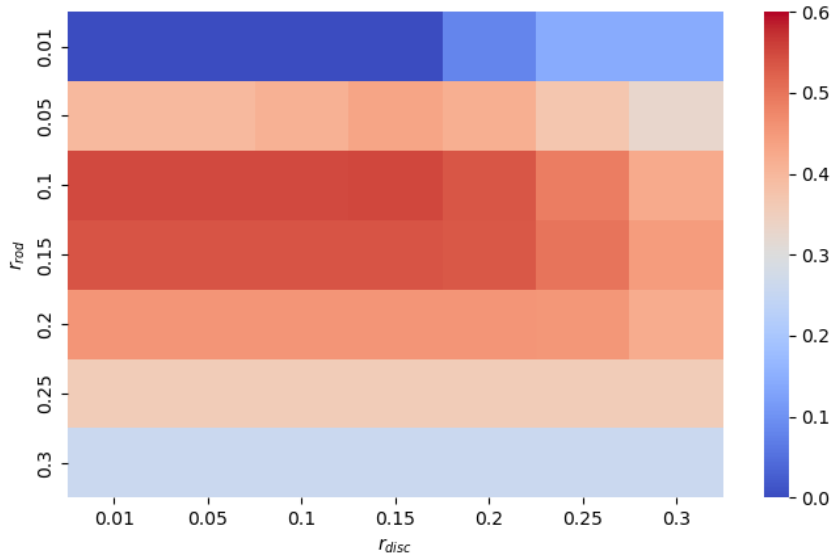


Figure 14: Heatmap of the gap-to-midgap ratio for the hexagonal lattice in TE polarization at dielectric contrast $\alpha = 13.0$. The red regions correspond to higher gap-to-midgap ratios, whereas the blue regions correspond to smaller values.

gap-values for the highest dielectric contrasts).

Given those tables, we can observe that smaller dielectric contrasts require larger radii values. Moreover, as α increases, the gap-values also increase. From the data, we can also understand that the gap-values for TE-polarization are not relevant with the values of TM-polarization for the same parameters (radii and α). The absence of a gap for TE could mean a large gap for TM (as we can deduce from the last row of table 4). The reason is the geometry of the lattice and the adjustment of the radii values. Increasing the r_{rod} favors TE-polarization, since it creates more "routes" where light can propagate inside the network. Whereas, higher r_{disc} values allow TM-modes to increase their gap, since the "routes" are closing and the packing becomes more rigid (more information about packing and crystal structures can be found here: [19]). The fact that TE-gap values differ from TM-gap values, predispose us to the idea of complete photonic band gaps (CPBGs) which we will analyze in the next section. Before CPBGs, we will continue our preliminary analysis by presenting some 2D heatmaps plots of the gap-midgap ratio versus r_{disc} and r_{rod}. These plots provide a hint for the radii at which the maximum gap occurs, an important aspect for the optimization procedure that will follow up, for different lattice geometries.

Here we provide 3 different heatmaps, one for each lattice geometry, corresponding to TE-polarization and for $\alpha = 13.0$. More information about the heatmaps produced for the different geometries and polarizations can be found in Appendix A.

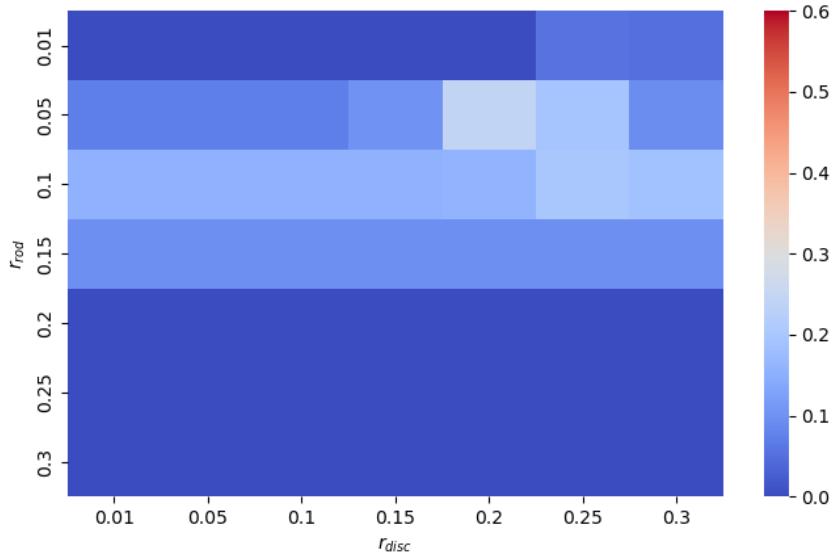


Figure 15: Heatmap of the gap-to-midgap ratio for the triangular lattice in TE polarization at dielectric contrast $\alpha = 13.0$. The red regions correspond to higher gap-to-midgap ratios, whereas the blue regions correspond to smaller values.

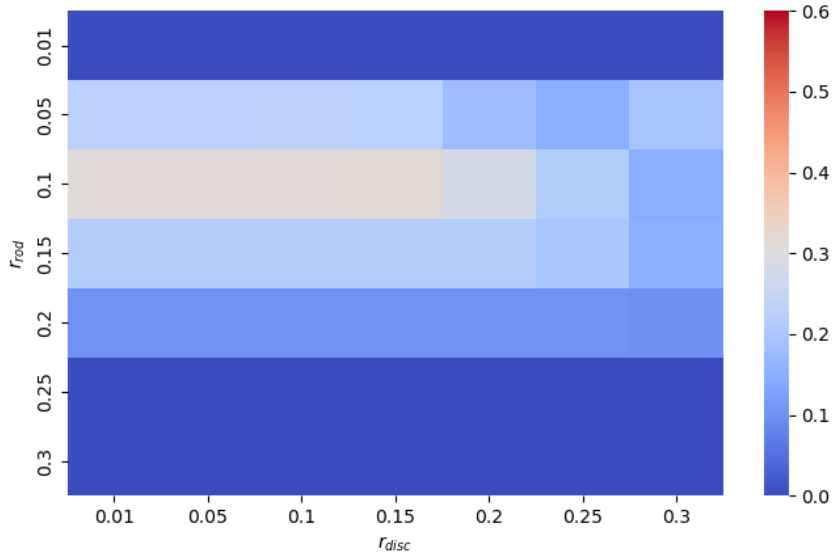


Figure 16: Heatmap of the gap-to-midgap ratio for the simple-cubic lattice in TE polarization at dielectric contrast $\alpha = 13.0$. The red regions correspond to higher gap-to-midgap ratios, whereas the blue regions correspond to smaller values.

At $\alpha = 13.0$, the hexagonal lattice exhibits substantially higher TE gap-to-midgap ratios than the triangular and simple-cubic lattices, as shown in Figures 14–16. The connected topology of the hexagonal structure modifies the spatial distribution of the electromagnetic fields and the coupling between the photonic bands, which can contribute to wider TE gaps. Moreover, we can observe again that an absence of gap at a specific dielectric contrast for TE-polarization, does not imply an absence of gap for TM-polarization modes (as shown in Table 4).

2.4 Complete PBGs

Let us now focus on the complete band gaps and how we compute them. The methodology developed for the computation of complete photonic band gaps (CPBGs) is described in the following section.

2.4.1 Complete PBGs in networks: methodology

Our approach is based on the ".dat" files created by MPB, for the gap-midgap ratios for TE- and TM-polarization, for each lattice geometry, and for dielectric contrast $\alpha = 4.0, 7.0, 10.0, 13.0$. We construct a python code which loads, via configuration files, the frequencies available in the ".dat" files for TE- and TM-modes. This python code, loops over all the parameters (radii and α) and uses a function, that finds all the gaps for TE (te-gap 1, te-gap 2, ...) and TM (tm-gap 1, tm-gap 2, ...) and then compares them with each other, in a for loop and searches for overlaps in the frequency gaps between the two modes.

For this algorithm, we use a function named: get-all-gaps, which reads the frequencies from the ".dat" files and finds the maximum value (frequency) of the lower band and the minimum value of the upper band. Then it computes the gap-midgap ratio for all the gaps between consecutive bands. More specifically, a variable bands is assigned the values of the columns including the band frequencies data. Then two variables max-lower and min-upper, find the maximum frequency of the band below the gap and the minimum frequency of the band above the gap, respectively. Also we define an empty array: gaps. Then we loop over all possible values of max-lower (it would be the same if we have looped through min-upper). Inside the loop values are assigned to two new variables lower and upper (from max-lower and min−upper, and for all i) and we compute the gap difference (gap=upper-lower). After, if gap is a positive value, we compute the mid-frequency (mid=upper+lower/2). Finally, all variables and the band-index (i+1), are assigned to a list named, gaps.

2.4.2 Heatmaps for complete PBGs

The gap-to-midgap ratios produced for the complete-polarization, are saved on three csv-files, one for each polarization. The csv-files are then loaded into the Python code used to generate the heatmaps (seaborn library is used for the data visualization), allowing us to obtain heatmaps of the complete band gaps. The

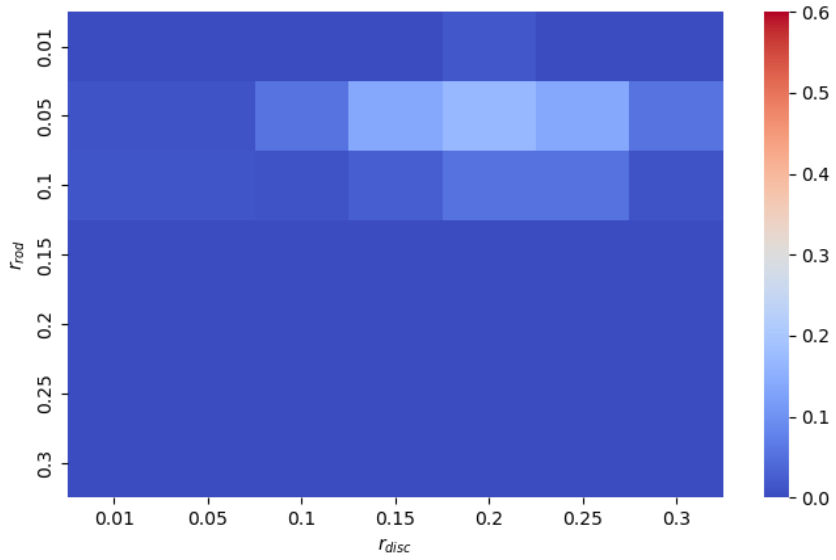


Figure 17: Heatmap of the gap-to-midgap ratio for complete polarization in the hexagonal lattice at dielectric contrast $\alpha = 13.0$.

following heatmaps represent the occurrence of complete photonic band gaps on the three different lattice geometries, for a pair of radii (r_{rod}, r_{disc}) and for dielectric contrast, $\alpha = 13.0$:

The complete band-gap heatmaps for the three lattice geometries are shown in Figures 17–19. The hexagonal lattice exhibits a broader range of gap-to-midgap ratios across the parameter space. In contrast, the triangular and simple-cubic lattices show gap-to-midgap ratios that are concentrated around two distinct values. In the triangular lattice, two different gap-to-midgap ratios can occur for the same rod radius, whereas in the simple-cubic lattice, two different values can occur for the same disc radius.

More heatmaps for the complete-polarization gaps are presented in Appendix B. Nevertheless, a preliminary inspection of Figure 17, together with the heatmaps in Appendix B, suggests that the largest gap values, and consequently the optimal radii, are obtained at dielectric contrasts around $\alpha = 13.0$. This observation motivates further investigation of dielectric contrasts around $\alpha = 13.0$, which may provide additional opportunities for optimizing the band gaps.

The heatmaps produced constitute the first step of our preliminary investigation into the maximum gap-to-midgap ratios for complete polarization. They provide an initial assessment of the optimal lattice parameters (radii) corresponding to the largest gap-to-midgap ratios, and consequently, the largest complete photonic band gaps.

The optimization procedure for the network structures is presented in the following section. Before that, a separate section on the optimization of the

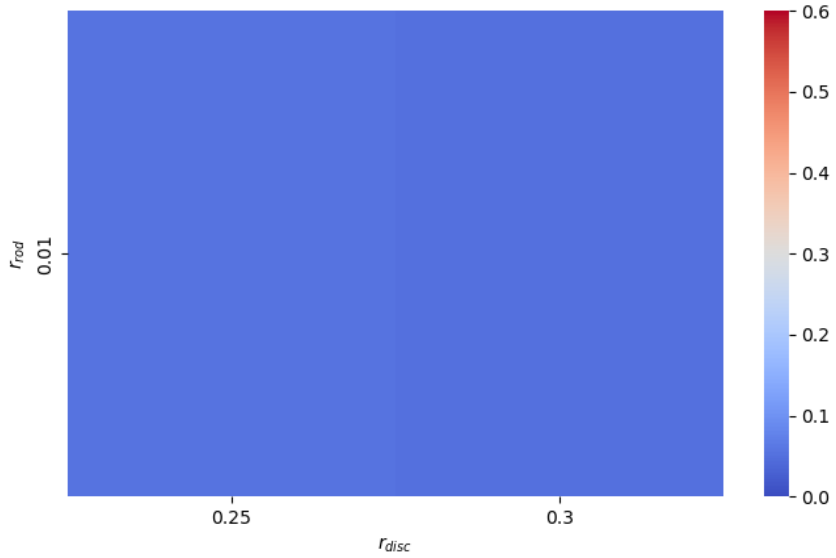


Figure 18: Heatmap of the gap-to-midgap ratio for complete polarization in the triangular lattice at dielectric contrast $\alpha = 13.0$.

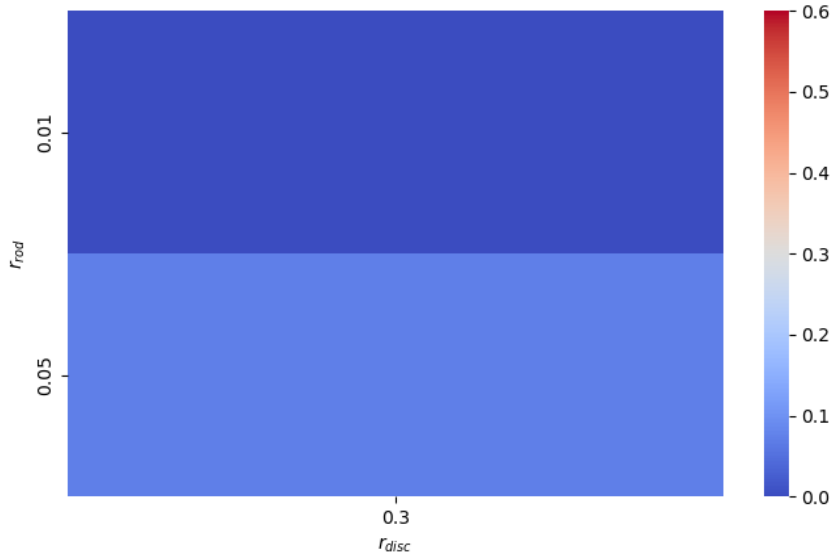


Figure 19: Heatmap of the gap-to-midgap ratio for complete polarization in the simple-cubic lattice at dielectric contrast $\alpha = 13.0$.

disc structures is analyzed. The latter methodology, which concerns lattice structures composed of dielectric discs, involves one fewer parameter and is based on "refined grid search" optimization method [20].

3 Optimization

The scope of this section is to describe the optimization techniques that have been used for photonic structures composed of, (1) dielectric discs and (2) dielectric networks. We first describe the refined grid search procedure used to optimize the disc-based structures, followed by the optimization of the network structures, which combines a refined grid search with Gaussian fitting to estimate the optimal radii and the corresponding maximum gap values. These optimization procedures are computational expensive, so our task is to develop simple optimization techniques that require limited computational resources while yielding valuable physical insights.

3.1 Optimizing 2D disc packings

For the optimization of lattices composed of dielectric discs, we will follow a process containing three steps. The first step of our optimization analysis is a rough grid search, and it has been obtained in the section "Discs", where we have computed the gap-to-midgap ratio and produced the gap versus r_{disc} curves. The curves presented on Figures 10 – 12, imply a first guess of the optimal discs radii. So, we collect 4 values for each lattice (one for each dielectric contrast) that represent the radius at which the maximum gap-value occurs. So, we create four tables of (α, r_{disc}) for the sc, triangular, hexagonal lattice, and the stealthy hyperuniform point pattern. These tables are used in a Python code, which fits a model to our existing data. The fitting model is the second step of our optimization procedure. It is described by an equation of the form: $r = b/\alpha + c$. Where α is the dielectric contrast and r is the disc radius. With b and c we define the fitting parameters. The fitting procedure is performed with curve_fit, from scipy.optimize library of python, which uses nonlinear least squares to fit a function ($f = b/\alpha + c$) on the $(x, y) = (\alpha, r_{disc})$ data that are represented by arrays including four values. An example of this fitting is given in Figure 20. We apply the same procedure to each of the lattices.

The last step involves, plugging the fitting parameters, b and c, into JSON files which include all the important information for each lattice: the resolution, the MPB-tolerance, the number of k-values interpolated, the number of bands and the band where the maximum gap is computed and the fitting parameters, b and c respectively. Then we use the information included in the JSON files, in a SLURM script which includes our optimization algorithm (a refined grid search method). With this method, we start from our initial guess and we compute maximum gap values and optimal radii. If the guess is not good enough, we refine a new grid around the produced set of parameters $(\alpha, r_{disc}^{(opt)})$, instead of searching the whole grid from the beginning. This method is computational

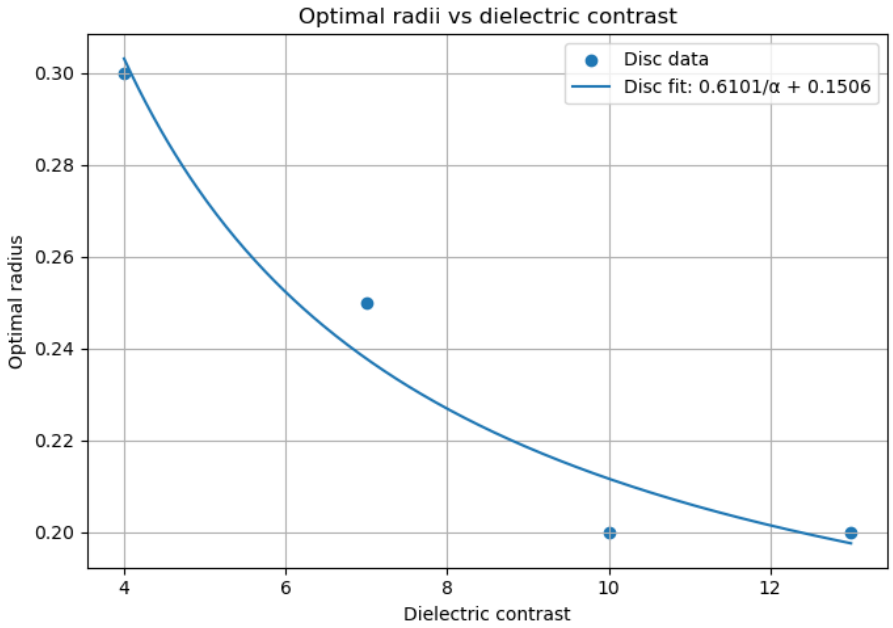


Figure 20: Fitting curve, regarding the model $b/\alpha + c$. The fitting parameters, b and c are represented on the upper right corner of the plot. The y-axis represents the radii, whereas the x-axis corresponds to the dielectric contrast values, α.

efficient. Later for the complete PBG, instead of "scanning" a lattice with 100 points in each direction (100×100=10000 points), we only have to search for a smaller region, e.g. 20×20. So, we "coarse-grain" our mesh. Moreover, the optimization algorithm, ran on cip-pool, at an LMU-cluster. Where, 16-nodes and 4-tasks-per-node are asked to be used. Each calculation lasted 16 to 18 minutes in total. However, the calculation corresponding to the stealthy lattice, lasted around 36 to 48 minutes, according to the number of dielectric contrasts and fitting parameters specified. For the hexagonal, simple cubic and triangular lattices, a resolution of 80 ($res = 80$) and 30 k-values were interpolated. In contrast, for the stealthy point pattern, k-interpolate was equal to zero and the resolution used, was equal to 30 ($res = 30$). Figure 21, provides a rough sketch of the refined grid-search optimization method.

After completing our optimization procedure, we collect the corresponding data for each lattice and we create two graphs: (1) the maximum gap-values as a function of the dielectric contrast, $\Delta(\alpha)$ and α respectively. And (2) the gap-sensitivity plot, $S(\alpha)$ as a function of α, where $S(\alpha)$ is the numerical derivative of $\Delta(\alpha)$. The key results for the gaps of three crystal lattices and one disorder structure (stealthy hyperuniform point pattern), are shown in Figure 22. In addition, Figure 23 represents the slope for the same lattices (gap-sensitivity plot).

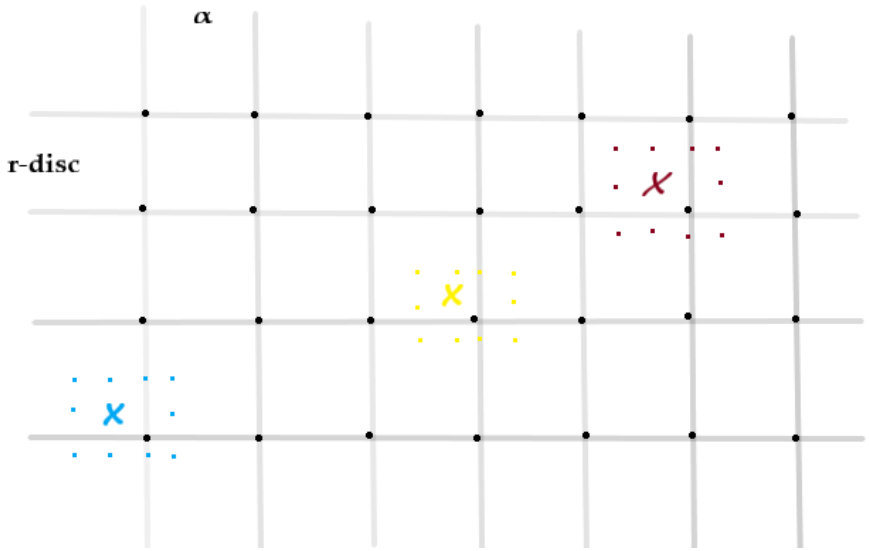


Figure 21: A rough sketch, that describes **refined grid search**. This is coarse grid, and the red x represents the point around we refine (which could be our initial guess for the optimal radii), for a region of high α values. The yellow mark is for intermediate values, whereas the blue mark corresponds to regions of low α values. The α and $r-disc$ on the axis, correspond to the dielectric contrast and disc-radii. A problem with this method is that if there is a narrow peak between two points, the coarse search may miss it completely. For a more extensive research, we can probably use a local optimizer, via Brent's method [21].

Figure 22 indicates that, the triangular lattice, appears to have the largest PBG. Moreover, for small dielectric contrasts, the stealthy pattern, has a larger PBG than the simple cubic (sc) lattice. Although, as we increase the dielectric contrast, the latter obtains larger PBGs. Both sc and stealthy lattices have different geometries, with the second one characterized by disorder. However, the symmetry that we use to obtain our calculations for the PBG values, acquires the use of simple-cubic structure. So, for both systems we use "a cubic box", where our calculations are obtained (same underlying periodic cubic cell). Although, the arrangement of points is different for both lattices. For the sc-lattice, the arrangement is crystal ordered and periodic, whereas for the stealthy-pattern, the points are generated according to a stealthy disordered point process and they do not form a simple cubic lattice. Moreover, the points on the stealthy pattern, are characterized by correlations, such that density fluctuations are suppressed in a region around $k = 0$ ($S(k) = 0$, for $0 < K < k$). This defines the hyperuniform identity of the structure and implies a hidden long-range order on the system. Thus, even though the system is characterized by disorder, the positions of points are not randomly independent. Furthermore, we can deduce from Figure 22, that **geometry specifies the PBG values**. Each lattice, has different gap values, with the hexagonal-lattice, having the lowest values. Even if its geometry is composed of two triangular shifted lattices, this shift is enough

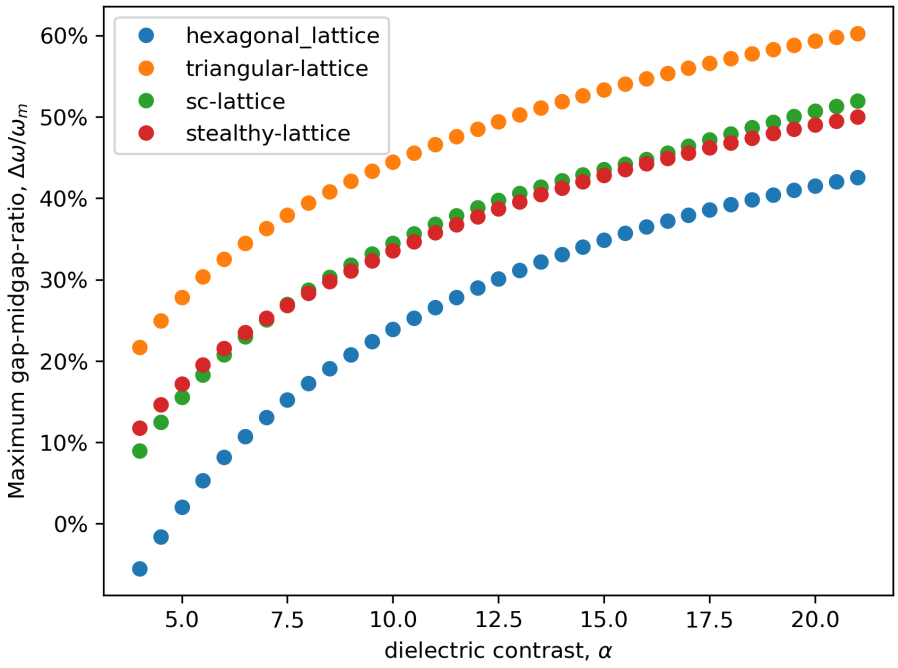


Figure 22: The gap-plot shows the optimum gap-to-midgap ratio, $\Delta(\alpha)$ as a function of the dielectric contrast, α. The plot compares 2D PBGs of crystal structures (yellow, blue and green) with a stealthy disorder structure (red). The values on the y-axis are expressing the gap-values.

for opening a lower PBG in comparison with the triangular lattice.

Next, we will focus our attention on the gap-sensitivity plots of these optimized disc-lattices. All simulations were performed for dielectric contrasts $\alpha = 4.0 - 21.0$, with a 0.5 step. Turning to Figure 23, we note that, for all our crystal lattices and the disordered structures considered, $S(\alpha)$ is well approximated by the gap sensitivity of the quarter-wave stack (QWS), $S_{QWS}(\alpha)$, for large values of α. Overall, it is a very nice fit, with a small deviation appearing on larger α, in the tail of the $S_{QWS}(\alpha)$ curve. However, it is not yet clear whether this deviation is due to the optimization tolerance or the numerical tolerance of the MPB eigensolver. Furthermore, the resolution used for the simulations is limited by the computational resources available on the cluster. Increasing the resolution, could probably offer better results and remove the deviation appearing on large dielectric contrasts. Moreover, our cross-checks suggest that the observed deviation could reflect a genuine physical effect. Nevertheless, we remain cautious in our interpretation, as the computational resources available to us do not allow us to extend our analysis further and establish this conclusion more firmly.

Furthermore, to extend our analysis, we compute the difference between the gap-sensitivity of the quarter-wave stack and the gap-sensitivity data for each lattice (crystals and the stealthy pattern) and plot the results together in Figure 24, where we observe that all curves approach the same positive offset for the largest values of α studied here. This finding suggests that, only at very large dielectric contrasts, beyond $\alpha = 13$, we observe a convergence to the universal curve with a small positive offset remaining even for $\alpha = 21$. Whether this offset is a real phenomenon or an optimization issue, remains an interesting open question for future research and would require substantial computational resources beyond the scope of this Master's thesis.

The close similarity to the universal gap sensitivity can hardly be a coincidence. Hence a similar physical law apparently applies. On the other hand, we found no obvious numerical explanation of the small offset. Taken together, these observations point towards a universal law that is modified in two dimensions possibly because the gap size is optimized for all in-plane directions but only for a single polarization (TM). However, we are cautious to make such a claim because of our limited computational resources. Further high-performance calculations are needed to verify this claim.

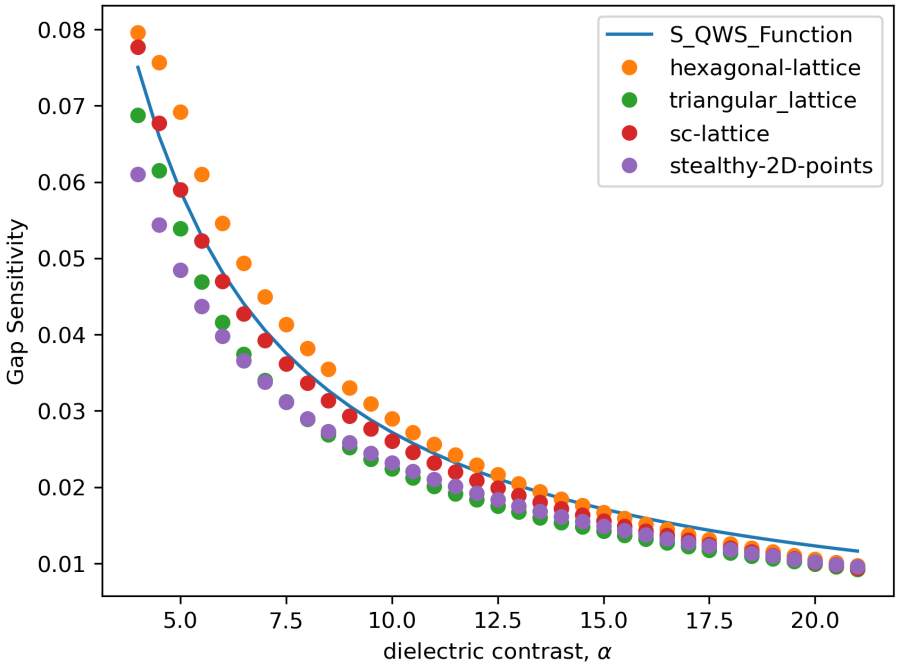


Figure 23: The gap-sensitivity plot shows the slope, $S(\alpha) := \frac{d\Delta(\alpha)}{d\alpha}$ for each of the curves on Figure 22. The blue line, corresponds to the 1D quarter-wave stack (QWS) PhC. All the lattices, are well approximated by the QWS curve, especially for larger values of dielectric contrast. However there is a small deviation on the tail of the curves, that may be plausible as a result of low resolution or MPB-tolerance used for the simulations.

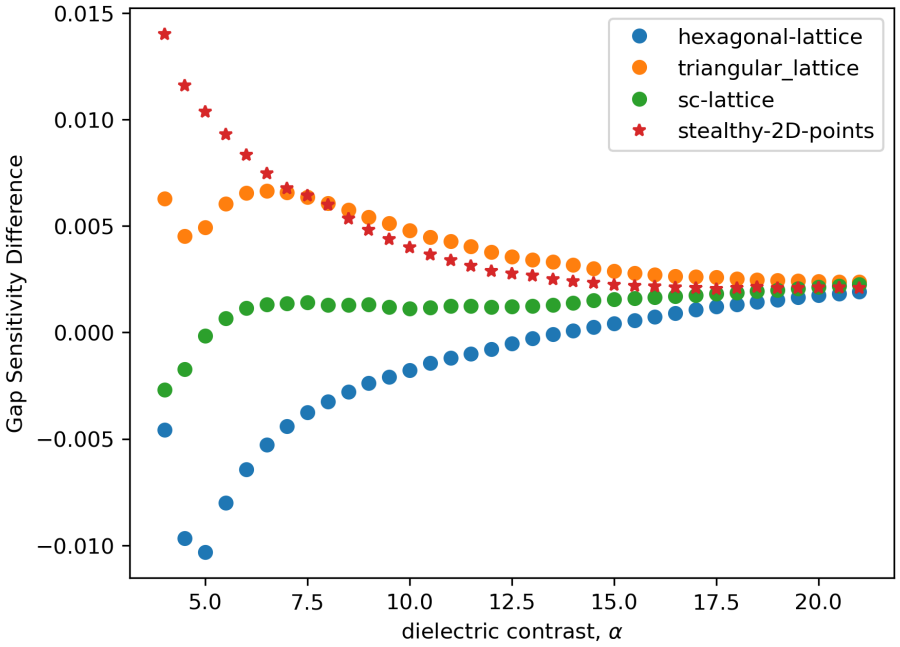


Figure 24: The difference $S_{QWS}(\alpha) - S(\alpha)$ of gap-sensitivities for each of the curves of Figure 23. However, here we do not plot the data of the gap values and the S_{QWS} separately. We plot the difference of the analytical quarter-wave stack equation with the gap-values for each of the corresponding lattices. We can observe that all lattices converge to the same offset for $\alpha \approx 21$. Moreover, $S_{QWS}(\alpha) - S(\alpha)$ increases for low α, for the crystal lattices. For the hexagonal-lattice, it keeps increasing until it reaches the offset.

3.2 Optimizing 2D photonic networks

The optimization procedure that we will follow for the network structures, includes four steps. The first step is a rough grid search (the same procedure as for the TM-polarized disc structures). For the photonic networks, we turn our attention to CPBGs because we need to optimize the geometrical parameters of the lattice structures to obtain complete gaps that prohibit light propagation in any direction. A quick look at the heatmaps of CPBGs presented on Section 2.4.2 and Appendix B, provide us with a first guess of the optimal radii. So, we proceed exactly as in the discs case, by collecting the data in tables containing sets of candidate optimal radii, r_{disc} and r_{rod} together with the corresponding dielectric contrast values, α. The following procedure is described for three types of network lattices: simple cubic, triangular and hexagonal. Unfortunately, the data for the triangular lattice were insufficient, as calculations were performed only for a dielectric contrast of $\alpha = 13.0$. Therefore, the available data were insufficient even to obtain an initial estimate of the optimal radii. Evaluation and MPB calculations of bands at higher dielectric contrast is probably needed. Thus, we followed our analysis with data for the simple cubic and the hexagonal lattice. The fitting parameters now are not only two but four, since we use the data on a Python code that used curve_fit from Python library scipy.optimize, and we obtain 4 values: b_{discs}, c_{discs}, b_{rod} and c_{rod}. These parameters are written into the corresponding JSON files, which contain the information required by the optimization algorithms for each lattice. The next step involves refining the grid around the initial estimates of the optimal radii. The JSON files are read by a SLURM script that runs the optimization procedure for the network structures. During this procedure, a Gaussian function is fitted to the gap values obtained from the refined grid search. As illustrated in Figure 25, the gap values around the maximum exhibit an approximately Gaussian-shaped profile. The Gaussian fit is therefore used to estimate the location of the maximum and the corresponding optimal radii, r_{disc} and r_{rod}, while reducing the influence of fluctuations in the sampled data. This procedure provides an estimate of the maximum gap and the associated optimal radii.

Furthermore, during the "refine grid" procedure, we observed that the data of the optimal gaps, are subjected to noise. To tackle the noisy data landscape, we plug our results for the gap values (which have been obtained by running on the LMU-cluster, the SLURM script for the optimization of networks) into a Python code, which uses spline-fit for smoothing (4th-step). More specifically, we use the `make_smoothing_spline` function from the Python module `scipy.interpolate`, setting the smoothing parameter to $\lambda = 1$. This function constructs a smoothing spline that balances agreement with the input data against the smoothness of the resulting curve. The spline fit provides us with smoothed estimates of the optimal radii, (r_{disc}, r_{rod}). More specifically, we obtain two arrays of data: one containing the disc radii and the other containing the rod radii. These data are then written into new JSON files, which are used by another SLURM script (`mpb_run_networks_hpc_2`). This script uses MPB to solve the eigenvalue problem derived from Maxwell's equations for the hexag-

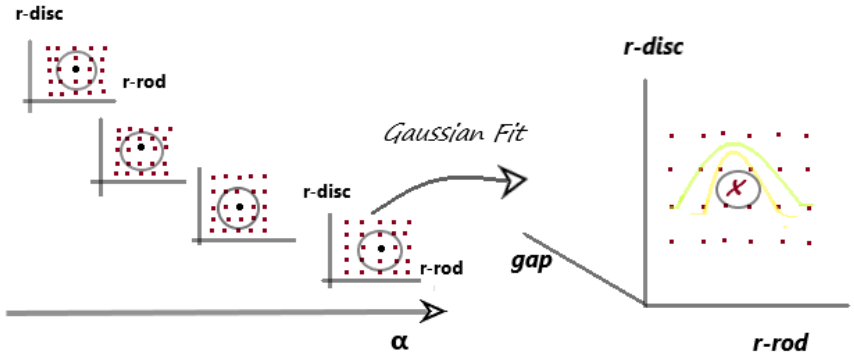


Figure 25: Gaussian fit on the optimal values that have been obtained via a refine grid search. Around the initial guess, a new grid is refined and then a Gaussian function is fitted around the gap values corresponding to the optimal radii. With "x" in red color we define a random optimal value of the grid, where we apply the Gaussian fit.

onal and simple cubic geometries and calculate the corresponding frequencies and CPBGs. We begin our analysis with the hexagonal lattice. The JSON files, specify the polarization setting (complete), the geometry, the symmetry of the lattice and the dielectric contrast values (α), used to solve the master equation. The output of the MPB eigensolver also provides the gap-values as percentages (e.g. 10% gap). We collect the gap values and the corresponding optimal radii, for dielectric contrasts ranging from $\alpha = 7.0$ to $\alpha = 13.0$ (our preliminary analysis, with the heatmaps, has indicated the absence of CPBG at $\alpha = 4$ for the hexagonal lattice), in increments of 0.2.

Our initial optimization procedure, has been obtained for $k_{int} = 10$ and $res = 80$. These parameters were used to produce the gap values with the MPB eigensolver script. However, the resulting data exhibited substantial scattering and deviated from smooth curves in the gap and gap-sensitivity plots. We found that the number of interpolated k-points affected the scattering. Increasing this number reduced the scattering in the optimized data. We therefore repeated the procedure from Step 3 using $k_{int} = 75$ and $res = 130$. We then followed the same procedure to obtain new data for our gap and gap-sensitivity plots.

On Figure 26 and Figure 27 we observe the gap (only for hexagonal-lattice) and gap-sensitivity plot (for hexagonal- and sc-lattice), respectively. The latter, indicates that there is no overlap between gap sensitivity of the data $S(\alpha)$ and $S_{QWS}(\alpha)$. Moreover, we observe a "kink" in the data, for $\alpha = 12.6$. The optimal radii that correspond to the "kink" are written down on Figure 27. Since the kink appears for both lattices close to the largest values of α that we can consider here, it may be an artifact of our optimization procedure. Note that gaps at non-optimal radii are smaller and can hence lead to a drop in the gap sensitivity. The appearance of the "kink" in the gap-sensitivity plot,

is possibly produced due to the decreasing of the slope of optimal rod radii, as α increases. In addition, the non-convergence of our data to $S_{QWS}(\alpha)$, is connected with the wall-thickness of the rods (or equivalently $2 \times r_{rod}$), that constitutes the network lattice. As we increase the dielectric contrast, the wall-thickness decreases, and the necessary change to optimize is may no longer be represented by the pixelated image.

Furthermore, we continue our analysis, for the sc-lattice. We follow the same procedure as in the case of the hexagonal. However, for this structure, the optimization procedure produced data only for $12 \leq \alpha \leq 13$ with step 0.2. The absence of data, does not allow us to extract more information for the simple cubic lattice. We tried to create gap-values for higher values of dielectric contrast, but the optimization procedure, ran on the HPC, stuck and did not provide us with an output. Although, we did not smooth our data (for sc), we plot them on the gap sensitivity plot, together with the hexagonal-lattice data. The important thing is, the observation of the same "kink" in the simple cubic lattice, for $\alpha = 12.6$. Figure 27 represents the gap-sensitivity plot for the optimal data of hexagonal and sc lattices. Only three data are trustworthy for the simple cubic lattice, the other three are not taken into account (as explained above).

Another important reason for the substantial quantitatively deviations, is the different geometrical requirements of the TE and TM band gaps. The two polarizations respond differently to the dielectric geometry: TM modes tend to favor isolated dielectric inclusions, such as dielectric discs, whereas TE modes generally benefit from connected dielectric networks or vein-like structures. This competition between the geometrical requirements of the two polarizations makes the simultaneous optimization of TE and TM band gaps more restrictive than optimizing either polarization separately. This argument, together with the limitations imposed by the finite pixel resolution of the rod wall thickness, are a possible, rough explanation of the deviation of data from the analytical curve, $S_{QWS}(\alpha)$. These observations further motivates a more detailed investigation of the mechanisms underlying the emergence of photonic band gaps in optimized two-dimensional network structures.

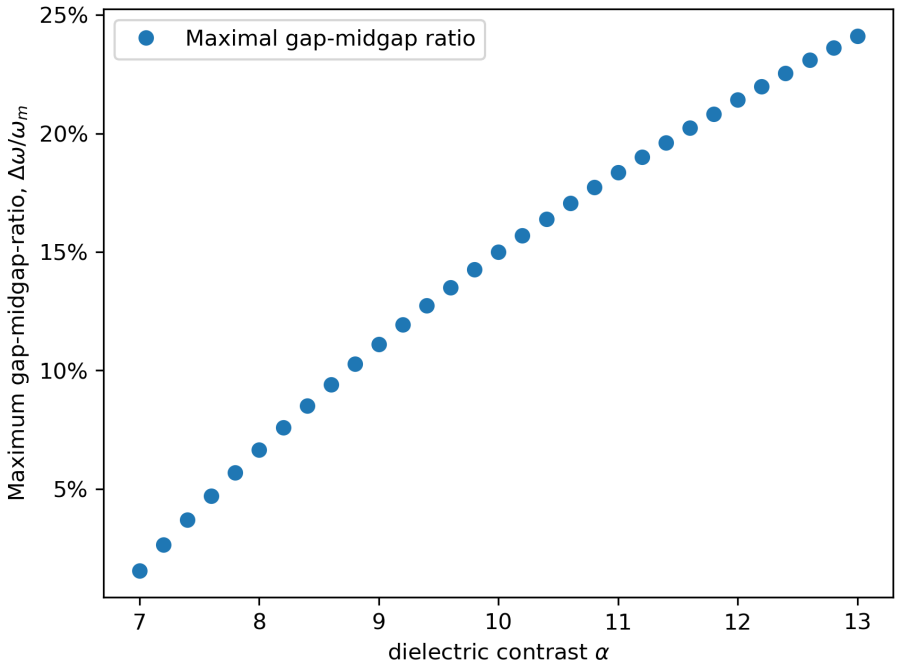


Figure 26: The gap plot for a hexagonal-lattice network. $\alpha = 7$, is roughly the critical value for the appearance of a CPBG. The gap shows the optimal gap-to-midgap ratio $\Delta(\alpha)$ as a function of the dielectric contrast α.

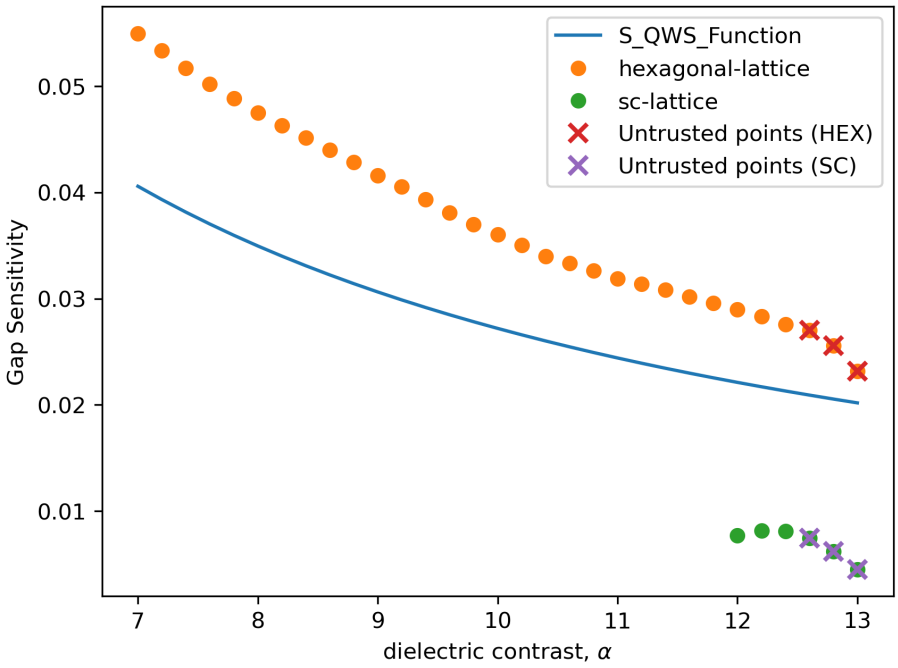


Figure 27: The gap-sensitivity plot for the hexagonal and simple cubic lattices. It has been obtained for $res = 300$ and $k_{int} = 75$. We can clearly observe that despite the high resolution, the data do not converge towards the quarter-wave stack curve for gap-sensitivity. On $\alpha = 12.6$, we have a "kink" in the hexagonal-lattice data, that corresponds to optimal values: $r_{rod} = 0.026$ and $r_{disc} = 0.199$. The points appearing directly at and after the "kink" are not trustworthy and so are "deleted". For the sc-lattice, on $\alpha = 12.6$, the "kink" appears. This corresponds to optimal radii: $r_{disc} = 0.327$ and $r_{rod} = 0.028$. The untrusted points are "deleted", with an "x" symbol, for both lattices.

3.3 Remarks on optimization processes

The steps that have been followed for the optimization processes, for dielectric disc and network structures provide us with some important remarks about PBGs on 2D photonic heterostructures. Firstly, for the discs case, we managed to obtain results that confirm a possible universal behavior of crystal and disorder lattices on high dielectric contrasts. The gap-sensitivity plot provide us with rich information about the "quarter-wave stack law" and highlight the possibility of further investigations for the emergence of PBGs in dielectric-disc structures. These structures despite their simplicity (in contrast with networks complexity), can be beneficial for understanding TM-polarization gaps and how changes in the geometric structure can suppress their appearance. Moreover, all of them constitute stealthy hyperuniform patterns. The latter notion is highly associated with the appearance of complete PBGs on photonic crystals, enriching in that way previous research remarks and ringing a bell for further investigation on the future.

Moreover, the optimization of network designed lattices, proved to be challenging with the available computational resources. Therefore, we devised an efficient procedure. Within our accuracy, we did not observe convergence of the gap-sensitivity towards the theoretical QWS-curve, complete PBGs for the hexagonal and even more for the simple cubic networks require high dielectric contrasts and slender rods (even more so for the triangular networks so that we did not observe a sizable complete PBG for this symmetry). The small changes in r_{rod} that are necessary for the optimization are computationally extraordinarily expensive. We observe a "kink" in the gap sensitivity, which sheds light for further future investigations about 2D network photonic crystals. It may originate from a physical limitation, namely that TE and TM PBG overlap cannot be further optimized. Alternatively, it is possible that the complete PBG becomes exceptionally sensitive to r_{rod} so that we can no longer resolve the optimal value. Again this question can only be decided by further massive high performance computing: Is there a new law that characterizes the emergence of CPBGs on larger dielectric contrasts or is it about demanding more computational resources and employing clever optimization techniques?

Overall, the aim of this thesis is to extend our knowledge for the emergence of PBGs on 2D photonic crystals and indicate how simple optimization techniques, such as the refine grid search and the Gaussian fit on a grid of optimal values, with low computational resources, can give us important information about gap-sensitivity and push the research toward novel processes for the discovery of gaps and enrich our knowledge about the complex interplay between TM- and TE-polarization.

4 No-go theorem for hyperuniform slices

In the preceding section, we numerically investigated the physical properties of optimized two-dimensional heterogeneous materials, specifically focusing on the emergence of photonic band gaps (PBGs).

As has been established in previous literature [6, 7], hyperuniformity appears to be a necessary condition for the existence of such band gaps in these structures. Given this requirement, some natural and critical question arises regarding the physical realization of these materials: how can one systematically construct two-dimensional materials that exhibit hyperuniformity? Can mathematics provide us with a solid answer?

One intuitive route toward scalable fabrication via self-assembly [22], would be the production of multiple samples simultaneously by taking thin cross-sectional slices of existing three-dimensional materials [23]. The motivation behind this approach is the possibility of inheriting the structural properties of a bulk precursor to ensure the desired 2D characteristics.

In the following section, we examine the theoretical viability of this approach. Firstly, we offer an introductory guide in the world of hyperuniformity and random fields, providing the analytical background needed. Moreover, we provide a rigorous mathematical proof, demonstrating that this particular fabrication route is not feasible. In that way, we establish a "no-go theorem" which proves that a slice of an isotropic hyperuniform material is never hyperuniform in two dimensions. Consequently, this option is effectively ruled out as a means of constructing 2D hyperuniform structures, thereby necessitating the exploration of alternative synthesis strategies.

4.1 What is a random field?

We will start the introduction by specifying first the notion of a random field.

The theoretical framework and applications of random fields emerged from the combination of two fundamental ingredients: statistical mechanics (Boltzmann theory, Gibbs measures, etc.) and the mathematical development of probability theory (Kolmogorov [24], Markov, Stravskaya [25], and others). Owing to their widespread use in numerous scientific disciplines—including physics, mathematics, biology, and image analysis—the underlying concepts of random fields are largely shared across fields, although their terminology and representation may differ considerably. To avoid this "Babel" of disparate notations and viewpoints, we introduce the theory of random fields from a broad physical perspective while providing the necessary mathematical definitions, largely following the framework presented by Albeverio and Krohn [26].

In many physical systems, the microscopic state cannot be described deterministically. Instead, one observes spatially distributed quantities whose values fluctuate from one realization to another. Random fields provide the mathematical framework for describing such spatial randomness while preserving the underlying statistical properties of the medium. They therefore constitute a natural language for the study of heterogeneous materials, porous media, dis-

ordered solids, biological tissues, and hyperuniform structures. The long-scale phenomena originate from local interactions, which are stochastic. Lets now sum up this picture of random fields with some definitions.

Definition I (Random Fields): A random field (RF) over $\mathbb{Z}^m$ or $\mathbb{R}^m$ is a family of random variables, $\xi(x)$, parametrized by $x \in \mathbb{Z}^n$ or $x \in \mathbb{R}^n$, with values in $\mathbb{R}^m$. Thus $\xi = [\xi(\mathbf{x}) : \mathbf{x} \in \mathbb{R}^n]$, is for each $\mathbf{x}$ a measurable function from a probability space $(\Omega, \mathscr{B}, \mathbb{P})$, where $\mathscr{B}$ is the class of measurable sets in Ω and $\mathbb{P}$ is a probability measure (usually a joint or conditional probability) such that $\xi(\mathbf{x})(\omega)$ is measurable in $\mathbf{x}$ and ω with values in $\mathbb{R}^n$ (where ω are possible realizations of the random process).

Definition II (Homogeneous RF): A homogeneous random field is a random field such that for any integer k, the joint distribution of $\xi(\mathbf{x_1}), ..., \xi(\mathbf{x_k})$ is translation invariant, i.e.,

$$\mathbb{P}(\xi(\mathbf{x_1}), ..., \xi(\mathbf{x_k})) = \mathbb{P}(\xi(\mathbf{x_1} + \alpha), ..., \xi(\mathbf{x_k} + \alpha))$$

(the joint probability distribution stays invariant under a translation, $\alpha \in \mathbb{R}^n$).

Examples: The most common example is a homogeneous Gaussian random field. Its joint probability distribution is characterized by its expectation (mean) value and a correlation function, $\mathbb{E}(\xi_i(\mathbf{x})) = m_i$ and $\mathbb{E}(\xi_i(\mathbf{x})\xi_j(\mathbf{y})) = G_{ij}(\mathbf{x} - \mathbf{y})$, respectively. Where $\xi_i(\mathbf{x})$ is the ith component in $\mathbb{R}^m$ of $\xi(x)$. For the analysis, that will follow on the section: hyperuniformity in random fields, we will use $m = 1$ corresponding to scalar fields. The homogeneity implies that the mean value is constant (independent of $\mathbf{x}$) and the correlation function depends only on the difference vector $\mathbf{x} - \mathbf{y}$ between two spatial random points; if the field is isotropic, the correlation function depends only on the radial distance $r := |x - y|$. We can create also non-Gaussian random fields, by perturbing a Gaussian one. Analytically, we start with the underlying probability measure of a Gaussian field, dP_0 and we multiply it by a new exponential function, reminiscent of a Gibbs distribution (known from Statistical mechanics). The measure takes the form:

$$dP_\Lambda \propto exp\left[\lambda \int f(\xi(\mathbf{x}))d\mathbf{x}\right] dP_0, \tag{14}$$

where Λ is a bounded domain of $\mathbb{R}^n$ and $f(.)$ is any function that can be written as a Fourier transform of a complex finite measure, decreasing at infinity. We then expand in the thermodynamic limit and see if the new measure converges to a non-Gaussian one for a λ value smaller than a constant λ_0. We call such perturbations, "gentle". Moreover the non-Gaussian measure dP is strongly mixing. A property that allows us to make an analogy with a gas of particles. In the language of statistical mechanics, the above mathematical treatment is well known as fluctuations [27]. Later, we will analyze local volume fluctuations to employ the notion of hyperuniformity in two-phase media (a simple and specific category of random fields).

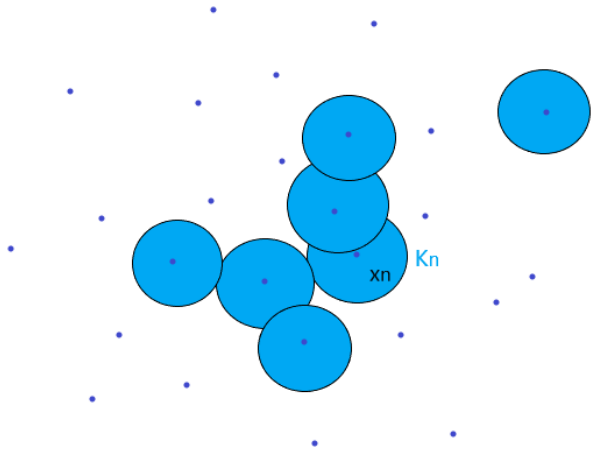


Figure 28: The Boolean Model. Where x_n is the position of a specific point in the process (here it forms a stationary Poisson process, meaning that the points are uniformly and randomly scattered in a bounded region. The K_n is a random compact set (a disc in our case, that surrounds each point). If we define the union set of these compact sets, we derive the Boolean model: $X = \bigcup_{n=1}^{\infty}(K_n + x_n)$.

Another important example are the Markov random fields, where a set of random variables obeys the **Markov property**. This means that the random field is memory-less or the joint probability obeys the following rule:

$$\mathbb{P}(\xi(\mathbf{x_k}+1) = \mathbf{x_{k+1}}|\xi(\mathbf{x_k}) = \mathbf{x_k}, ..., \xi(\mathbf{x_1}) = \mathbf{x_1}) = \mathbb{P}(\xi(\mathbf{x_{k+1}}) = \mathbf{x_k}|\xi(\mathbf{x_k}) = \mathbf{x_k}).$$

An archetypical example of a Markov random field in physics was laid out in the Ising model [28]. If the joint probability, $\mathbb{P}(\xi_1, \xi_2, ..., \xi_k)$, of a Markov field is positive, then we call it **Gibbs random field**. The interactions of the particles in this field are described by a pair potential.

A random field can also be constructed, by using as an initial step, a random point process [29]. A random closed set K naturally induces a random field $\xi(\mathbf{x}), \quad \mathbf{x} \in \mathbb{R}^n$ through its indicator function:

$$\xi(\mathbf{x}) = \mathbf{1}_K(\mathbf{x}), \qquad x \in \mathbb{R}^n \tag{15}$$

Conversely, from a random field a random closed set can be obtained as an excursion set by truncating the random field at a fixed level [30].

A particular case of a **marked point process** (which can be used to create a random field), is the **Boolean model**. More information about the Boolean model can be seen in Figure 28.

The general theory of random fields provides a natural mathematical framework for describing heterogeneous materials. However, in many physical systems, the medium consists of only two distinct phases (e.g. binary alloys, photonic crystals etc.), such as a dielectric material embedded in air or a porous

solid containing voids. In this case, the random field reduces to a binary or indicator random field, assigning the value one to points belonging to one phase and zero otherwise (exactly as in Eq. (15)). Each realization of the random field therefore corresponds to a particular realization of the microstructure. The statistical descriptors introduced for general random fields, such as ensemble averages and correlation functions, provide a geometrical description of a heterogeneous medium, including the volume fraction, two-point probability function, and covariance function. These quantities form the basis for the statistical characterization of two-phase random media and, subsequently, hyperuniform photonic materials.

4.2 What is hyperuniformity?

Many disorder systems, crystals and periodic materials, colloids jamming, perfect glasses and more, are obtaining hyperuniformity (or super-homogeneity). This exotic state of matter is characterized by long-wavelength suppression of density fluctuations. Specifically, for some isotropic disordered materials, hyperuniformity implies a form of "hidden order". Hyperuniform materials can be isotropic like a liquid and homogeneous like a crystal [31].

Defining a test window for a random sample of a material (or a random point process, for a more mathematical description), we can compute the volume variance ($\sigma_V(\mathbf{R})$), and extract information about the three most important classes of hyperuniformity (I, II and III). By observing the scaling behavior of the volume variance, we can categorize different materials on each of these classes.

An important property for the characterization of a system or a random point process as hyperuniform, is the structure factor, $S(\mathbf{k})$, scaling behavior with the wave number (or the wavelength) on a large scale. For hyperuniform systems, the structure factor tends to zero for small wavenumbers ($S(\mathbf{k}) \to 0$, in the limit $|\mathbf{k}| \to 0$).

Hyperuniformity can also be defined thermodynamically, as an inverse critical point. The Ornstein-Zernike theory [32], used for the description of critical opalescence has provided an equation that connects the total correlation function of a point process with the direct correlation function, $h(\mathbf{r})$ and $c(\mathbf{r})$, respectively. By usage of this equation, we can compute around the vicinity of a hyperuniform state, the different critical exponents for the correlation length, the direct correlation function and the structure factor. In this text, we will not mention more about the thermodynamical description. Our attention will be focused on the mathematical description of hyperuniformity, especially for random fields and two-phase media. This mathematical frame will provide the first pieces of the puzzle that we will built together with stereology.

4.2.1 Hyperuniformity in random fields

Heterogeneous media (therefore two phase media) can be seen as a special case of random fields. Thus, we can start exploring hyperuniformity in the language

of random fields, construct an elegant mathematical formalism and then via coarse graining we can present (in the next section) a "reduced" mathematical model for two phase media.

Random Fields can be scalar or vector like. In this manuscript we will focus our attention on the description of random scalar fields (e.g. temperature, convection and concentration fields). Other examples are pattern formations in biological and chemical systems described by famous equations such as: Cahn-Hilliard equation for spinodal-decomposition and Swift-Hohenberg equation used in hydrodynamics [33].

For the mathematical formalism, consider a scalar random field $F(\mathbf{x})$ in $\mathbb{R}^d$, that is real valued and its autocovariance function is given by:

$$\psi(\mathbf{r}) = \left\langle (F(\mathbf{x_1}) - \langle F(\mathbf{x_1})\rangle)(F(\mathbf{x_2}) - \langle F(\mathbf{x_2})\rangle) \right\rangle, \tag{16}$$

where we have taken into account the statistical homogeneity of the field, since $\mathbf{r} = \mathbf{x_2} - \mathbf{x_1}$, which is a d-dimensional vector (homogeneity has already been mentioned in the introduction to random fields). Next, we assume that the Fourier transform of the autocovariance exists (the spectral density). A random scalar field is hyperuniform if the spectral density tends to zero for small wavenumbers:

$$\lim_{|\mathbf{k}|\to\mathbf{0}} \tilde{\psi}(\mathbf{k}) = 0, \tag{17}$$

which implies, ψ obeys the sum rule (the integral of the autocovariance is zero).

As we have already discussed, random fields can fluctuate. So the integrated fields ψ inside a spherical window, of radius R, will fluctuate as the window position varies. To measure these fluctuations, we employ the local variance described below (in the Fourier space):

$$\sigma_F^2(\mathbf{R}) = \frac{1}{u_1(\mathbf{R})(2\pi)^d} \int_{\mathbb{R}^d} \tilde{\psi}(\mathbf{k})\tilde{\alpha_2}(\mathbf{k};\mathbf{R})d\mathbf{k}. \tag{18}$$

Torquato and Ma [33], have used Gaussian fields, that describe a variety of physical phenomena, and specifically many heterogeneous materials. They tested them numerically and have discovered, that the time evolution of spinodal decomposition models (such us the Cahn-Hilliard equation) can be modeled as a hyperuniform system in the scaling regime, where the local variance was shown to decay like $1/R^3$ for a square test window of side length, R. Moreover, they demonstrated that level-cutting a hyperuniform Gaussian random field produces a two-phase medium that does not inherit the hyperuniformity of the original field. The conjecture is related to the stereological assumption that will be presented in the next paragraph for two random fields.

Although Gaussian random fields fail to reproduce hyperuniform two-phase media through the coarse-graining (level-cutting) procedure, Torquato proposed a method for constructing hyperuniform heterogeneous media by level-cutting non-Gaussian random fields [34]. His approach is conceptually similar to that discussed by Alberio and Krohn in the previous section, where a Gaussian random field is multiplied by another random field to generate a new, non-Gaussian

field. Similarly, Torquato constructs a non-Gaussian random field by convolving a hyperuniform point configuration with a nonnegative, dimensionless scalar kernel, $K(\mathbf{x};\mathbf{C})$, that is radially symmetric and sufficiently localized, so that its Fourier transform is well defined. Here, $\mathbf{C}$, represents a set of parameters that characterize the shape of the radial function.

4.2.2 Hyperuniformity in two phase media

In this section we will develop the equation of the volume-fraction variance, and its asymptotic behavior for local fluctuations for a single configuration (which describes spatial fluctuations for a density of points/particles) for two-phase media, which is a subcategory of random fields. Hyperuniformity can be defined on random heterogeneous media with two phases (two disjoint regions): phase 1, $\mathscr{V}_1(\omega)$ with volume fraction ϕ_1 and a phase 2, $\mathscr{V}_2(\omega)$, with volume fraction ϕ_2. The statistical properties of each phase are characterized by an n-point probability function $S_n^{(i)}$, where i, indicates the ith-phase of the medium. For $n = 1$, $S_1^{(i)}$ represents the one-point probability function. If the later function is independent of the position (translational invariant), then $S_1^{(i)}$ is equal to the volume fraction of phase i: ϕ_i [35].

Although the global volume fraction is invariant (stays constant) on a homogeneous medium, on a spatially local scale it can still fluctuate. These fluctuations, for an observation window that we define $\Omega \subset \mathscr{V}$ (where $\mathscr{V}$ is the whole space/medium: $\mathscr{V} = \mathscr{V}_1 \cup \mathscr{V}_2$), can be described by the local volume fraction, $\tau(x)$, which has already been computed by Lu and Torquato [36]. Here we will review [36] and present the asymptotic variance formula for two phase media. The following equation (asymptotic variance), is important for the characterization of materials as hyposurficial, indicating the stereological features that we will ascribe to it.

The local volume fraction, $\tau_i(\mathbf{x}_0; R)$, of phase i, within a window of radius R, centered at position x_0 is given by:

$$\tau_i(\mathbf{x}_0;\mathbf{R}) = \frac{1}{u_1(\mathbf{R})}\int \mathscr{I}^{(i)}(\mathbf{x}) w(\mathbf{x}-\mathbf{x}_0;\mathbf{R})d\mathbf{x}, \tag{19}$$

where $u_1(R)$ is the window volume, $\mathscr{I}^{(i)}$ is the characteristic function (or indicator function) for phase i (defined in [36]) and w is the window function equal to one for values inside the window ($\mathbf{x} - \mathbf{x_0} \in \Omega$) or zero otherwise. The local volume fraction for large window sizes, $R \to \infty$, becomes equal with the volume fraction of phase i, ϕ_i: $\tau_i(\mathbf{x}_0;\mathbf{R}) \to \langle I\rangle = \phi_i$. The variance associated with the local volume fraction is then defined via the following equation:

$$\sigma_V^2 = \langle \tau^2\rangle - \langle\tau\rangle^2 = \langle \tau_i^2(\mathbf{x}_0; R)\rangle - \phi_i^2 \tag{20}$$

Following reference [35], the volume variance can be expressed in terms of

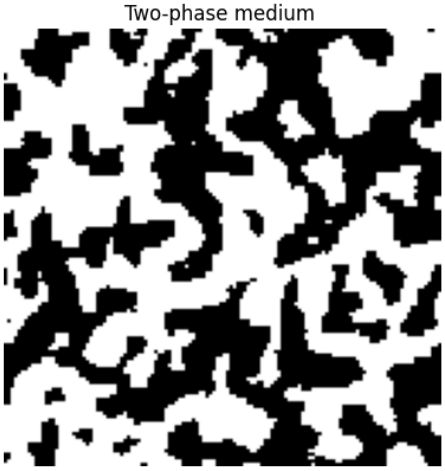


Figure 29: An example of a two-phase medium, rigorously used in the physics and statistical mechanics community is the Ising model (more specifically we have a random field here). These two-phase media can be reproduced with well-known algorithms such as the Metropolis-Hastings [37].

the autocovariance function $\chi_V(r)$

$$\sigma_V^2(R) = \frac{1}{u_1(R)} \int_{\mathbb{R}^d} \chi_V(\mathbf{r}) \alpha_2(\mathbf{r}; R)\, d\mathbf{r} \tag{21}$$

where $\alpha_2(\mathbf{r}; R)$, is the scaled intersection volume [31] (the ratio of the intersection volume of two windows over the total volume of the test window, $u_1(R)$). We can map Eq. 21 to Fourier space, by applying Parseval's theorem ($r \to k$ and we get an extra normalization term $1/(2\pi)^d$):

$$\sigma_V^2(R) = \frac{1}{u_1(R)(2\pi)^d} \int_{\mathbb{R}^d} \tilde{\chi}_V(\mathbf{k}) \tilde{\alpha}_2(\mathbf{k}; R) d\mathbf{k} \tag{22}$$

Torquato and Stillinger [38], have developed through sphere packing research, an equation for the scaled intersection volume $a_2(R)$, through series expansion, for odd dimensions, for $r \leq 2R$ (a more compact form is observed in [35]):

$$a_2(r; R) = 1 - c(d)x + c(d) \sum_{n=2}^{\infty} (-1)^n \frac{(d-1)(d-3)\cdots(d-2n+3)}{(2n-1)[2 \cdot 4 \cdot 6 \cdots (2n-2)]} x^{2n-1}, \tag{23}$$

where $x = r/2R$ and $c(d)$ is a d-dimensional constant associated with gamma functions depended on the dimension d of the process [35]. Plugging Eq. (23) into the local volume fraction variance, we can reach (approximately) the asymptotic variance relation for two phase media, as exactly mentioned in [35]:

$$\sigma_V^2(R) = \frac{1}{u_1(R)} \int \chi_V(\mathbf{r})[1 - c(d)\frac{\mathbf{r}}{2R} + ...]d\mathbf{r} \tag{24}$$

Splitting Eq. (24) (the integral of the autocovariance function) into two parts, we derive two terms (two dimensionless coefficients) according to Torquato [35]:

The Volume coefficient, A_V:

$$A_V(R) = \int_{r \leq 2R} \chi_V(\mathbf{r})d\mathbf{r} \tag{25}$$

and the surface coefficient, B_V:

$$B_V(R) = \frac{-c_1(d)}{2} \int_{r \leq 2R} \chi_V(r)\mathbf{r}d\mathbf{r} \tag{26}$$

Combining Eq. (24) – (26) and recalling that $u_1(R) \approx R^d$, we derive the asymptotic variance:

$$\sigma_V^2(R) = \frac{1}{R^d}[A_V + \frac{B_V}{R} + o(R^{-(d+1)})] \tag{27}$$

By applying a rescale to the system, $R \to R/D$, where D is a characteristic microscopic length scale of the system (e.g. the mean nearest neighbor distance between two particles). We receive the exact equation [35]:

$$\sigma_V^2(R) = [A_V(R)(\frac{D}{R})^d + B_V(R)(\frac{D}{R})^{d+1} + o(\frac{D}{R})^{(d+1)}] \tag{28}$$

According to [35], a hyperuniform two phase medium is one in which:

$$\lim_{\mathbf{k} \to 0} \tilde{\chi}_V(\mathbf{k}) = 0 \tag{29}$$

So, from Eq. (28) and with the use of a Fourier transform, we can deduce that hyperuniform systems are those whose volume coefficient vanishes ($A_V = 0$). When B_V=0 (the surface-area coefficient vanishes), then the point process or

the system that we examine (materials, porous media, etc.) is stated as a "hyposurficial" system. A_V and B_V cannot be both zero [31].

For power-law spectral densities $\tilde{\chi}_V(k) \to \mathbf{k}^a$, $|\mathbf{k}| \to 0$, and $a > 0$, we can obtain three different classes of hyperuniformity [35]:

$$\sigma_V^2(R) \sim \begin{cases} R^{-(d+1)}, & a > 1 \quad \text{(Class I)}, \\ R^{-(d+1)} \ln R, & a = 1 \quad \text{(Class II)}, \\ R^{-(d+a)}, & 0 < a < 1 \quad \text{(Class III)}, \end{cases} \qquad (R \to \infty). \tag{30}$$

For $a > 1$, the fluctuations scale like the surface area of the window. The exponent a is a measure of how strongly fluctuations are suppressed in the system already at finite wavelengths. As a increases, the suppression increases already at shorter wavelength. In the limit of $a \to \infty$, we "find" the regime of "stealthy" hyperuniformity, which means there is no scattering in an exclusion region around the origin in $\mathbf{k}$-space, i.e., $S(\mathbf{k}) = 0$ for $0 \leq |\mathbf{k}| \leq K$.

4.3 Stereology for hyperuniform random fields

Stereology is the science of inferring information for a d-dimensional object (e.g. three dimensional object), through an observation of $(d-1)$-dimensional samples of the same object (e.g. two dimensional cross sections). We have two types of stereology: (1) the target is an inhomogeneous deterministic "body" (a tissue, an organ etc.) and the planar sections (the samples that we need to take in order to perform our statistical methods) are random (random samplings), this is the so called design approach. Whereas, (2) if the target is random. Often its is assumed that it is a sample of homogeneous and isotropic random process. Then the geometrical probes (samples/sections) or windows, are deterministic and closed. This is called the model approach and is very common on material science. Both of these two approaches are important for what will follow on the next paragraph, but we will focus on the model approach, since our application is a two-phase homogeneous and isotropic medium, which can be derived, as known from boolean or germ-grain models of random processes. Stereology is the "poor mans" tomography (as has been stated by Torquato) and the mapping of the initial space/structure (e.g. (X, T)) to the cross-section $(X \cap T)$ causes a loss of information about our random field X. So, the key issue of stereology, is to understand what kind of information is lost or if this is inherited by the new geometrical structure that has to be studied, $X \cap T$ [39].

4.3.1 Stereological expansion to random fields

Let us now expand the stereology assumption in the language of random fields (a generalization of the two phase media, since many of them are constructed from random fields). The underlying idea is the following:

Let d be the dimension of the space in which we are given a random field $F \geq 0$, and let $q \in \{1, ..., d-1\}$ be the number of dimensions to which we reduce. So, the new random field G is the original random field restricted to a q-dimensional subspace S_q. Since we assume that F is isotropic, we can also assume that $S_q = \mathbb{R}^q \times \{0\}^{d-q}$ without loss of generality. Let g be some real-valued, bounded function in $\mathbb{R}^q$ with bounded support (a test function). Then

$$\int_{\mathbb{R}^q} g(\mathbf{x})G(\mathbf{x})d\mathbf{x} = \int_{\mathbb{R}^d} f(\mathbf{x})F(\mathbf{x})d\mathbf{x}, \tag{31}$$

with $f := g \times \delta_0^{d-q}$. Here we already use physics notation for the delta function. Then we obtain:

$$\begin{aligned}(2\pi)^{2q} \int |\hat{g}(\mathbf{k})|^2 S_G(\mathbf{k})\, d\mathbf{k} &= \mathbb{V}ar\left[\int g(\mathbf{x})G(\mathbf{x})\, d\mathbf{x}\right] \\ &= \mathbb{V}ar\left[\int f(\mathbf{x})F(\mathbf{x})\, d\mathbf{x}\right] = (2\pi)^{2d} \int |\hat{f}(\mathbf{k})|^2 S_F(\mathbf{k})\, d\mathbf{k},\end{aligned} \tag{32}$$

where S_G is the spectral density of G, and S_F that of F. Note that $\hat{f}(\mathbf{k}) = (2\pi)^{-(d-q)}\hat{g}(k_1, ..., k_q)$. Hence, $S_G(k_1, ..., k_q) = \int S_F(k_1, ..., k_d)d(k_{q+1}, ..., k_d)$. By isotropy of F, S_F is also isotropic and a quick calculation shows that $S_G(0)$ can only be 0 if S_F is constant 0, whereby the random field F must have been deterministic. So every non-trivial F yields a non-hyperuniform G.

However, this also works when there is no spectral density, but only a spectral measure[1]. And while isotropy is an important assumption since there are non-isotropic counterexamples, it is a lot stronger than what is actually sufficient. It would suffice that there is a k in every direction such that $S_F(k) > 0$, i.e., for every s with $\|s\| = 1$, there is an $r > 0$ such that $S_F(rs) > 0$.
From the following we can conceive the following theorem:

Theorem 4.1 (No-go theorem for hyperuniformity under dimensional reduction)**.** *Let $F \geq 0$, be a statistically homogeneous and ergodic random field on $\mathbb{R}^d$ satisfying:*

1. *F possesses a spectral density S_F;*
2. *S_F is a continuous function.*
3. *For every unit vector $\mathbf{s} \in \mathbb{S}^{d-1}$, there exists $r \geq 0$ such that*

$$S_F(r\mathbf{s}) > 0.$$

[1]Periodic crystals, fields that are described by a sine/cosine function, and many stationary processes, do not acquire a spectral density. Although according to Bochner's theorem ("Harmonic analysis and the theory of Probability", 1955 [40]), for every stationary random field, F, there is always a positive finite measure that exists, μ. In our case, for statistically homogeneous disordered media, autocovariance functions are typically integrable, so we can use the spectral density.

Let G be the restriction of F to a q-dimensional subspace of $\mathbb{R}^d$, with $1 \leq q < d$. Then G is not hyperuniform. In particular,

$$S_G(\mathbf{0}) > 0. \tag{33}$$

Hence, hyperuniformity is not inherited under dimensional reduction:

$$F \text{ hyperuniform } \not\Rightarrow \ G \text{ hyperuniform.}$$

In particular, hyperuniformity is not inherited under dimensional reductions. The hyperuniform field F does not imply a hyperuniform field G. For isotropic fields this conclusion remains valid, even for a stealthy hyperuniform field F.

Proof. The proof mainly relies on establishing Eq. (32), which provides the central result required for the theorem.

Let us rename the left hand side of Eq. (31) with a letter A: $A = \int g(\mathbf{x})G(\mathbf{x})d\mathbf{x}$ and the right hand side of it, with a letter B: $B = \int f(\mathbf{x})F(\mathbf{x})d\mathbf{x}$. As we can obtain from Eq. (31), the random variables A and B are identical. So their variances, will also be the same:

$$\mathbb{V}ar\left[\int g(\mathbf{x})G(\mathbf{x})\,d\mathbf{x}\right] = \mathbb{V}ar\left[\int f(\mathbf{x})F(\mathbf{x})\,d\mathbf{x}\right] \tag{34}$$

How do we now prove that,

$$\mathbb{V}ar\left[\int g(\mathbf{x})G(\mathbf{x})\,d\mathbf{x}\right] = (2\pi)^{2q}\int |\hat{g}(\mathbf{k})|^2 S_G(\mathbf{k})\,d\mathbf{k}.$$

If G is a stationary random field, we can define:

$$\langle G(\mathbf{x})\rangle = \mu,$$

then we need to compute the variance, as it is defined in Eq. (34). So we need to compute the variance of A. Thus, we need to compute:

$$\mathbb{V}ar[A] = \langle A^2\rangle - \langle A\rangle^2 \tag{35}$$

So, $\langle A\rangle = \langle \int g(\mathbf{x})G(\mathbf{x})\,d\mathbf{x}\rangle = \int g(\mathbf{x})\langle G(\mathbf{x})\rangle\,d\mathbf{x} = \mu\int g(\mathbf{x})d\mathbf{x}$.
Hence,

$$\langle A\rangle^2 = \mu^2(\int g(\mathbf{x})\,d\mathbf{x})^2 \tag{36}$$

Now for the second moment of A^2, we have:

$$\langle A^2\rangle = \Big\langle \Big(\int g(\mathbf{x})G(\mathbf{x})\,d\mathbf{x}\Big)^2\Big\rangle = \Big\langle \Big(\int g(\mathbf{x})G(\mathbf{x})\,d\mathbf{x}\Big)\Big(\int g(\mathbf{x}')G(\mathbf{x}')\,d\mathbf{x}'\Big)\Big\rangle.$$

Therefore,

$$\langle A^2\rangle = \int\int g(\mathbf{x})g(\mathbf{x}')\langle G(\mathbf{x})G(\mathbf{x}')\rangle\,d\mathbf{x}\,d\mathbf{x}'. \tag{37}$$

Now we use the following identity for the covariance:

$$C(\mathbf{x}-\mathbf{x}') = \langle G(\mathbf{x})G(\mathbf{x}')\rangle - \mu^2, \tag{38}$$

where $C(\mathbf{x}-\mathbf{x}') = \mathbb{C}ov(G(\mathbf{x}), G(\mathbf{x}'))$ is the covariance function of two points $\mathbf{x}$ and $\mathbf{x}'$. We substitute Eq. (38) into Eq. (37) and we obtain:

$$\begin{gathered}\langle A^2\rangle = \int\int g(\mathbf{x})g(\mathbf{x}')[C(\mathbf{x}-\mathbf{x}')+\mu^2]\,d\mathbf{x}d\mathbf{x}' = \\ \int\int g(\mathbf{x})g(\mathbf{x}')C(\mathbf{x}-\mathbf{x}')\,d\mathbf{x}d\mathbf{x}' + \mu^2\int\int g(\mathbf{x})g(\mathbf{x}')\,d\mathbf{x}d\mathbf{x}'\end{gathered} \tag{39}$$

Subtract now Eq. (36) from Eq. (39) so that the terms with μ^2 cancel; thus we derive the variance:

$$\mathbb{V}ar[A] = \int\int g(\mathbf{x})g(\mathbf{x}')C(\mathbf{x}-\mathbf{x}')\,d\mathbf{x}d\mathbf{x}'. \tag{40}$$

Next step is to introduce the inverse Fourier transform of the covariance, which is the integral over Fourier space, of the spectral density:

$$C(\mathbf{r}) = \int S_G(\mathbf{k})e^{i\mathbf{k}\cdot\mathbf{r}}d\mathbf{k}, \tag{41}$$

where $S_G(\mathbf{k})$ is the spectral density, defined by the Wiener-Khinchin theorem [41], as the inverse Fourier transform of $C(\mathbf{r})$ and $\mathbf{r} = \mathbf{x}-\mathbf{x}'$. We plug Eq. (41) in Eq. (40) and we obtain:

$$\begin{gathered}\mathbb{V}ar[A] = \int\int\int g(\mathbf{x})g(\mathbf{x}')S_G(\mathbf{k})e^{i\mathbf{k}\cdot(\mathbf{x}-\mathbf{x}')}\,d\mathbf{k}d\mathbf{x}d\mathbf{x}' = \\ \int S_G(\mathbf{k})\Big(\int g(\mathbf{x})e^{i\mathbf{k}\cdot\mathbf{x}}d\mathbf{x}\Big)\Big(\int g(\mathbf{x}')e^{-i\mathbf{k}\cdot\mathbf{x}}d\mathbf{x}'\Big)d\mathbf{k} = \\ (2\pi)^{2q}\int S_G(\mathbf{k})(\hat{g}(\mathbf{k})(\hat{g}(-\mathbf{k}))d\mathbf{k} = (2\pi)^{2q}\int|\hat{g}(\mathbf{k})|^2S_G(\mathbf{k})d\mathbf{k},\end{gathered} \tag{42}$$

where in the final step, we recognized the Fourier transform $g(\mathbf{x})$: $\hat{g}(\mathbf{k}) = \frac{1}{(2\pi)^q}\int g(\mathbf{x})e^{-ikx}dx$ and its conjugate, $\hat{g}(-\mathbf{k})$. We know that the product of $\hat{g}\hat{g*}$, gives the quadratic component of g included in the integral of Eq. (42). An analogous calculation applies to the test function f and the random field F, in d dimensions. Combining the two variance representations and using $f = g\times\delta_0^{d-q}$ yields the spectral-density relation

$$S_G(\mathbf{k}_\parallel) = \int_{\mathbb{R}^{d-q}} S_F(\mathbf{k}_\parallel, \mathbf{k}_\perp)\,d\mathbf{k}_\perp,$$

under the assumptions required for this restriction formula. In particular, setting $\mathbf{k}_\parallel = \mathbf{0}$ gives

$$S_G(\mathbf{0}) = \int_{\mathbb{R}^{d-q}} S_F(\mathbf{0}, \mathbf{k}_\perp)\,d\mathbf{k}_\perp. \tag{43}$$

The directional positivity assumption ensures that S_F is strictly positive at some point in the perpendicular subspace. By continuity, it remains positive in a neighborhood of that point. Since a spectral density is nonnegative, the integral is strictly positive, and hence $S_G(\mathbf{0}) > 0$. Therefore, G is not hyperuniform $\square$

5 Conclusions and outlook

In this thesis, we initially provided the theoretical and computational background of photonic crystals. We defined our mainly objective, namely, the study of gap sensitivity on two-dimensional (2D) PhCs, and discussed the importance of stealthy hyperuniformity for the design of photonic heterostructures with isotropic photonic band gaps (PBGs). Special emphasis is placed on PBGs in systems composed of discs and network structures. Moreover, the role of transverse electric (TE) and transverse magnetic (TM) modes is discussed, together with examples of 2D photonic crystal structures. We then describe our methodological steps followed in our preliminary analysis, for the detection of PBGs. We computed via Python codes, the gap-to-midgap ratios for disc-based and networks with different lattice geometries. Also, we constructed gap plots as functions of the radii and generated heatmaps for the respective structures. In addition, we defined and explained the notion of complete photonic band gaps (CPBGs), why they here appear only on network structures and how we can create heatmaps to identify possible gap regions and estimate their corresponding optimal radii for three characteristic crystal lattices: simple cubic, triangular and hexagonal. Furthermore, we used our initial estimates of the gap-to-midgap ratios, to optimize 2D crystal structures made of dielectric discs, including disorder structures generated from stealthy hyperuniform point patterns. We employed a refined grid search method (for optimization), and the resulting gap and gap-sensitivity plot, indicated a universal behavior across all the investigated lattice geometries, in agreement with the quarter-wave stack theoretical curve, S_{QWS}. However, this behavior is associated with a small, apparently universal deviation from the theoretical curve that persists even for high dielectric contrasts. This discrepancy may be attributable to the low resolution and numerical tolerance of MPB, as well as limitations of the optimization procedure (optimization tolerance). Alternatively, it may reflect a physical phenomenon that requires to invest more time and computational resources in the future to investigate.

Additionally, we have conducted research on the optimization of 2D network structures, using a similar refined grid search, complemented by a Gaussian fitting, to reduce the influence of fluctuations in the numerical data. However, our optimization analysis did not yield a sufficiently extensive set of reliable data for all the investigated lattice geometries. While we obtained numerous data points for the hexagonal lattice, only a few reliable points were available for the simple cubic lattice. Despite these limitations, the results revealed an interesting feature in the gap-sensitivity plot: a "kink" in the data was appearing for $\alpha = 12.6$. This observation, may be associated with the decreasing changes in the optimal wall thickness of the network rods as the dielectric contrast increases. Two explanations are still possible: (1) it may be a numerical artifact of our optimization procedure towards the end of our range of α if the competing overlap of TE and TM gaps becomes exceptionally sensitive to the slender rods; or (2) the overlap of TE and TM gaps is limited for high dielectric contrasts causing a real deviation from the universal gap sensitivity.

Last but not least, we extend our mathematical background of hyperuniformity on the context of random fields and stereology, laying the groundwork for the proof of a "no-go theorem". Under the assumptions specified in the theorem, this result demonstrates that constructing 2D hyperuniform materials from slices of 3D isotropic materials is impossible, thereby challenging the hypothesis that hyperuniformity can be preserved through simple dimensional reduction by slicing ("slicing hypothesis").

Overall, this thesis, provides analytical tools, by "borrowing" mathematical knowledge from statistical mechanics and stereology to construct an elegant theorem that rules out the possibility of designing 2D hyperuniform materials by slicing 3D materials, so that they have to be designed using bottom-up and self assembly approaches. At the same time, our numerical results demonstrate how relatively simple optimization techniques and numerical evaluations, even with limited computational resources, can reveal important trends, fundamental principles, and limitations in the design of two-dimensional photonic crystals, arising from both computational constraints and geometrical restrictions. These findings highlight the central role of geometry in determining the formation and properties of photonic crystals, both in analytical investigation and in numerical optimization.

References

[1] Luca Peliti. *Statistical Mechanics in a Nutshell*. Princeton University Press, 2011.

[2] John D. Joannopoulos, Steven G. Johnson, Joshua N. Winn, and Robert D. Meade. *Photonic Crystals: Molding the Flow of Light*. Princeton University Press, 2nd edition, 2008.

[3] Sajeev John. Strong localization of photons in certain disordered dielectric superlattices. *Physical Review Letters*, 58:2486, 1987.

[4] Lasha Tkeshelashvili, Jens Niegemann, Suresh Pereirae, and Kurt Busch. Nonlinear wave interaction in photonic band gap materials. *Photonics and Nanostructures: Fundamentals and Applications*, 4:75, 2006.

[5] Salvatore Torquato, Ge Zhang, and Frank H. Stillinger. Ensemble theory for stealthy hyperuniform disordered ground states. *Physical Review X*, 5:021020, 2020.

[6] Marian Florescu, Salvatore Torquato, and Paul J. Steinhardt. Designer disordered materials with large, complete photonic band gaps. *Proceedings of the National Academy of Sciences*, 106:20658, 2009.

[7] Michael A. Klatt, Paul J. Steinhardt, and Salvatore Torquato. Wave propagation and band tails of two-dimensional disordered systems in the thermodynamic limit. *Proceedings of the National Academy of Sciences*, 119:e2213633119, 2022.

[8] Michael A. Klatt, Paul J. Steinhardt, and Salvatore Torquato. Gap sensitivity reveals universal behaviors in optimized photonic crystal and disordered networks. *Physical Review Letters*, 127:037401, 2021.

[9] Charles Kittel. *Introduction to Solid State Physics*. Wiley, 8th edition, 2005.

[10] Eli Yablonovitch. Photonic band-gap crystals. *Journal of Physics: Condensed Matter*, 5:2443, 1993.

[11] Eli Yablonovitch. Inhibited spontaneous emission in solid-state physics and electronics. *Physical Review Letters*, 58:2059, 1987.

[12] Christoph Fenzl, Thomas Hirsch, and Otto S. Wolfbeis. Photonic crystals for chemical sensing and biosensing. *Angewandte Chemie International Edition*, 53:3318, 2014.

[13] John D. Jackson. *Classical Electrodynamics*. Wiley, 3rd edition, 1998.

[14] Jun J. Sakurai. *Modern Quantum Mechanics, Revised ed.* Addison-Wesley Publ. Company, 1993.

[15] Steven G. Johnson and J. D. Joannopoulos. Block-iterative frequency-domain methods for maxwell's equations in a planewave basis. *Optics Express*, 8:173, 2001.

[16] Eli Yablonovitch. Photonic crystals: semiconductors of light. *Scientific American*, 285:46, 2001.

[17] Mikael C. Rechtsman, Hyeong-Chai Jeong, Paul M. Chaikin, Salvatore Torquato, and Paul Steinhardt. Optimized structures for photonic quasicrystals. *Physical Review Letters*, 101:073902, 2008.

[18] Keiichi Edagawa. Photonic crystals, amorphous materials, and quasicrystals. *IOP Publishing, Science and Technology of Advanced Materials*, 15:034805, 2014.

[19] Salvatore Torquato. Physics of sphere packings. *Nature Reviews Physics*, 8:261, 19 March 2026.

[20] Jan Verwaeren, Pieter Van der Weeën, and Bernard De Baets. A search grid for parameter optimization as a byproduct of model sensitivity analysis. *Applied Mathematics and Computation*, 261:8, 2015.

[21] Kendall Atkinson. *An Introduction to Numerical Analysis, 2nd Edition.* Wiley and Sons, 1991.

[22] Junhu Zhang, Zhiqiang Sun, and Bai Yang. Self-assembly of photonic crystals from polymer colloids. *Current Opinion in Colloid & Interface Science*, 14:103, 2009.

[23] Luiz Manuel Cruz-Orive. *Stereology: Theory and applications, Interdisciplinary Applied Mathematics*, volume 59. Springer, 2024.

[24] Andrey N.Kolmogorov. *Foundation of the theory of probability.* Chelsea Publishing Company, New York, 1950.

[25] Enrique Hernández-Lemus. Random fields in physics, biology and data science. *Frontiers in Physics*, 9:641859, 2021.

[26] Sergio Albeverio and Raphael Hoegh Krohn. Homogeneous random fields and statistical mechanics. *Journal of Functional Analysis*, 19:242, 1975.

[27] Landau and Lifshitz. *Statistical Physics, 3rd Edition, Part 1.* Elsevier, Butterworth-Heinemann, 1980.

[28] Ernst Ising. Beitrag zur Theorie des Ferromagnetismus. *Zeitschrift für Physik*, 31:253, 1925.

[29] Dietrich Stoyan. Stereology and stochastic geometry. *International Statistical Review*, 58:227, 1990.

[30] Sung N. Chiu, Dietrich Stoyan, Wilfrid S. Kendall, and Joseph Mecke. *Stochastic Geometry and its Applications*. J. Wiley and Sons, Ltd, 2013.

[31] Salvatore Torquato and Frank H. Stillinger. Local density fluctuations, hyperuniformity and order metrics. *Physical Review E*, 68:041113, 2003.

[32] Steven A. Kivelson, Jack Mingde Jiang, and Jeffrey Chang. *Statistical Mechanics of Phases and Phase Transitions*. Princeton University Press, 2024.

[33] Zheng Ma and Salvatore Torquato. Random scalar fields and hyperuniformity. *Journal of Applied Physics*, 121:244904, 2017.

[34] Salvatore Torquato. Hyperuniformity and its generalizations. *Physical Review E*, 94:022122, Aug 2016.

[35] Salvatore Torquato. Hyperuniform states of matter. *Physics Reports*, 745:1, 2018.

[36] Binglin Lu and Salvatore Torquato. Local volume fraction fluctuations in heterogeneous media. *Journal of Chemical Physics*, 93:3452, 1990.

[37] David Chandler. *Introduction to Modern Statistical Mechanics*. Oxford University Press, New York, 1987.

[38] Salvatore Torquato and Frank H. Stillinger. New conjectural lower bounds on the optimal density of sphere packings. *Experimental Mathematics*, 15:307, 2006.

[39] Edited by Wilfrid S. Kendall and Ilya Molchanov (multiple authors). *New Perspectives in Stochastic Geometry*. Oxford University Press, 2010.

[40] Salomon Bochner. *Harmonic Analysis and the Theory of Probability*. University of California Press, Berkeley, 1955.

[41] Joseph W. Goodman. *Statistical Optics*. John Wiley & Sons, Hoboken, New Jersey, 2 edition, 2015.

A Appendix: Heatmaps for TE/TM polarization

The following section includes all the heatmaps of the gap-to midgap ratio, constructed for network structures for the sc, triangular and hexagonal lattice geometry.

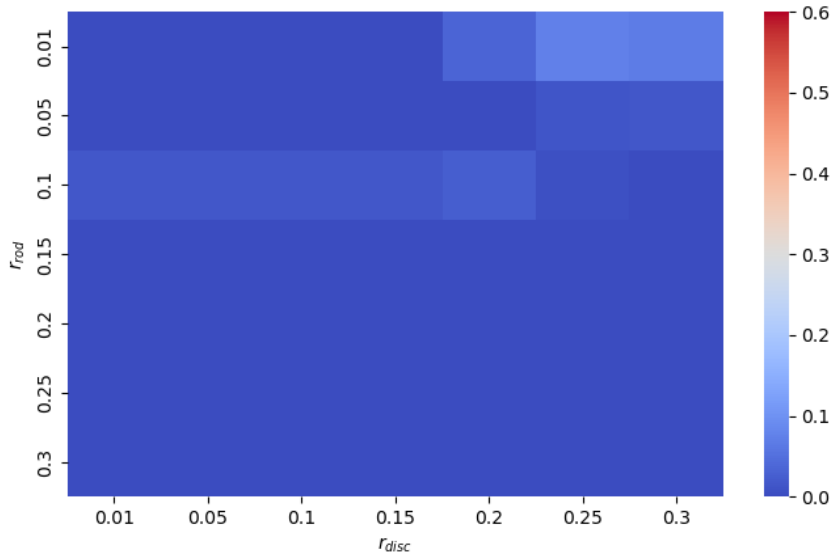


Figure 30: Heatmap of the gap-to-midgap ratio for the simple-cubic lattice in TM polarization at dielectric contrast $\alpha = 4.0$.

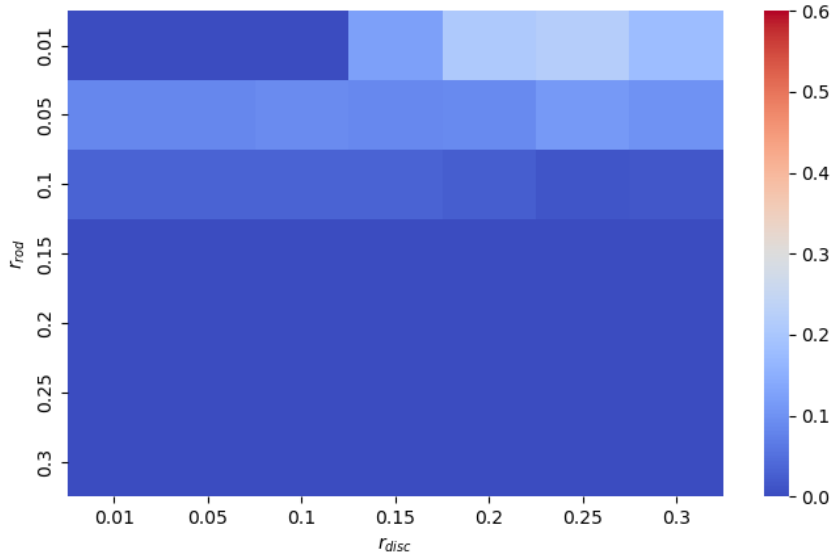


Figure 31: Heatmap of the gap-to-midgap ratio for the simple-cubic lattice in TM polarization at dielectric contrast $\alpha = 7.0$.

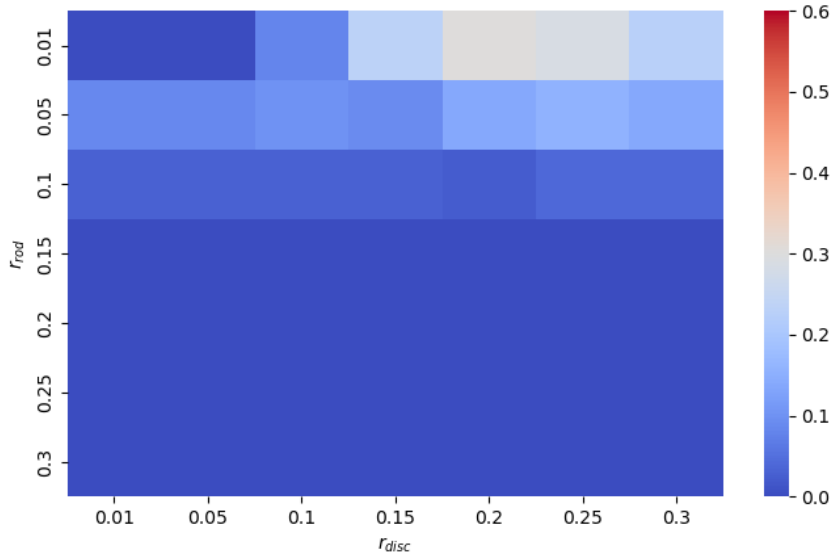


Figure 32: Heatmap of the gap-to-midgap ratio for the simple-cubic lattice in TM polarization at dielectric contrast $\alpha = 10.0$.

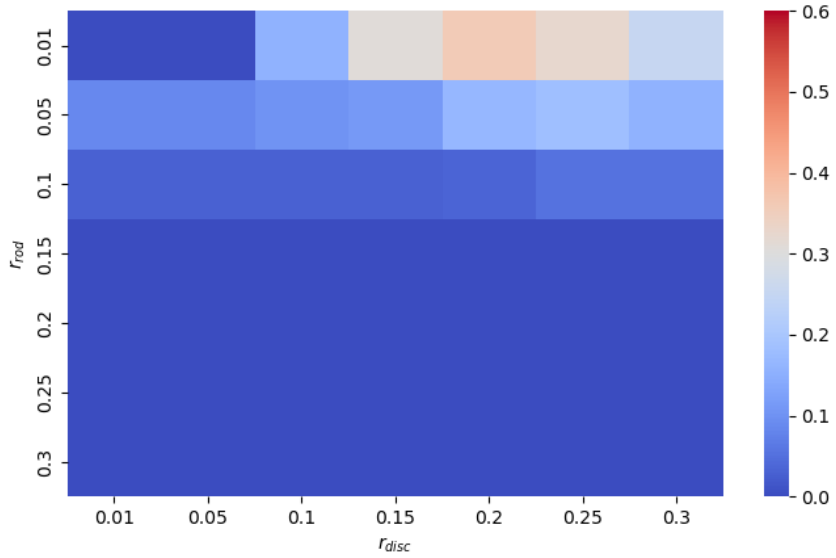


Figure 33: Heatmap of the gap-to-midgap ratio for the simple-cubic lattice in TM polarization at dielectric contrast $\alpha = 13.0$.

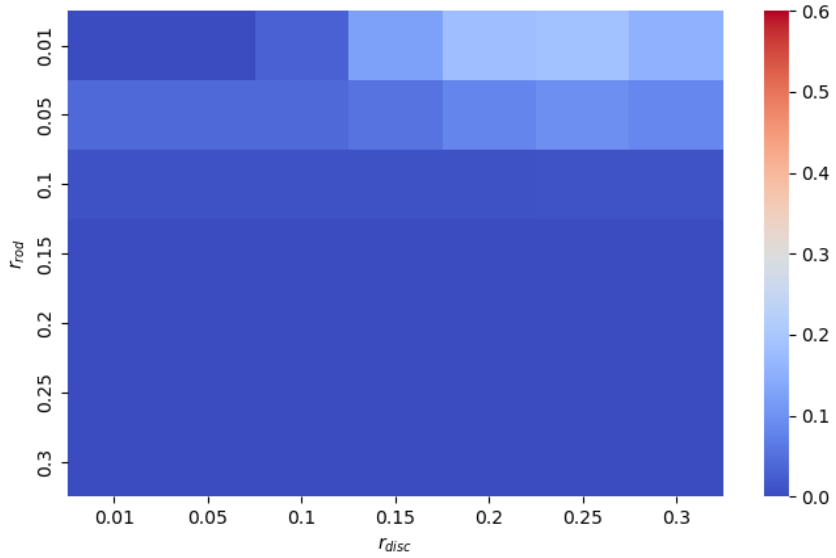


Figure 34: Heatmap of the gap-to-midgap ratio for the triangular lattice in TM polarization at dielectric contrast $\alpha = 4.0$.

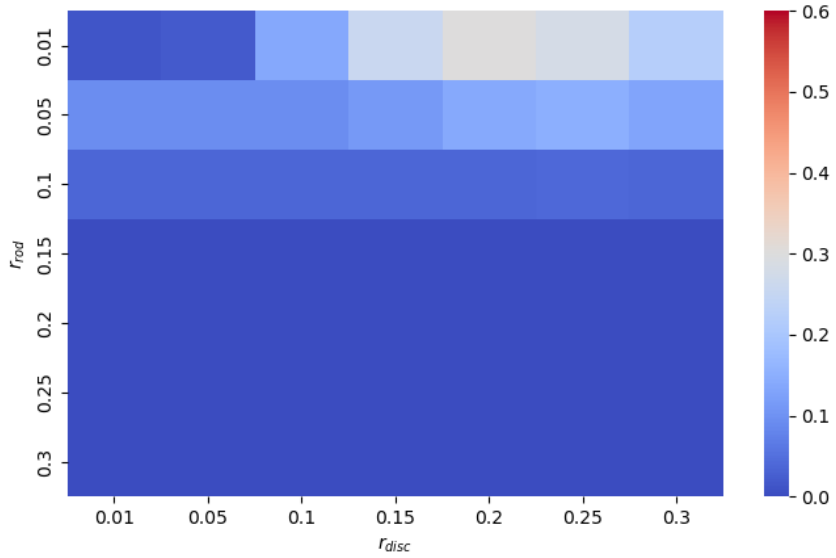


Figure 35: Heatmap of the gap-to-midgap ratio for the triangular lattice in TM polarization at dielectric contrast $\alpha = 7.0$.

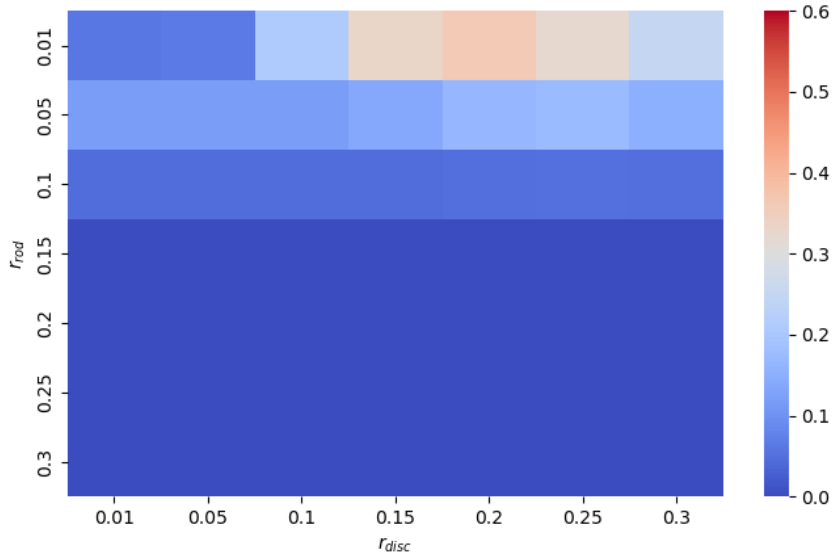


Figure 36: Heatmap of the gap-to-midgap ratio for the triangular lattice in TM polarization at dielectric contrast $\alpha = 10.0$.

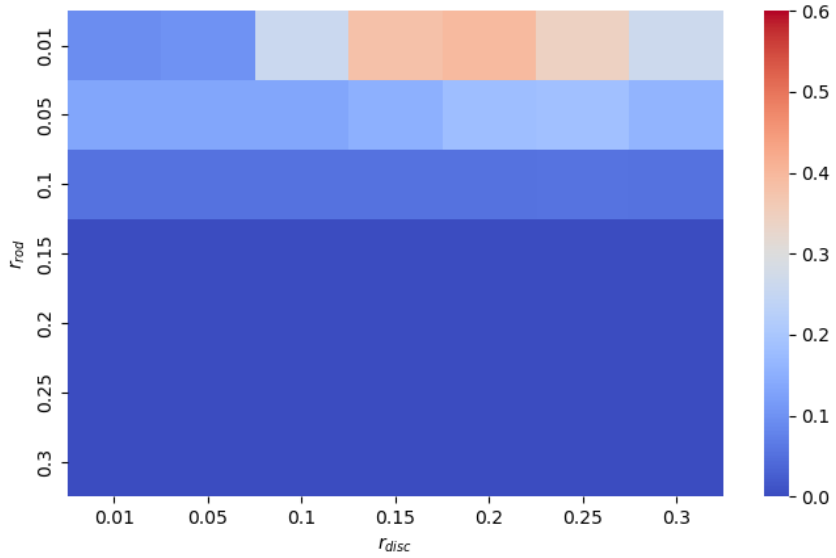


Figure 37: Heatmap of the gap-to-midgap ratio for the triangular lattice in TM polarization at dielectric contrast $\alpha = 13.0$.

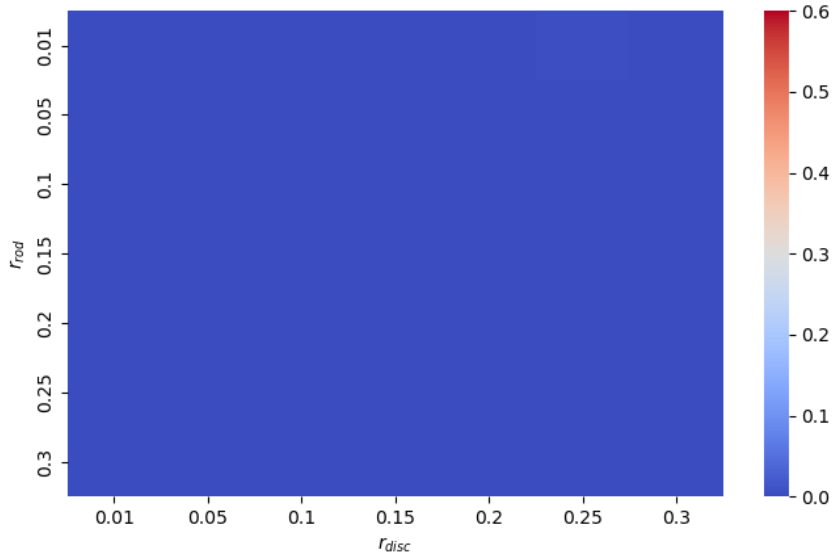


Figure 38: Heatmap of the gap-to-midgap ratio for the hexagonal lattice in TM polarization at dielectric contrast $\alpha = 4.0$.

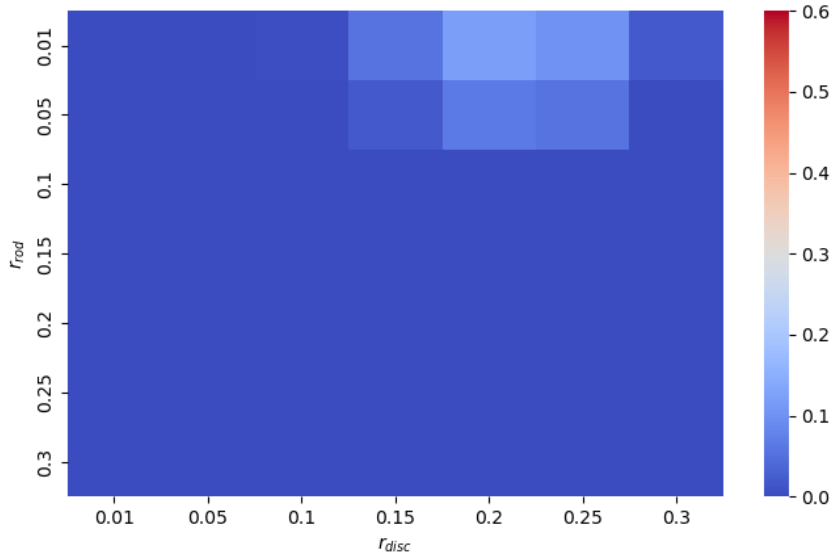


Figure 39: Heatmap of the gap-to-midgap ratio for the hexagonal lattice in TM polarization at dielectric contrast $\alpha = 7.0$.

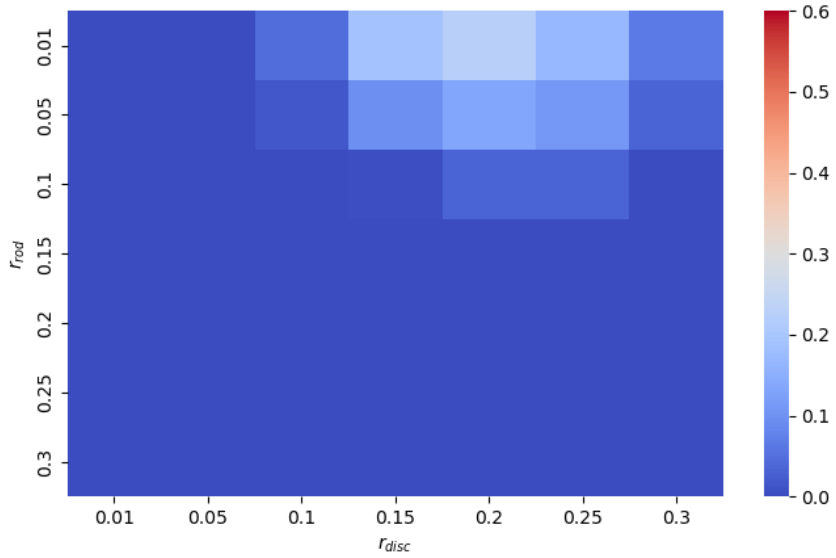


Figure 40: Heatmap of the gap-to-midgap ratio for the hexagonal lattice in TM polarization at dielectric contrast $\alpha = 10.0$.

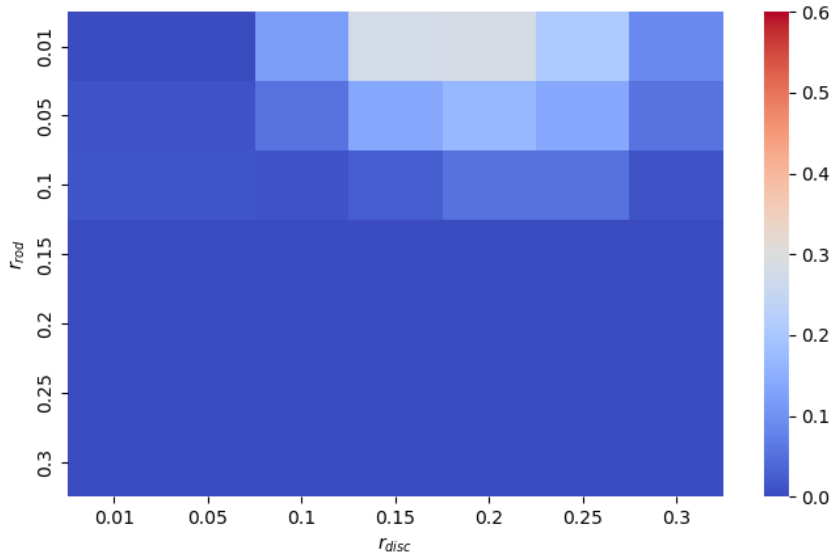


Figure 41: Heatmap of the gap-to-midgap ratio for the hexagonal lattice in TM polarization at dielectric contrast $\alpha = 13.0$.

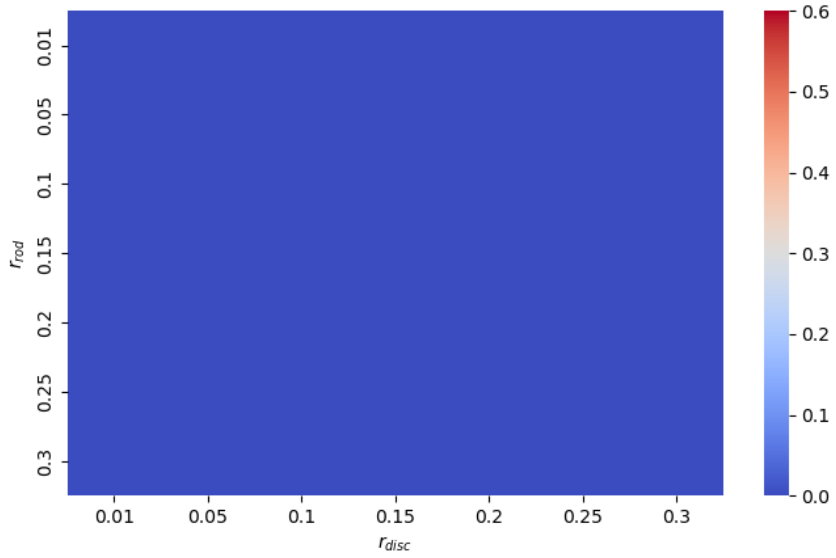


Figure 42: Heatmap of the gap-to-midgap ratio for the simple-cubic lattice in TE polarization at dielectric contrast $\alpha = 4.0$.

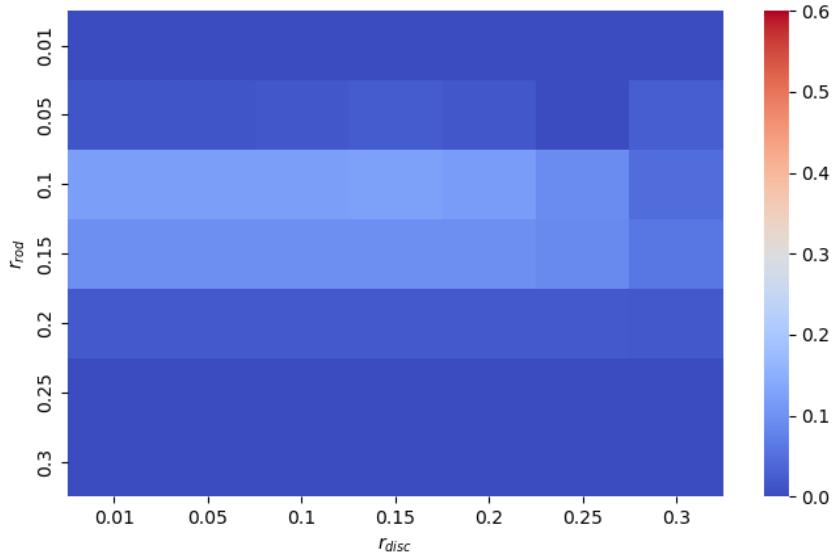


Figure 43: Heatmap of the gap-to-midgap ratio for the simple-cubic lattice in TE polarization at dielectric contrast $\alpha = 7.0$.

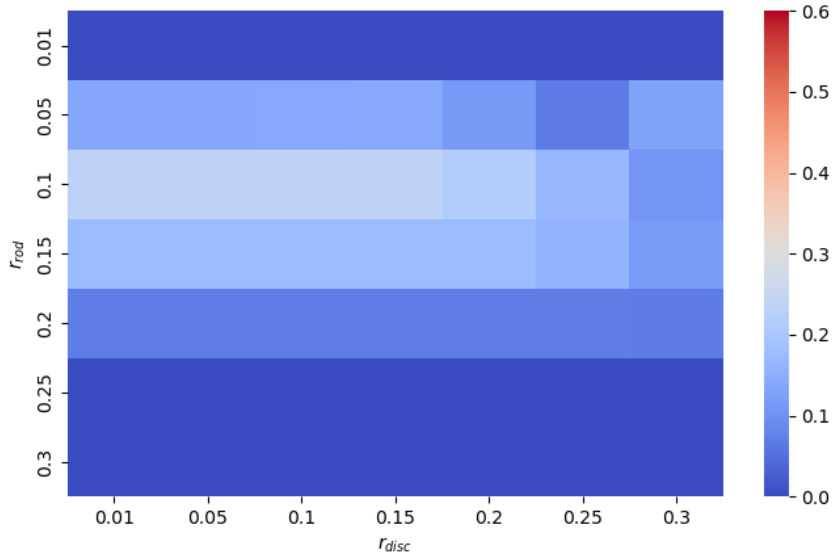


Figure 44: Heatmap of the gap-to-midgap ratio for the simple-cubic lattice in TE polarization at dielectric contrast $\alpha = 10.0$.

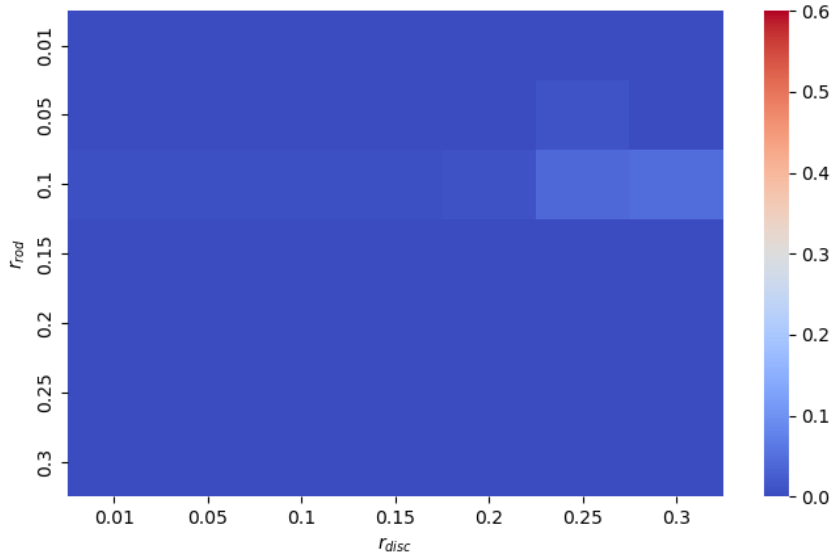


Figure 45: Heatmap of the gap-to-midgap ratio for the triangular lattice in TE polarization at dielectric contrast $\alpha = 4.0$.

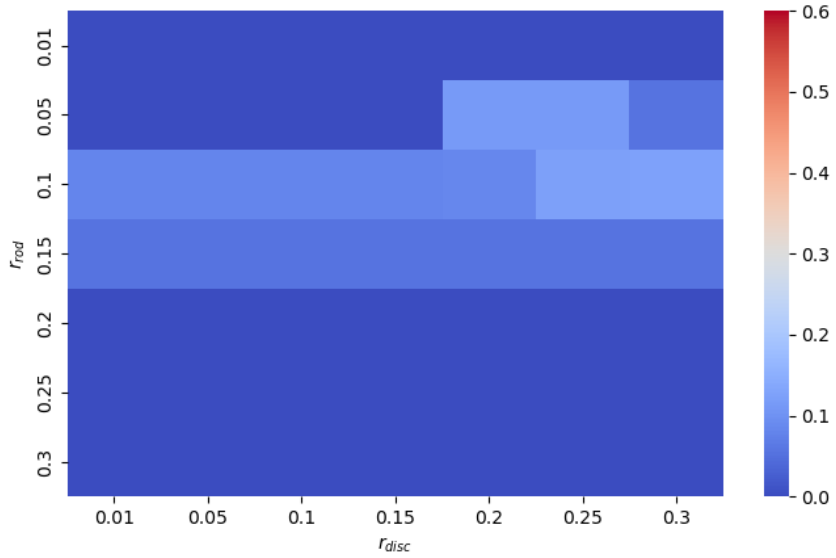


Figure 46: Heatmap of the gap-to-midgap ratio for the triangular lattice in TE polarization at dielectric contrast $\alpha = 7.0$.

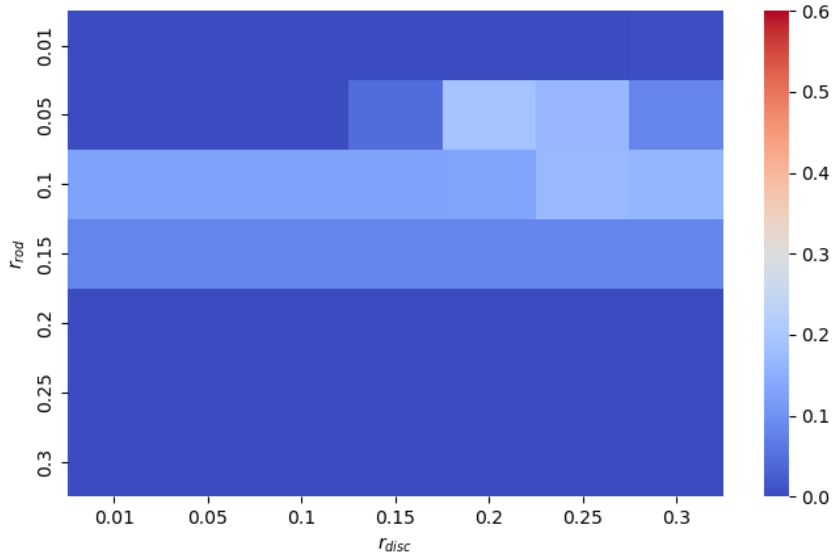


Figure 47: Heatmap of the gap-to-midgap ratio for the triangular lattice in TE polarization at dielectric contrast $\alpha = 10.0$.

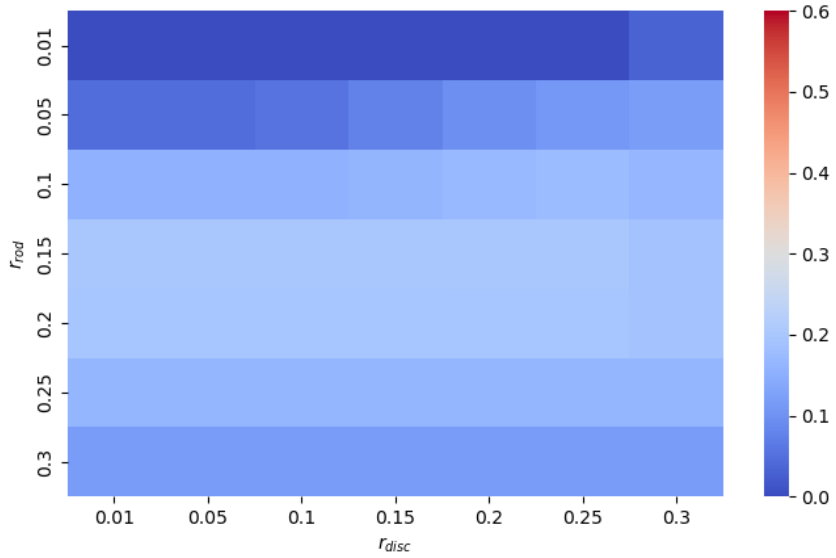


Figure 48: Heatmap of the gap-to-midgap ratio for the hexagonal lattice in TE polarization at dielectric contrast $\alpha = 4.0$.

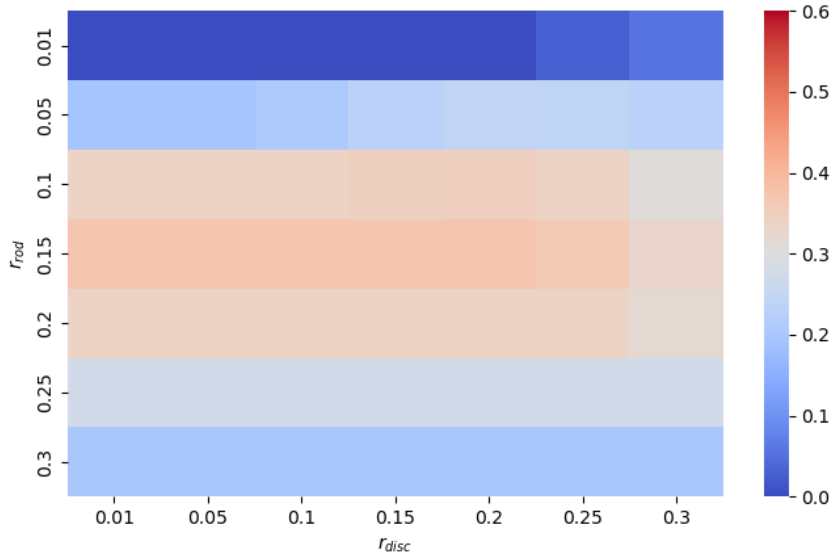


Figure 49: Heatmap of the gap-to-midgap ratio for the hexagonal lattice in TE polarization at dielectric contrast $\alpha = 7.0$.

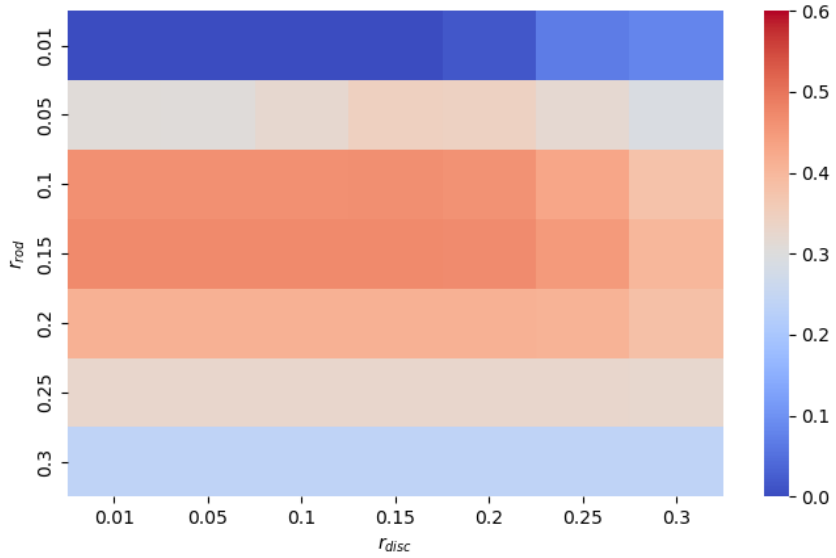


Figure 50: Heatmap of the gap-to-midgap ratio for the hexagonal lattice in TE polarization at dielectric contrast $\alpha = 10.0$.

B Appendix: Heatmaps for complete PBGs

The following section presents the heatmaps of the gap-to-midgap ratio for complete band gaps in network structures with simple-cubic, triangular, and hexagonal lattice geometries.

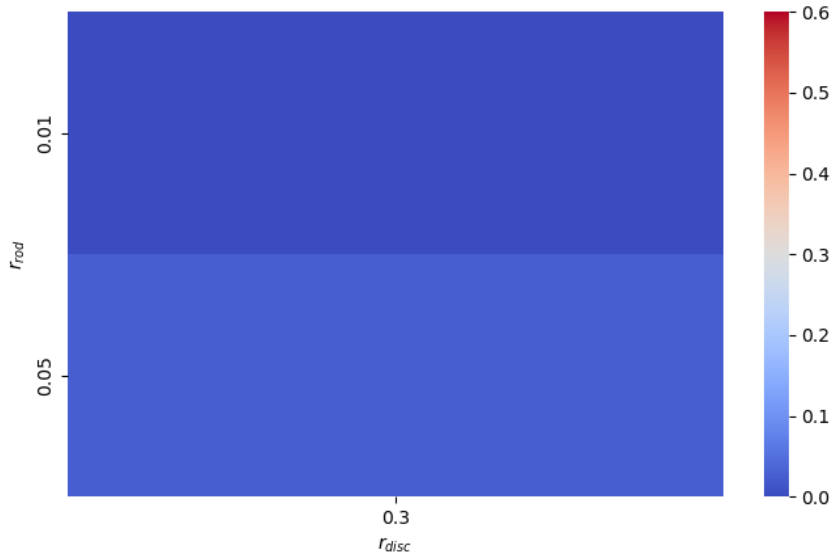


Figure 51: Heatmap of the gap-to-midgap ratio for complete band gaps in the simple-cubic lattice at a dielectric contrast of $\alpha = 7.0$.

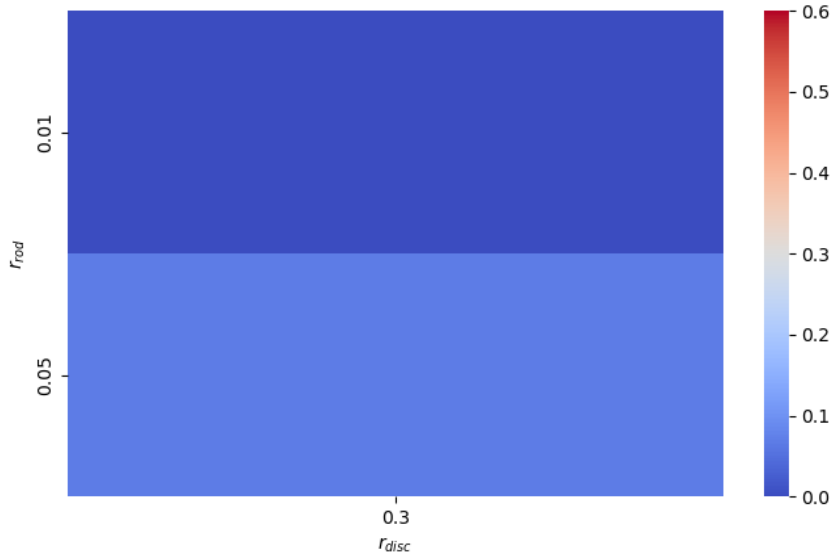


Figure 52: Heatmap of the gap-to-midgap ratio for complete band gaps in the simple-cubic lattice at a dielectric contrast of $\alpha = 10.0$

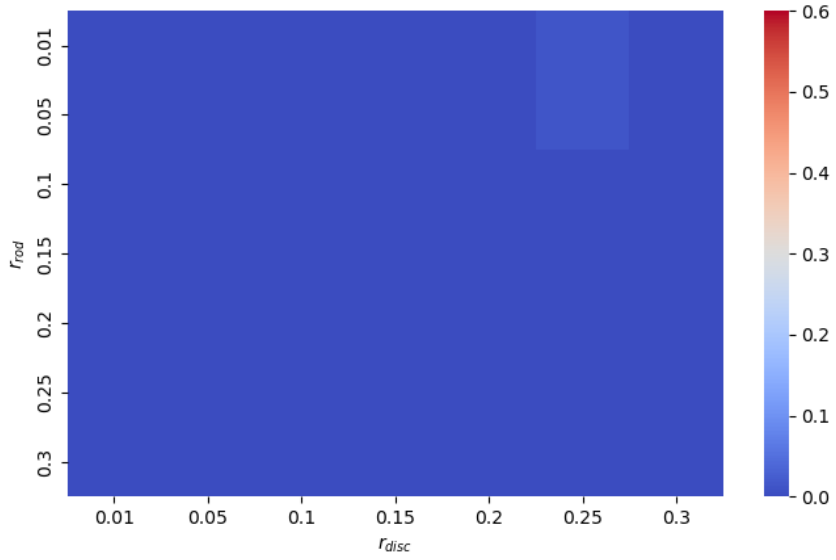


Figure 53: Heatmap of the gap-to-midgap ratio for complete band gaps in the hexagonal lattice at a dielectric contrast of $\alpha = 7.0$

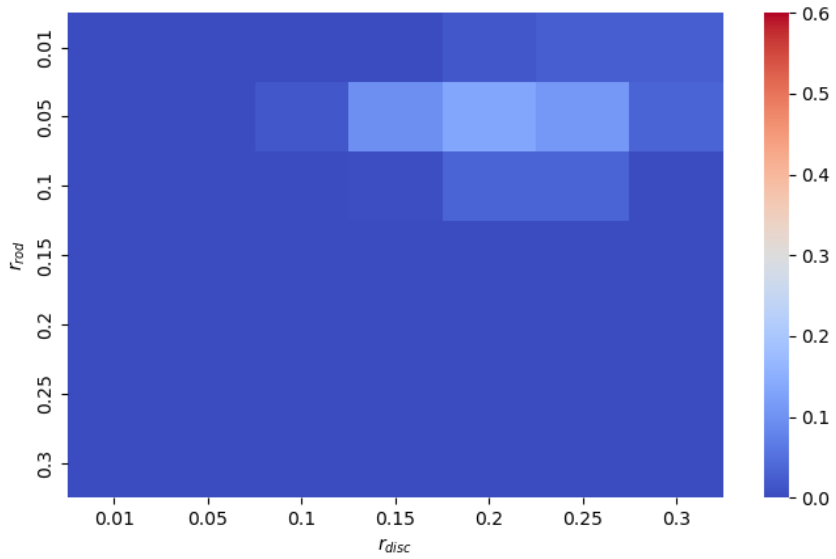


Figure 54: Heatmap of the gap-to-midgap ratio for complete band gaps in the hexagonal lattice at a dielectric contrast of $\alpha = 10.0$